A Measurement of the Cosmic Microwave Background Angular Power Spectrum with DASI

Thesis by

Nils W. Halverson

In Partial Fulfillment of the Requirements
for the Degree of
Doctor of Philosophy

California Institute of Technology
Pasadena, California

2002
(Defended September 17, 2001)

Acknowledgements

Graduate school has been a long journey for me, occasionally meandering, (almost) always enjoyable, and in the end immensely rewarding. My advisor John Carlstrom has been an unebbing source of support through the entire process. I first met John when he was a Millikan Fellow at Caltech, and I was a prospective graduate student. We have both changed quite a bit in the intervening years, but John has never ceased to encourage me, coax me, and humor my (very occasional) hard-headedness.

I have been privileged to work with a group of very talented people at the University of Chicago. John Carlstrom, John Kovac, Erik Leitch, and Clem Pryke have become familiar company. We have learned each other's strengths and weaknesses, and over the years we have achieved more than the sum of our parts, in an environment where ideas (even stupid ones!) are freely discussed in an atmosphere of trust and respect.

Aside from those of us in Chicago, there are many other people who have contributed to DASI's success. I am indebted to colleagues who have headed west, Mark Dragovan and Bill Holzapfel, for their dedication to the project. The CBI team at Caltech, John Cartwright, Brian Mason, Steve Padin, Tim Pearson, Tony Readhead, and Martin Shepherd have provided DASI with invaluable hardware, software, and technical expertise. Ethan Schartman and Sam LaRoque have spent long hours in the lab doing a myriad of jobs; Gene Davidson and John Yamasaki had the guts to spend the first winter with the telescope at the South Pole. Finally, the folks at the Center for Astrophysical Research in Antarctica have supported DASI throughout its deployment with expert care.

I survived my first two years of graduate school at Caltech with the help of many

people. Steve Sanders, Gilad Almogy, and I did battle with first-year problem sets together. Thomas Büttgenbach and Garrett Reisman sustained my interest in flying, and encouraged me to explore my hedonistic side. José Navarro gave me levity, and reminded me to taste the pleasures of life outside of work (including his Paella!).

Here in Chicago, I have been tirelessly fed by my friends Gary Wong and Michelle Molina, and entertained by their son Sam during the many evenings that I have been too busy to cook for myself. Diana Steele introduced me to early morning open-water swimming in Lake Michigan, through which I discovered both a bit of local wilderness, and the Hyde Park community at its finest.

My early mentors in the art of science include Tom Phillips at Caltech, my undergraduate advisor Doug Osheroff at Stanford, and Ben Tigner, who, as Doug's graduate student, took me on unassumingly and as a peer. My high school physics teacher Pat Hogan was a wonderful teacher; understated and patient, he thoughtfully answered my questions, encouraged my after-class experimental forays, and tolerated the damages I occasionally incurred on his equipment. My parents Jon and Anne were my very first science teachers. I have fond memories of my mother helping my brother Anders and me to pluck butterfly eggs from sprigs of dill in the garden for later observation, and my father showing us the stars through his 8" Newtonian telescope.

My family have always encouraged unfettered exploration, intellectually, vocationally, and in matters of the heart. They have stood behind me during this entire venture, and I couldn't have done it without them. It is to them that I dedicate this thesis.

Abstract

The Cosmic Microwave Background (CMB) has long been recognized as an astounding source of information about the early Universe. In this thesis we describe the design, implementation, and first-year results of the Degree Angular Scale Interferometer (DASI), a compact interferometer designed to measure the angular power spectrum of the CMB. We discuss details of the optics, receivers, and power spectrum analysis, including the use of constraint matrices to project out contaminants and test for correlations with diffuse foreground templates.

We present a measurement of the CMB angular power spectrum in the multipole range $l \approx 100$–900 in nine bands. The measured fluctuations have a temperature spectral index of $\beta = -0.1 \pm 0.2$ $(1\,\sigma)$, consistent with CMB. We find no evidence of foregrounds other than point sources in the data. We detect a first peak in the power spectrum at $l \sim 200$, a second peak in the power spectrum at $l \sim 550$, and a rise in the power spectrum at $l \sim 800$ which is indicative of a third, consistent with inflationary theories.

Using the DASI measurement along with COBE DMR data, and adopting conservative priors on the Hubble parameter $h > 0.45$ and an optical depth due to reionization $0.0 \leq \tau_c \leq 0.4$, we constrain the total density of the Universe $\Omega_{tot} = 1.04 \pm 0.06$, the spectral index of the primordial density fluctuations $n_s = 1.01^{+0.08}_{-0.06}$, and the physical baryon density $\Omega_b h^2 = 0.022^{+0.004}_{-0.003}$, among others (all 68% confidence limits). These constraints are consistent with inflation and estimates of $\Omega_b h^2$ from Big Bang Nucleosynthesis. With prior $h = 0.72 \pm 0.08$, we constrain the matter density $\Omega_m = 0.40 \pm 0.15$, and the vacuum energy density $\Omega_\Lambda = 0.60 \pm 0.15$, indicating from CMB data the presence of dark matter and dark energy in the Universe.

Contents

Acknowledgements iii

Abstract v

1 Introduction 1

1.1 Theoretical Overview 2

1.1.1 Inflation 2

1.1.2 Acoustic Oscillations 4

1.1.3 The Angular Power Spectrum 5

1.2 CMB Anisotropy Measurements 7

1.3 The DASI Experiment 10

1.4 Thesis Outline 11

2 DASI Instrument Overview 13

2.1 Introduction 13

2.2 Interferometry and the CMB 14

2.3 Instrument Configuration 15

2.4 Optics 18

2.5 Receivers 18

2.6 Downconverter and Correlator 20

2.7 Telescope Control and Data Handling 21

2.8 Mount 21

2.9 Tower Infrastructure & Environmental Design 22

2.10 Telescope Deployment 25
2.11 Ground Shields 26
2.12 The South Pole Site 28

3 Optics Design **31**
3.1 Introduction 31
3.2 Review of Previous Work 32
3.2.1 Fundamental Principles of Corrugated Horns 32
3.2.2 Broadband Throat Design 35
3.2.3 Return Loss in Wide Flare-Angle Horns 38
3.2.4 Lensed Corrugated Horns 39
3.3 Design of the DASI Lensed Corrugated Horn 41
3.3.1 Design of the Wide-Angle Horn 42
3.3.2 Design of the DASI Horn Lens and Shroud 49
3.4 Measurement Results 51
3.4.1 Return Loss Measurements 51
3.4.2 Beam Measurements 53
3.4.3 Coupling Measurements 57
3.5 Summary 59

4 Receivers **61**
4.1 Introduction 61
4.2 RF Design 61
4.3 Cryogenic Design 67
4.4 Performance 72

5 Observations **76**
5.1 Observing Strategy 76
5.2 Pointing 78
5.3 Calibration 79

5.3.1 Absolute Calibration 79
5.4 Data Reduction 81
5.5 Field Images 83
5.6 DASI Detected Point Sources 85

6 Analysis Formalism **88**
6.1 Introduction 88
6.2 The Fundamental Observable 89
6.3 The Interferometer Response 92
6.4 The Datavector and Data Covariance Matrix 95
6.4.1 The Theory Covariance Matrix 96
6.4.2 The Noise Covariance Matrix 104
6.4.3 Visibility Sensitivity 104
6.5 The Simple Quadratic Estimator 105
6.6 The Maximum Likelihood Estimator 109
6.7 Iterative Quadratic Estimator 110
6.7.1 Estimator Formalism 111
6.7.2 Single Iteration Example 114
6.8 Constraint Matrix Formalism 115
6.9 Non-Gaussian Uncertainties 118
6.10 Band-Power Window Functions 121
6.11 Cosmological Parameter Estimation 123
6.12 Likelihood Analysis Implementation 126
6.13 Summary 133

7 Results **134**
7.1 Introduction 134
7.2 Angular Power Spectrum Analysis 135
7.2.1 Analysis Formalism Summary 135

7.2.2 Noise Estimation 136
7.2.3 Ground Constraints 136
7.2.4 Point Source Constraints 137
7.3 Angular Power Spectrum Results 138
7.4 Consistency Tests 140
7.5 Diffuse Foregrounds 143

8 Conclusions **145**

Bibliography **153**

List of Tables

3.1 DASI lensed corrugated horn parameters. 51

3.2 DASI lensed corrugated horn beam parameters. 56

4.1 DASI receiver component specifications. 66

4.2 DASI receiver thermal load budget. 70

4.3 Noise temperature contributions of various receiver components. . . . 73

5.1 DASI CMB field row coordinates and dates observed. 77

5.2 DASI detected point sources. 87

7.1 Angular power spectrum band powers and uncertainties. 141

7.2 Correlation coefficient matrix for the DASI band powers. 141

8.1 Cosmological parameter constraints from DASI+DMR. 149

List of Figures

1.1 A typical theoretical power spectrum for an adiabatic inflationary model. 6
1.2 The angular power spectrum dependence on cosmological parameters. 8
1.3 Status of CMB angular power spectrum measurements in 1995. . . . 9
1.4 Status of CMB angular power spectrum measurements in 2000. . . . 10
2.1 The DASI telescope at the Admunsen-Scott South Pole Station. . . . 14
2.2 Two-element interferometer response pattern. 16
2.3 The DASI aperture plate configuration and (u, v) plane sensitivity. . . 17
2.4 The DASI prototype Ka-band receiver assembly. 19
2.5 Technical drawing of the DASI telescope structure. 22
2.6 Preliminary design of telescope-tower interface. 24
2.7 Telescope winter snow accumulation. 25
2.8 The DASI telescope being lifted to its tower. 27
2.9 The DASI ground shields. 28
2.10 Cumulative opacity distribution at the South Pole measured by DASI. 29
2.11 Short baseline visibility noise for the first season of observations. . . . 30
3.1 Geometry of corrugated waveguide. 35
3.2 Dispersion curves for corrugated waveguide hybrid modes. 36
3.3 Cross sections of three corrugated horn throat types. 37
3.4 Geometry of a meniscus lens. 40
3.5 An exploded view of the DASI lensed corrugated horn. 42
3.6 Geometry of the DASI corrugated horn throat. 43
3.7 Cylindrical slot depths for presenting an open or short. 45

3.8 Estimated return loss for the DASI corrugated horn throat design. . . 48
3.9 Theoretical aperture E-field distributions and beam patterns. 49
3.10 The measured return loss for the DASI lensed corrugated horn. 52
3.11 Beam patterns for the unlensed DASI corrugated horn. 54
3.12 Beam patterns for the lensed DASI corrugated horn. 55
3.13 DASI lensed horn beam pattern at $f = 30$ GHz, enlarged. 56
3.14 Time domain gate used for coupling measurements. 58
3.15 Measured coupling between adjacent horns. 59
4.1 DASI receiver schematic diagram. 63
4.2 DASI receiver physical layout. 63
4.3 Interior of the open DASI receiver. 64
4.4 DASI HEMT amplifier gain and noise temperature curves. 65
4.5 Receiver cool down performance. 68
4.6 Receiver waveguide thermal break. 70
4.7 Detail of the horn throat. 71
4.8 DASI receiver noise temperatures measured during calibration. 73
4.9 DASI receiver physical temperatures throughout the first season. . . . 75
5.1 Locations of the DASI CMB fields, plotted over the IRAS 100 μm map. 77
5.2 A DASI field image before and after ground and point source removal. 84
5.3 CLEANed images of five DASI CMB fields, showing image noise. . . . 85
5.4 Images of the 32 DASI fields, at $20'$ resolution. 86
6.1 Simple schematic of a two-element interferometer. 93
6.2 The aperture autocorrelation function. 100
6.3 The DASI aperture configuration and (u, v) plane coverage. 100
6.4 The diagonal DASI variance window functions. 101
6.5 Fractional power spectrum uncertainty vs. rms signal-to-noise ratio. . 108
6.6 Sample of the noise and constraint matrices. 117
6.7 Sample dust map and dust template for one of the DASI fields. . . . 118

6.8 Band-power window functions for the nine DASI bands. 124
6.9 Sample area of integration for a theory covariance matrix element. . . 127
6.10 Theory covariance matrix non-zero elements for a single field. 128
6.11 Test of the analysis software using simulated data. 132
7.1 Angular power spectrum from the first season of DASI observations. . 139
7.2 Angular power spectrum of individual field rows. 143
8.1 The DASI angular power spectrum with cosmological models. 147
8.2 Marginal likelihood distributions, varying the prior on h. 148
8.3 Marginal likelihood distributions, varying the prior on τ_c. 150
8.4 April 2001 power spectra from DASI, BOOMERanG, and MAXIMA. 151

Chapter 1

Introduction

The Cosmic Microwave Background (CMB) radiation, first discovered in 1964 by Penzias & Wilson (1965), is an ancient glowing jewel; imprinted with an abundance of information about the Universe in its infancy, it continues to enrich us some 35 years after its discovery. The CMB is relic radiation from the epoch $\sim 400,000$ years after the Big Bang when light decoupled from matter as the Universe cooled and expanded. Subtle temperature fluctuations in the Cosmic Microwave Background (CMB) radiation, first observed by the COBE DMR experiment (Smoot et al. 1992), provide information about density perturbations in the nearly homogeneous early Universe, well before the non-linear gravitational collapse of matter led to the structure we see today. Temperature anisotropy on different angular scales gives us information about physical processes operating on different physical length scales in the early Universe. Angular scales $\gtrsim 1^\circ$ were causally unconnected at the epoch of decoupling; anisotropy on these scales represents the primordial density inhomogeneity of matter (see, e.g., White et al. 1994). On scales $\lesssim 1^\circ$ gravitational interactions enhance the density perturbations, leaving characteristic features in the CMB angular power spectrum (see, e.g., Hu et al. 1997). Measurements of this angular power spectrum can be used to test cosmological theories, and within the context of standard cosmological models, they can be used to determine fundamental cosmological parameters (Knox 1995; Jungman et al. 1996). The Degree Angular Scale Interferometer (DASI), the subject of this thesis, is designed to measure the angular power spectrum of the CMB

on angular scales of $\sim 15'$–$2°$, enabling us to test the validity of currently favored cosmological theories, and to determine the contributions of baryonic matter, dark matter, and vacuum energy to the total density of the Universe.

1.1 Theoretical Overview

In the most widely accepted cosmological theories, the evolution of the Universe can be split into three major epochs: an inflationary epoch during which the Universe expanded exponentially and generated an initial spectrum of density perturbations, the plasma epoch during which the perturbations evolved through gravitationally driven acoustic oscillations, and the structure formation epoch which started when the Universe became neutral, allowing gravitational collapse into the structures we see in the present-day Universe. The CMB photons come to us from the end of the plasma epoch at a redshift $z_* \sim 1000$, corresponding to an age of $\sim 400,000$ years. Prior to this time, photons were tightly coupled to electrons via Thomson scattering; the electrons were in turn coupled to the baryons. At the end of the plasma epoch (the so-called *epoch of decoupling*) the fractional ionization of baryons dropped precipitously, driven primarily by the decrease in electron number density due to the Universal expansion (see discussion in Kolb & Turner 1990). The mean free path of photons became nearly infinite (larger than the causal horizon), and photons propagated unimpeded. To the present-day observer, these photons are detectable as the CMB, emanating from the *surface of last scattering* some 15 billion light-years distant, and carrying with them precious information about the early Universe.

1.1.1 Inflation

The theory of inflation (Guth 1981; Linde 1982; Albrecht & Steinhardt 1982) was originally proposed as an explanation for the apparent isotropy in the CMB on causally unconnected angular scales (the *horizon problem*), and as an explanation for evidence

that the density of the Universe is nearly equal to the critical density, where it has a spatially flat geometry (the *flatness problem*). The density of the early Universe would need to be fine-tuned to extraordinary precision to avoid diverging to a grossly closed or open geometry at the present epoch (Dicke 1970), but prior to inflation, a mechanism for fine-tuning the total density to the critical density was not known. The inflation theory was further developed as a natural mechanism which predicts nearly scale invariant adiabatic density perturbations as the source of inhomogeneity in the Universe (Guth & Pi 1982; Hawking 1982; Starobinsky 1982; Bardeen et al. 1983). Scale invariant perturbations were first proposed about a decade earlier by Harrison (1970) and Zeldovich (1972) from other theoretical arguments, although the mechanism for generating these perturbations was not then postulated.

Inflation is a phase transition which occurred at Grand Unified Theory (GUT) energy scales, at a time $t \sim 10^{-35}$ s, when a scalar field evolved from a quasi-stable state of non-zero potential, or *false vacuum* state, to the true vacuum state at zero potential (see, e.g., review by Narlikar & Padmanabhan 1991). During this transition, the Universe underwent exponential expansion of $\mathcal{O}(10^{30})$ e-foldings. Quantum mechanical fluctuations in the field crossed the causal horizon (or *Hubble radius*) during exponential expansion, and were stretched to cosmological length scales. During the exponential expansion phase, the fluctuations were produced under approximately identical conditions on all length scales, generating a nearly scale invariant spectrum of perturbations. At the end of the inflation epoch, these fluctuations re-entered the horizon as the Hubble radius grew. Inflation solves the horizon problem since the observable Universe was in causal contact and in thermal equilibrium in the pre-inflationary epoch. It also solves the flatness problem since the exponential expansion locally flattens spatial curvature to high precision.

1.1.2 Acoustic Oscillations

The primordial adiabatic density perturbations gave rise to gravity-driven acoustic oscillations in the plasma which lead to a series of harmonic peaks in the CMB angular power spectrum (Peebles & Yu 1970; Bond & Efstathiou 1984; Vittorio & Silk 1984). The acoustic oscillations responsible for degree-scale anisotropy evolved linearly in a cool (10^4–10^3 K) Universe in a realm well described by classical physics, and may be understood in terms of a simple harmonic oscillator (see Scott & White 1995; Hu et al. 1997, for a review of CMB physics). The photons provided the restoring force and the baryons provided the inertial mass in the photon-baryon fluid. In a Universe where the matter content is dominated by a non-relativistic ("cold") dark matter (CDM) component, as is presently favored, the primordial density fluctuations in CDM provided the gravitational potential wells in which the fluid oscillated. Initially, the fluid had zero velocity (apart from the overall Universal expansion). As the Universe evolved, progressively larger regions came into causal contact. Fourier modes k with spatial wavelengths k^{-1} comparable to the sound horizon $s = \int c_s d\eta$ (where η is conformal time) began to compress, with baryons falling into the CDM potential wells. The fluid compressed until photon pressure provided sufficient resistance to re-expand the fluid. These driven oscillations continued until the epoch of decoupling, z_*, when the photons ceased to scatter, preserving information on the phase and amplitudes of the oscillating modes and carrying this information to the present-day observer.

Because the oscillations started with the same initial conditions and had periods which were proportional to the wavelength of the mode, the phases of the modes at last scattering (z_*) were proportional to their wavenumber k, resulting a series of harmonic peaks in the power spectrum, where the modes were at extrema in the oscillation cycle. The fundamental (largest spatial scale) peak results from modes which had reached their first state of maximum compression (1/2 cycle) at z_*. The second peak is due to modes which had time to progress in the oscillation cycle

to the state of maximum rarefaction (1 cycle); higher order peaks represent modes at an integral number of half-cycles. Thus odd-numbered peaks represent states of maximum compression, and even peaks represent states of maximum rarefaction. The harmonic peaks are damped at small spatial scales (the so-called *damping tail*). This is due to two effects: the finite mean free path of the photons in the plasma prior to decoupling allows photons to diffuse between hot and cold spots, and, because the epoch of decoupling is not instantaneous, spatial wavelengths shorter than the finite thickness of the surface of last scattering destructively interfere.

1.1.3 The Angular Power Spectrum

From the present observer's point of view, the density fluctuations at the epoch of decoupling appear in the angular power spectrum of CMB temperature fluctuations. The fractional temperature fluctuations in a direction $\hat{s}$ on the sky can be decomposed into spherical harmonics:

$$\frac{\Delta T}{T}(\hat{s}) = \sum_{l,m} a_{lm} Y_{lm}(\hat{s}). \tag{1.1}$$

The theoretical angular power spectrum C_l is a statistical average over an ensemble of universes of the temperature spherical harmonic coefficients,

$$C_l = \left\langle |a_{lm}|^2 \right\rangle . \tag{1.2}$$

The multipole moment l is inversely proportional to angular scale, $l \sim \theta^{-1}$. Experiments which measure the angular power spectrum measure the statistical properties of temperature fluctuations in our (one realization of the) CMB sky. Thus, we are inherently limited in our measurement of the power spectrum C_l by the number of samples ($2l + 1$ if the entire sky is observed) for a given multipole moment l. A more detailed discussion of the observable is given in §6.2. A typical angular power spectrum is shown in Fig. 1.1.

The angular power spectrum is influenced by a number of fundamental parameters such as the density of baryons Ω_b, cold dark matter density Ω_{cdm}, vacuum

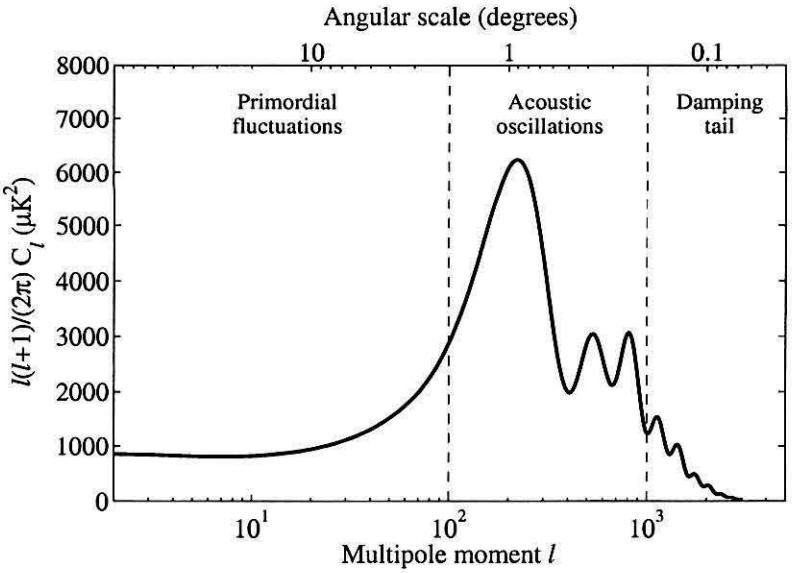

Figure 1.1 A typical theoretical power spectrum for an adiabatic inflationary model. The physical processes which determine the predicted features depend on the angular scale. Angular scales $\gtrsim 1°$ are causally unconnected at the epoch of decoupling; the power spectrum at these scales is determined by the primordial fluctuations, which inflation predicts are nearly scale invariant adiabatic fluctuations. On angular scales $\lesssim 1°$ gravitationally driven acoustic oscillations lead to a series of harmonic peaks in the angular power spectrum. Power on angular scales $\lesssim 0.1°$ is damped due to photon diffusion in the plasma and destructive interference within the finite thickness of the last scattering surface.

energy density Ω_Λ, the Hubble parameter h, the spatial spectral index of the primordial fluctuations n_s, and the optical depth of reionization τ_c, among others. The total matter density is given by $\Omega_m \equiv \Omega_b + \Omega_{cdm}$ and the total density is given by $\Omega_{tot} \equiv \Omega_m + \Omega_\Lambda$. Here, the densities of the various components are expressed as ratios with respect to the critical density, $\Omega_i \equiv \rho_i/\rho_{\rm crit}$ where $\rho_{\rm crit} = 3H_0^2/(8\pi G)$ is the density at which the Universe is spatially flat, H_0 is the Hubble constant and G is the gravitational constant. The Hubble parameter h is given by the relation $H_0 = 100h$ km s^{-1} Mpc^{-1}. Within the framework of the most widely accepted CDM models, the CMB angular power spectrum can be calculated with precision given a set of cosmological parameters, and code is freely available which can rapidly generate

power spectra (Zaldarriaga & Seljak 2000). The models which we use in Chapter 8 to place constraints on cosmological parameters exclude such possibilities as tensor perturbations due to gravity waves and a "hot" dark matter component (i.e., massive neutrinos). Both are thought to be unlikely to contribute to the CMB angular power spectrum at a significant level compared with the DASI measurement uncertainties (Lyth 1997; Dodelson et al. 1996).

A detailed discussion of the effect of various parameters on the power spectrum is beyond the scope of this work, but several key dependencies should be noted. First, the angular scale of the first peak is determined by the spatial geometry of the Universe (which is a function of Ω_{tot}), since the apparent angular scale of the first peak is influenced primarily by the geodesics along which the photons travel to the present-day observer. Second, the ratio of the even to odd peak amplitudes depends on the baryon number density, which is a function of $\Omega_b h^2$. This is due to the fact that the the presence of baryons dynamically influences the depth of the potential wells, lowering the zero-point of the acoustic oscillations, which in turn suppresses the amplitudes of the rarefaction phase. Finally, a third harmonic peak of comparable or greater magnitude than the second is the signature of baryonic matter re-compressing in dark matter potential wells, and is a tell-tale sign of the presence of non-baryonic cold dark matter (assuming a reasonable value for the spectral index n_s). Angular power spectra showing the effect of varying Ω_{tot}, $\Omega_b h^2$, and $\Omega_{cdm} h^2$ are shown in Fig. 1.2.

1.2 CMB Anisotropy Measurements

Tremendous improvements in experimental sensitivity have been made since CMB anisotropy on angular scales of $\sim 10^\circ$ was first detected by the COBE DMR experiment in 1992 (Smoot et al. 1992). By 1995, the year the DASI experiment was first proposed, several detections of anisotropy had been made at degree angular scales, although experimental sensitivity and l-space coverage were not sufficient to resolve

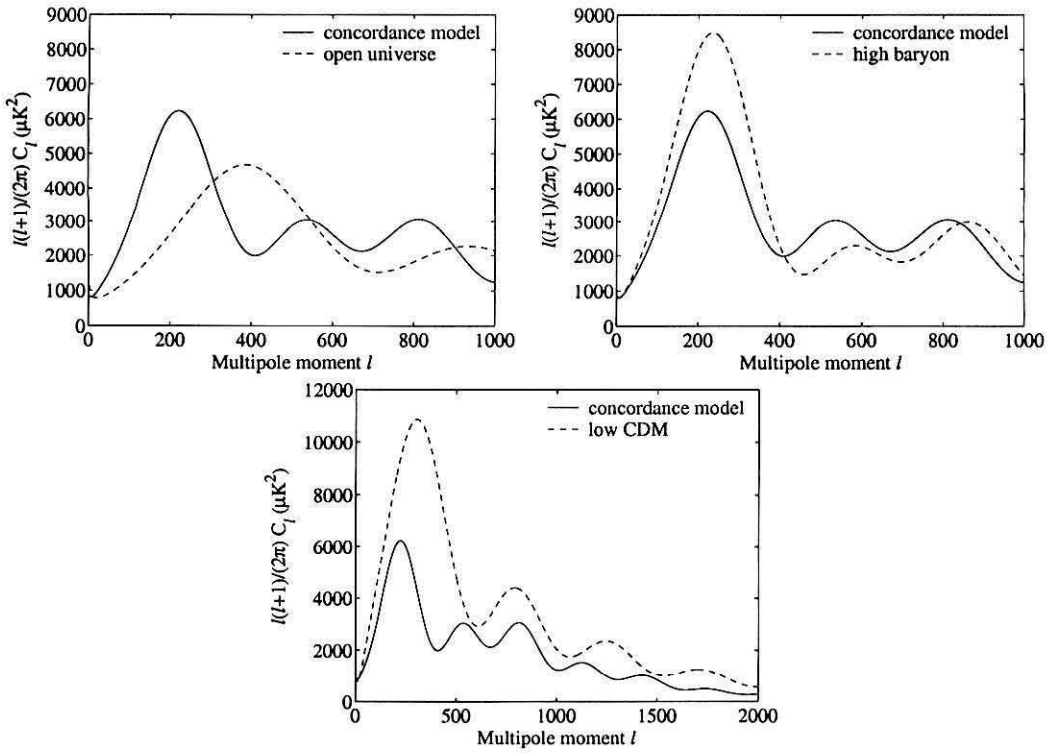

Figure 1.2 The angular power spectrum dependence on cosmological parameters. The base model used for comparison is a favored "concordance" model which has parameters $(\Omega_b, \Omega_{cdm}, \Omega_\Lambda, \tau_c, n_s, h) = (0.05, 0.65, 0.30, 0, 1, 0.65)$. The top left panel shows that reducing the total density of the Universe ($\Omega_{tot} = \Omega_b + \Omega_{cdm} + \Omega_\Lambda$) moves the first peak to smaller angular scales. The top right panel shows the effect of raising the baryon content, which suppresses the amplitude of the second peak with respect to the first and third peaks. The lower middle panel shows the effect of reducing the cold dark matter (CDM) content of the Universe, which suppresses the third peak with respect to the first and second peaks.

the predicted first peak (see Fig. 1.3). In 1999 and 2000, experiments determined the location of the degree-scale first peak (Miller et al. 1999; Mauskopf et al. 2000; de Bernardis et al. 2000; Hanany et al. 2000), providing strong evidence that the Universe is spatially flat ($\Omega_{tot} \sim 1$), a key prediction of inflation (see Fig. 1.4). The Cosmic Background Imager (CBI) also made the first detection by a single experiment of a decrease in power in the damping tail region of the power spectrum (Padin et al. 2001b). While hints of structure at sub-degree angular scales were present in these

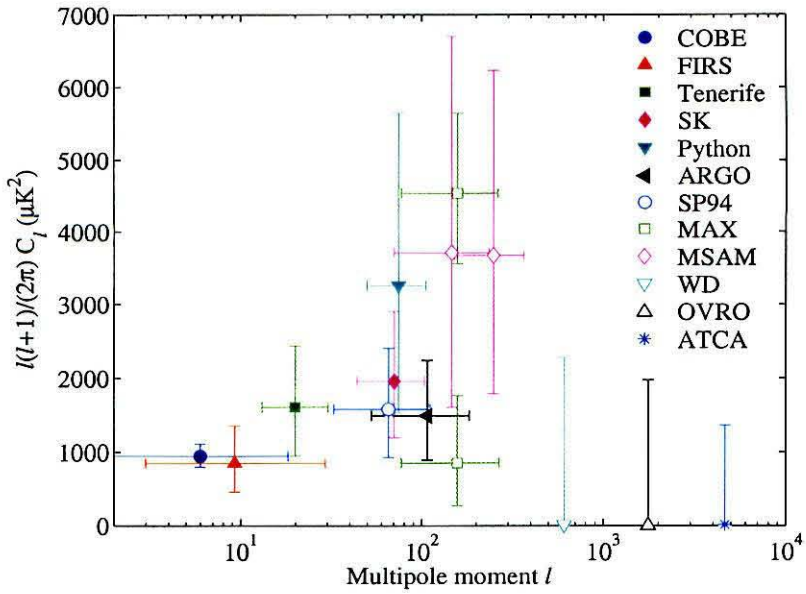

Figure 1.3 Status of CMB angular power spectrum measurements in 1995, from a compilation in Scott et al. (1995). (See this paper for references to individual experiments.) The three experiments probing multipole moments $l > 500$ are upper limits. Although multiple experiments had detections at degree angular scales, a peak in the power spectrum was not clearly discernible.

results, harmonic peaks in the power spectrum were not yet apparent. This was the experimental status in the period leading to the release of the DASI first-year results (the measurements presented in this thesis) in April 2001.

A detection of a series of harmonic peaks in the CMB angular power spectrum would provide additional strong evidence for the inflationary view of the early Universe, confirming another key prediction of inflation — gravity driven acoustic oscillations seeded by primordial adiabatic density perturbations. In addition, a precision measurement of the CMB angular power spectrum in multiple bands extending from the first peak through the multipole moment of the predicted third peak at $l \sim 800$ would enable us to place tight constraints on cosmological parameters such as $\Omega_b h^2$ and $\Omega_{cdm} h^2$, in addition to Ω_{tot}, within the context of standard cosmological models.

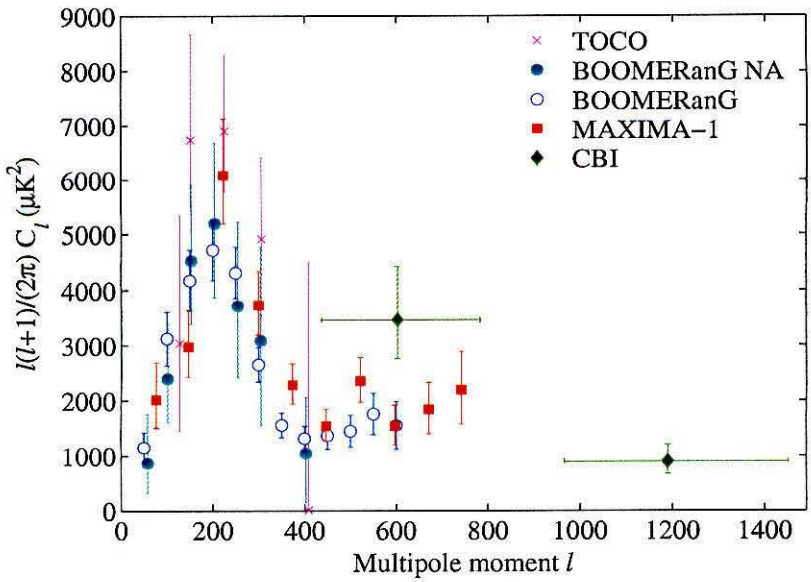

Figure 1.4 Status of CMB angular power spectrum measurements in 2000. Multiple experiments (Miller et al. 1999; Mauskopf et al. 2000; de Bernardis et al. 2000; Hanany et al. 2000) showed the presence of a peak in the CMB angular power spectrum at $l \sim 200$, revealing the Universe is spatially flat ($\Omega_{tot} \simeq 1$), confirming one of the key predictions of the inflationary theory. The Cosmic Background Imager (CBI) made the first detection by a single experiment of decreasing power in the damping tail (Padin et al. 2001b), further supporting the standard cosmological model.

1.3 The DASI Experiment

DASI is one of a new generation of interferometers, including its sister instrument the Cosmic Background Imager (CBI) (Pearson et al. 2000) and the Very Small Array (VSA) (Jones 1997) designed specifically to measure the angular power spectrum of the CMB. An interferometer is a natural choice for making a subtle difference measurement of temperature fluctuations on the microwave sky. The response pattern of each pair of antennas is a sinusoidally varying interference pattern on the sky, and the sky brightness difference measurement is instantaneous. An interferometer makes a direct measurement of the Fourier transform of the sky temperature fluctuations, allowing a relatively straightforward analysis of the CMB angular power spectrum.

DASI is a compact cm-wavelength interferometer designed to measure the CMB

angular power spectrum in multiple bands in the range $100 < l < 900$, corresponding to the span of the first three harmonic peaks in a flat inflationary Universe. The instrument was deployed at the South Pole in November 2000, and made observations throughout the following austral winter. In this thesis we present a measurement of the angular power spectrum in nine bands across this l range with fractional uncertainties of 10–20% and dominated by sample variance. With this measurement we are able to test for the presence of multiple harmonic peaks in the CMB angular spectrum, and place stringent constraints on fundamental cosmological parameters.

1.4 Thesis Outline

This thesis describes the design and implementation of the DASI instrument as well as first-year results, including a precise measurement of the CMB angular power spectrum in the range $100 < l < 900$. A project of this magnitude is of course a group effort, and many talented people have contributed to its success — this is acknowledged by the use of the first person plural throughout this work. The structure of this thesis emphasizes the contributions of the author, which include the design and development of the optics and receivers, deployment and testing of the telescope at the South Pole, and data analysis, including the development of the power spectrum analysis software. An overview of the instrument configuration and deployment is given in Chapter 2. In Chapter 3, we discuss the design and measurements of the lensed corrugated horns which comprise the DASI optics; this material will soon be submitted as a dedicated paper (Halverson & Carlstrom 2001). Chapter 4 gives the details of the receiver design and measured performance at the South Pole. The first year of observations with DASI is described in Chapter 5. The formalism for the power spectrum analysis is introduced in Chapter 6, as well as a more detailed discussion of the CMB observable and interferometry. The CMB angular power spectrum results are given in Chapter 7. Finally, we draw some conclusions in Chapter 8, including a discussion of cosmological parameter constraints. The material in Chapters 5 and 7

as well as the discussion of parameter constraints in Chapter 8 overlaps substantially with the DASI first-year results papers (Leitch et al. 2001; Halverson et al. 2001; Pryke et al. 2001) which were submitted to *The Astrophysical Journal* in April 2001.

Chapter 2

DASI Instrument Overview

2.1 Introduction

DASI is a compact centimeter-wavelength interferometer designed to image the CMB primary anisotropy and measure its angular power spectrum at degree and sub-degree angular scales (see Fig. 2.1). As an interferometer, DASI measures the Fourier transform of the sky temperature distribution directly. The instrument has 13 antenna elements, consisting of 20-cm aperture-diameter lensed corrugated horns; the elements are configured to measure the CMB angular power spectrum in the multipole range $100 < l < 900$ in multiple bands. All elements are mounted on a single alt-az mount, which fixes the projected baselines and obviates an intermediate frequency (IF) tracking delay. The receivers utilize cooled low-noise HEMT amplifiers operating in Ka band, 26–36 GHz. The signal is downconverted to a 2–12 GHz IF output, and the 10 GHz IF bandwidth is correlated in 1 GHz bands to provide spectral index information. The telescope was successfully deployed at the South Pole during the 1999–2000 austral summer; the data presented in this thesis were taken throughout the following austral winter. This chapter partially draws upon previous papers on the DASI instrument and experimental setup (Halverson et al. 1998; Leitch et al. 2001).

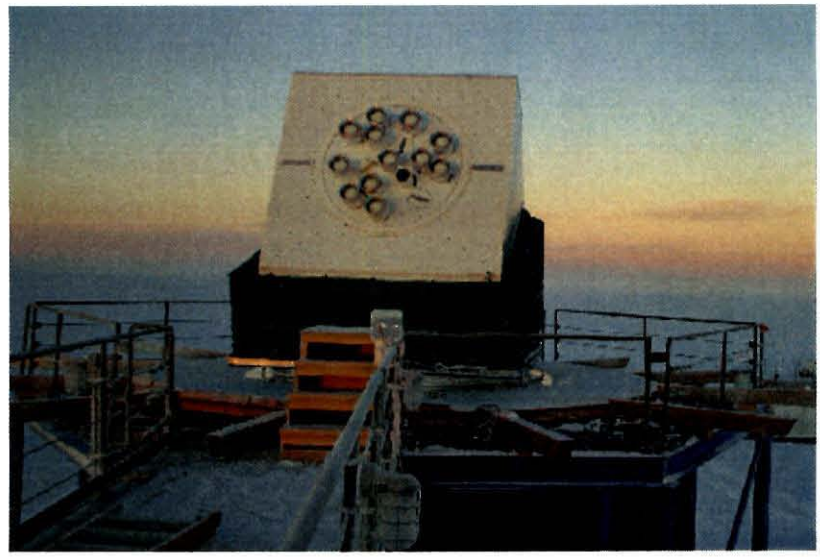

Figure 2.1 The DASI telescope, perched atop a 35′ tower attached to the Martin A. Pomerantz Observatory (MAPO) building at the Admunsen-Scott South Pole Station, March 2000. The telescope was successfully deployed during the austral summer 1999–2000; the data presented in this thesis were taken throughout the following austral winter.

2.2 Interferometry and the CMB

An interferometer is inherently a differencing instrument which is insensitive to the constant component of the both the CMB and the Earth's atmosphere, and thus is an excellent tool for measuring anisotropy. Unlike single-dish experiments which move a beam mechanically in sweeps of constant elevation to map temperature differences on the sky, an interferometer makes instantaneous difference measurements. The response pattern on the sky for a given pair of antennas is a sinusoidal fringe pattern attenuated by the primary beam of the individual antennas, Fig. 2.2. For a pair of antennas with a physical separation (*baseline*) vector $\mathbf{b}$, the center of the measured Fourier components, labeled $\mathbf{u}$ or (u, v), is given by $u = b_x/\lambda$ and $v = b_y/\lambda$, where b_x and b_y are the projections of the baseline normal to the line of sight, and λ is the observing wavelength. The approximate conversion to multipole moment is given by $l \approx 2\pi\,|\mathbf{u}|$ (White et al. 1999a), with a width Δl that is related to the diameter of

the apertures in units of observing wavelength.

An interferometer directly measures the Fourier transform of the sky temperature at many points in the Fourier plane, enabling the synthesis of two-dimensional images from a single pointing on the sky and relatively straight-forward power spectrum analysis. We can also design an observing strategy with widely separated pointings on the sky which maximizes the number of independent samples of the sky, and reduces the correlations between fields that make analysis more difficult. We are able to tailor our observing strategy to achieve a given science goal, and eliminate potential contamination from the ground through repeated observations of several fields at constant elevation (see Chapter 5). A more rigorous description of the output of an interferometer and the power spectrum analysis formalism is given in Chapter 6.

2.3 Instrument Configuration

The DASI antenna array consists of thirteen 20-cm diameter lensed corrugated horns, compactly arranged on a 1.6-m diameter aperture plate, with antenna spacings designed to densely sample the CMB angular power spectrum in the angular wavenumber range $100 \lesssim l \lesssim 900$ (see Fig. 2.3). The aperture plate may be rotated about the pointing axis to increase (u, v) coverage and provide redundancy checks using the three-fold rotational symmetry of the antenna pattern. The low-noise Ka-band receivers have 10 GHz of IF bandwidth, correlated in ten 1 GHz bands with an analog correlator. DASI is an extremely sensitive instrument, able to detect rms sky temperature fluctuations of 10 μK with a resolution of $20'$ in 24 hours with 10 GHz bandwidth. All backend electronics, including the telescope control computer, receiver and local oscillator (LO) control, IF downconversion, and correlators reside in three 9U height custom VME crates which are rigidly attached to the rear of the aperture plate structure near the back end of the receivers, and move with the receivers. This eliminates the need for long cables which would compromise phase stability.

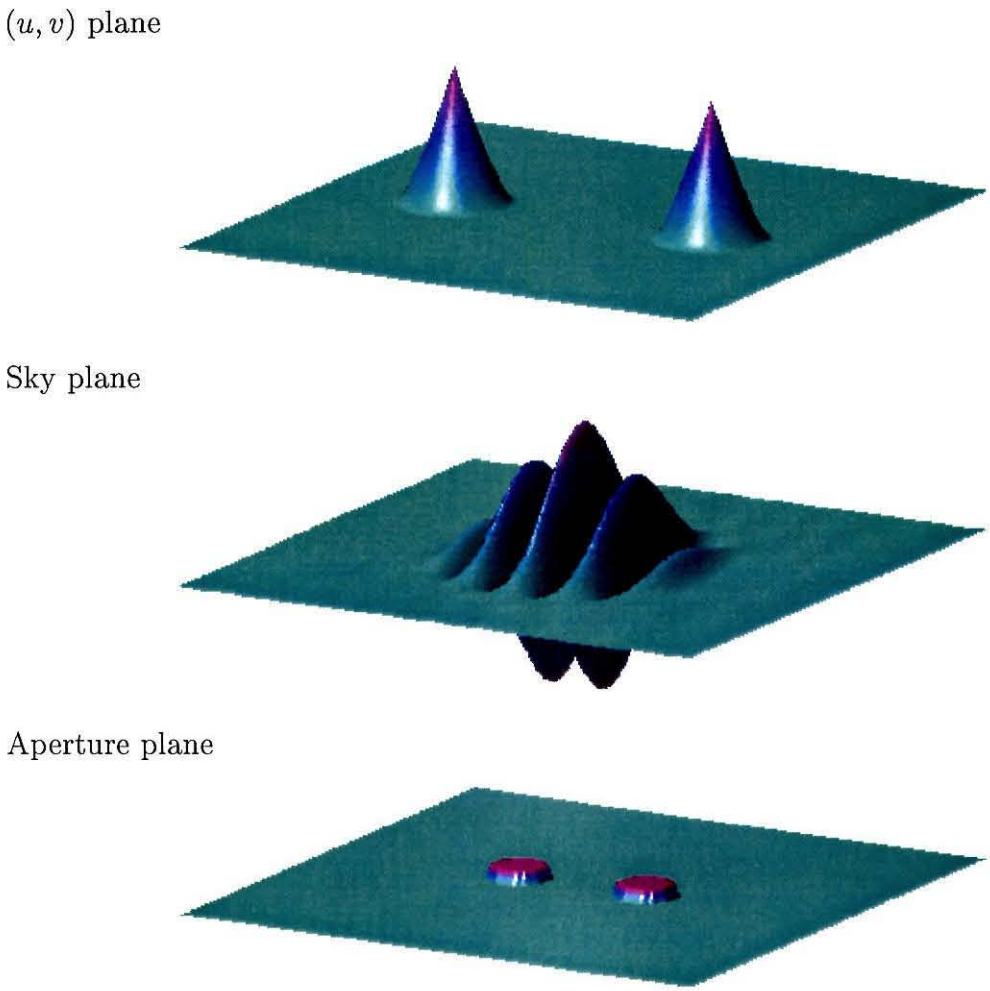

Figure 2.2 Two-element interferometer response pattern. The bottom panel depicts the aperture configuration for a simple two-element interferometer with uniformly illuminated apertures. The sky response (center panel) is a sinusoidal fringe pattern which is attenuated by the beam of a single aperture (the *primary beam*); the angular wavelength of the fringe pattern is inversely proportional to the separation (*baseline*) length $|\mathbf{b}|$ of the apertures, in units of the observing wavelength λ. The (u, v) plane (top panel) is the Fourier conjugate plane of the sky plane. The interferometer is sensitive to Fourier modes centered at $\mathbf{u} = \pm\mathbf{b}/\lambda$, with a finite width tapering to zero at $2D/\lambda$, where D is the aperture diameter. The interferometer thus makes a direct measurement of the angular power spectrum of the sky plane.

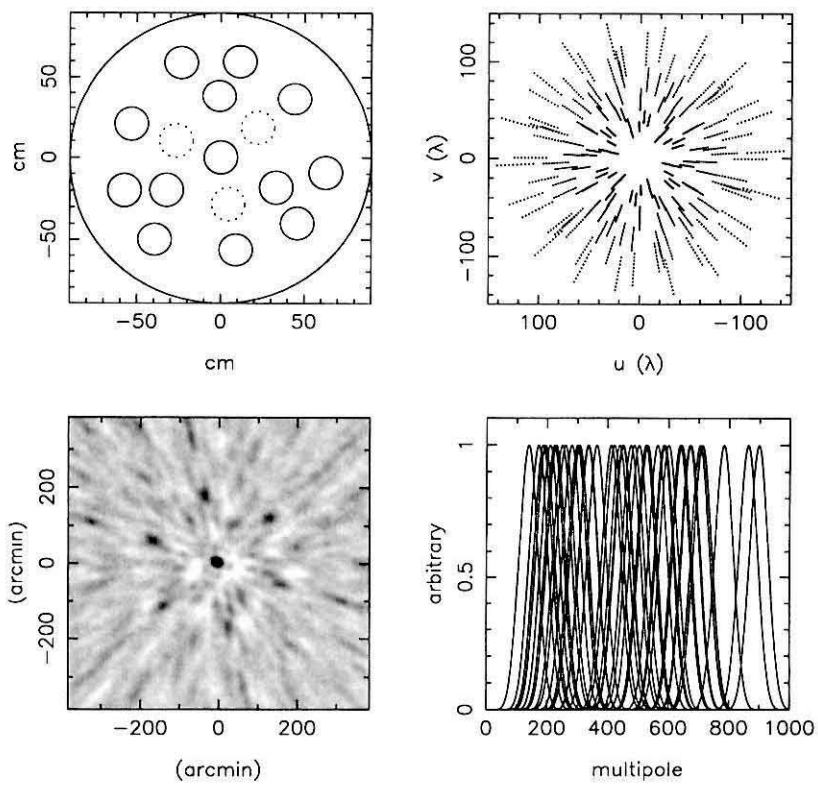

Figure 2.3 The top left panel shows the DASI aperture plate configuration (solid circles, with dotted circles representing spare holes). DASI has 13 antenna elements and 78 baselines. The aperture plane has three-fold rotational symmetry to provide redundant baseline lengths and as a check for systematics. The top right panel depicts the instantaneous (u, v) coverage; the radial lines of 10 points are a result of the 10 IF bands, which are correlated separately and increase the (u, v) plane coverage. The bottom left panel is an image of a bright point source in one of the DASI fields, representing the synthesized beam of the interferometer, and demonstrating DASI's superb imaging capability. Radial lines are an artifact of the incomplete (u, v) plane coverage. The bottom right panel depicts the window functions (each with arbitrary normalization) showing the l-range of the instantaneous angular power spectrum sensitivity for the 26 independent baseline lengths at two frequencies, 26.5 GHz and 35.5 GHz. This represents 1/5 of the 10 IF bands, which together are too dense to display.

2.4 Optics

Lensed corrugated horns were chosen as the antenna elements for DASI because of their compactness and low crosstalk characteristics. To achieve maximum sensitivity, each horn has a 20-cm aperture diameter, as large as possible within the constraint of the 25-cm minimum baseline length. The full width half power (FWHP) angle of the main beam is $3\overset{\circ}{.}4$. Corrugated horns have the advantage of an unobstructed and tapered aperture amplitude distribution with correspondingly low sidelobes, low spillover, and minimal crosstalk between elements. A diffraction limited compact horn is achieved by combining a wide-angle (30° semi-flare angle) corrugated horn with a High Density Polyethylene (HDPE) lens to collimate the phase front at the aperture.

The lens is meniscus with a refracting hyperbolic front surface, and a non-refracting spherical rear surface to match the spherical wavefront of the wide-angle horn (Clarricoats & Saha 1969). This particular lens type was chosen to increase the aperture efficiency by redistributing power toward the outside of the lens. The theoretical aperture efficiency for the DASI lensed horn is 84%, compared to 69% for an unlensed diffraction limited corrugated horn. The lens material HDPE was chosen for its desirable index of refraction, low dielectric loss, and machinability. With a loss tangent $\tan\delta \simeq 170 \times 10^{-6}$, a lens at ambient (polar) temperature contributes 2.5 K to the system noise temperature. The lens has grooves $\sim \lambda/4$ deep that act as an anti-reflection coating. Chapter 3 describes in detail the design and measurement of the DASI lensed horn. Figure 2.4 shows the DASI horn assembly and a prototype DASI receiver.

2.5 Receivers

The RF input to the receivers is in Ka band, 26–36 GHz, downconverted to a 2–12 GHz IF using an LO at 38 GHz. Each receiver uses a 4-stage InP HEMT amplifier,

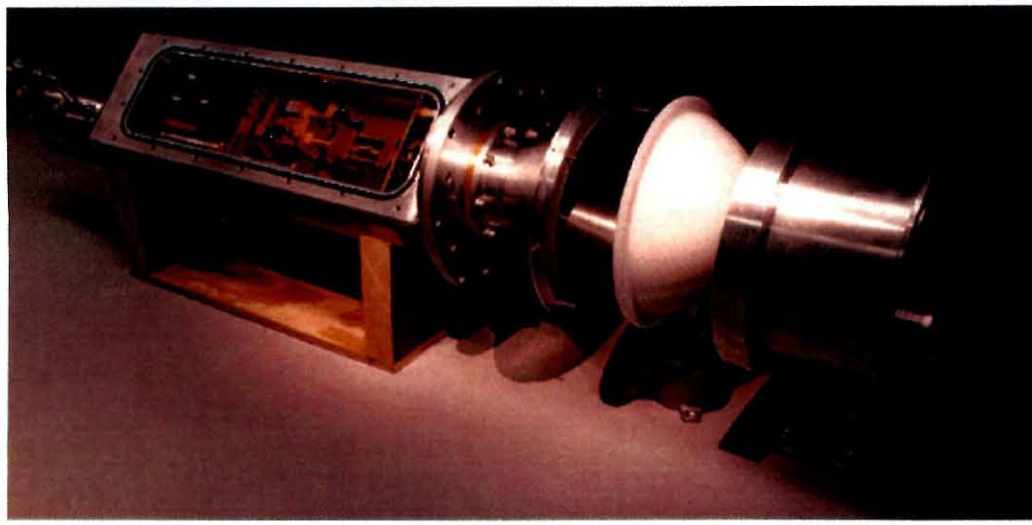

Figure 2.4 The DASI prototype Ka-band receiver assembly. The antenna element is a 20 cm diameter lensed corrugated horn which produces a 3.°4 full width half power (FWHP) beam on the sky. The receiver employs a 4-stage InP HEMT amplifier, cooled to $\sim$ 10 K by a two-stage closed cycle Helium refrigerator. A 38 GHz local oscillator (LO) downconverts the 26–36 GHz RF band to a 2–12 GHz IF output.

cooled to 10 K with a closed cycle Helium refrigerator, as the first-stage low-noise amplifier, built at the University of Chicago from an NRAO design (Pospieszalski 1993; Pospieszalski et al. 1994). We chose a robust receiver design with a waveguide vacuum break, warm lens, and warm horn throat, which slightly compromised the receiver noise temperatures. The mean measured noise temperature of the receivers is 25 K; a typical measured system temperature at the South Pole site is 30 K, including atmospheric thermal noise. The receivers are sensitive to circularly polarized light using a 1/4 wave dielectric fin in waveguide to reduce contamination from linearly polarized sources such as Galactic synchrotron emission. The receivers also employ a front-end isolator to minimize crosstalk between receivers due to correlated HEMT amplifier noise. Custom multilayered 9U $\times$ 340 mm VME cards using Altera[1] Field Programmable Gate Array (FPGA) technology are used to control the receiver mixer

[1] Altera Corporation, 101 Innovation Drive, San Jose, California 95134.

and amplifier biases, LO phaselock, and temperature monitors, as well as correlator readout. Details of the receiver design and measurement are discussed in Chapter 4.

2.6 Downconverter and Correlator

The 10 GHz bandwidth IF signal is correlated in ten 1 GHz bands to provide spectral information, to ensure flat gain across each band, and to reduce decorrelation due to finite bandwidth. The IF signal from each receiver is multi-bandpass filtered to separate the signal into ten bands, each of which is separately downconverted to 1–2 GHz (L band) and amplified in a dedicated downconverter crate. The 13×10 downconverted signals are correlated in ten identical analog correlators each of which performs the real and imaginary correlations for 78 baselines. The resulting 1560 visibilities (representing 1.56 THz of correlation bandwidth) are digitized, accumulated and read out by the control computer at 0.84-s intervals. Correlator offsets are eliminated by phase switching the 38 GHz LO between 0° and 180° in a Walsh sequence on a 25.6 μs clock interval, correcting for the sign flip in the accumulator hardware. A second level of Walsh switching is performed in software with a switching period equal to the readout interval. The analog correlators, developed at Caltech (Padin et al. 2001a) for joint use with the Cosmic Background Imager (CBI), represent a major technological achievement which gives DASI more correlation bandwidth than most observatory-class interferometers, in a single 9U VME crate which mounts behind the receiver aperture plate. Due to the fixed positions of the antennas on the aperture plate, no variable length delay lines are necessary, and the short fixed distance to the downconverter and correlator provides tremendous phase stability, with observed instrumental phase drifts less than 10° over a period of weeks.

2.7 Telescope Control and Data Handling

Telescope control and data readout are handled by a Motorola[2] VME 68060 computer board mounted inside the telescope, and running VXWorks[3], a real-time operating system. Visibility data, housekeeping data, and control commands are communicated between the VME computer and a Sun[4] workstation in a nearby control room via fiber optic ethernet cable. Data are stored temporarily on the Sun workstation; approximately 160 MB of data are transmitted to Chicago daily via a TDRS satellite internet link. Telescope motion is controlled with a PMAC[5] motion controller mounted next to the VME computer which receives input from encoders on the three axes of rotation as well as motor encoders and sends control signals to Techron[6] model 7780 amplifiers. Custom software developed at Caltech for CBI and DASI and additional software developed at the University of Chicago are used for DASI telescope control and data handling.

2.8 Mount

The telescope mount was designed and constructed in conjunction with Vertex/RSI[7], Fig. 2.5. The telescope mount was required to meet stringent pointing and tracking criteria[8], as well as endure the extreme polar environment, where temperatures average -30 C during the austral summer and -60 C during winter. The mount uses a counterbalanced gear and pinion elevation drive, and box steel plate construction

[2]Motorola, Inc., Schaumburg, IL 60196.

[3]Distributed by Wind River Systems, 500 Wind River Way, Alameda, CA 94501.

[4]Sun Microsystems, Inc., 901 San Antonio Road, Palo Alto, CA 94303.

[5]Manufactured by Delta Tau Data Systems, 9036-T Winnetka Ave., Northridge, CA 91324-3235.

[6]Manufactured by Techron, a division of Crown International Inc., Elkhart, IN 46515. The division has now been sold to AE Techron, Inc., Elkhart, IN 46516.

[7]Vertex/RSI, 2211 Lawson Lane, Santa Clara, CA 95054.

[8]The pointing error was specified as $5''$ for the azimuth and elevation axes and $30''$ for the deck rotation axis. The tracking error was specified as $1''$. These values were chosen through consideration of point source removal requirements and the angular resolution of the experiment, including a possible 90 GHz frequency upgrade. See §5.2 for actual pointing performance.

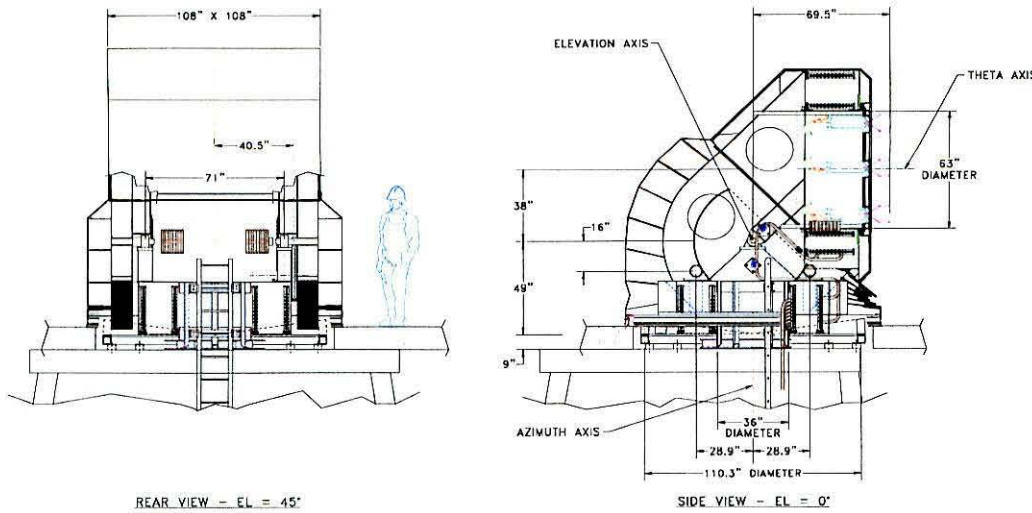

Figure 2.5 Technical drawing of the DASI telescope structure. The mount is designed to endure the extreme polar environment. The 13 receivers mount on an aperture plate which may rotate about the pointing axis; the correlator and other back-end electronics are rigidly attached at the rear of the receivers. A flexible fabric sleeve allows motion around the elevation access while keeping the telescope interior at room temperature. Access to the telescope is via a ladder from the room below.

to assure rigidity and pointing/tracking accuracy. An insulated fabric sleeve allows motion in the elevation axis while keeping the interior of the telescope and drive assemblies at room temperature.

2.9 Tower Infrastructure & Environmental Design

The DASI telescope was designed to mount atop a pre-existing tower structure attached to the Martin A. Pomerantz Observatory (MAPO) building at the South Pole. The tower structure consists of concentric inner and outer towers, which are individually free standing and vibrationally isolated. Great care was taken to design access

to the telescope in a weather-protected environment while preserving the inner tower vibration isolation (Fig. 2.6).

The interior of the telescope is accessed from below via a compressor room, which is built on the outer tower structure. The compressor room houses the 6 Helium compressors, DC drive motor amplifiers, and other electronics. This room and the interior of the telescope are heated by the $\sim$ 45 kW of waste heat from the compressors and electronics. Temperature control is accomplished by an integrated air handling unit which incorporates a heat exchanger to cool glycol from the liquid-cooled compressors, using an outside air intake. A small 5 kW electric heater, controlled by a thermostat, heats the room when the telescope electronics are off.

The telescope steel structure is covered with insulation panels consisting of 1″ thick extruded closed-cell polystyrene foam sandwiched between two 1/32″ aluminum sheets. The insulated fabric sleeve, which permits motion about the elevation axis, consists of an outer shell of polyurethane coated fabric supplied by Uretek, Inc.[9], sewn to an insulation layer and inner lining fabric made of polyester. The flexible fabric sleeve has performed well — our second-season winterover B. Reddall reports that as of July 2001, mid-way through the second winter of operation, there is no sign of cracking or fatigue in the material, although it does become stiff. The inside of the telescope maintains a comfortable temperature of $\sim$ 17 C during the winter while the compressor room hovers around 10 C. There is no ice buildup on the receiver dewars where they penetrate the telescope interior, although the interface between the dewars and aperture plate is wet due to heating of the dewars from the telescope interior. In the design stage, we were concerned about ice and fine snow buildup on the corrugated horns and near the azimuth-axis brush seal, but this has not proved to be a problem (Fig. 2.7). The apertures are covered with a 0.002″ thick Mylar window, which is kept under positive pressure with nitrogen gas; the snow accumulation brushes off easily. The compressor room is also under positive pressure, and constant outward

[9]Uretek, Inc., 30 Lenox St., New Haven, CT 06513.

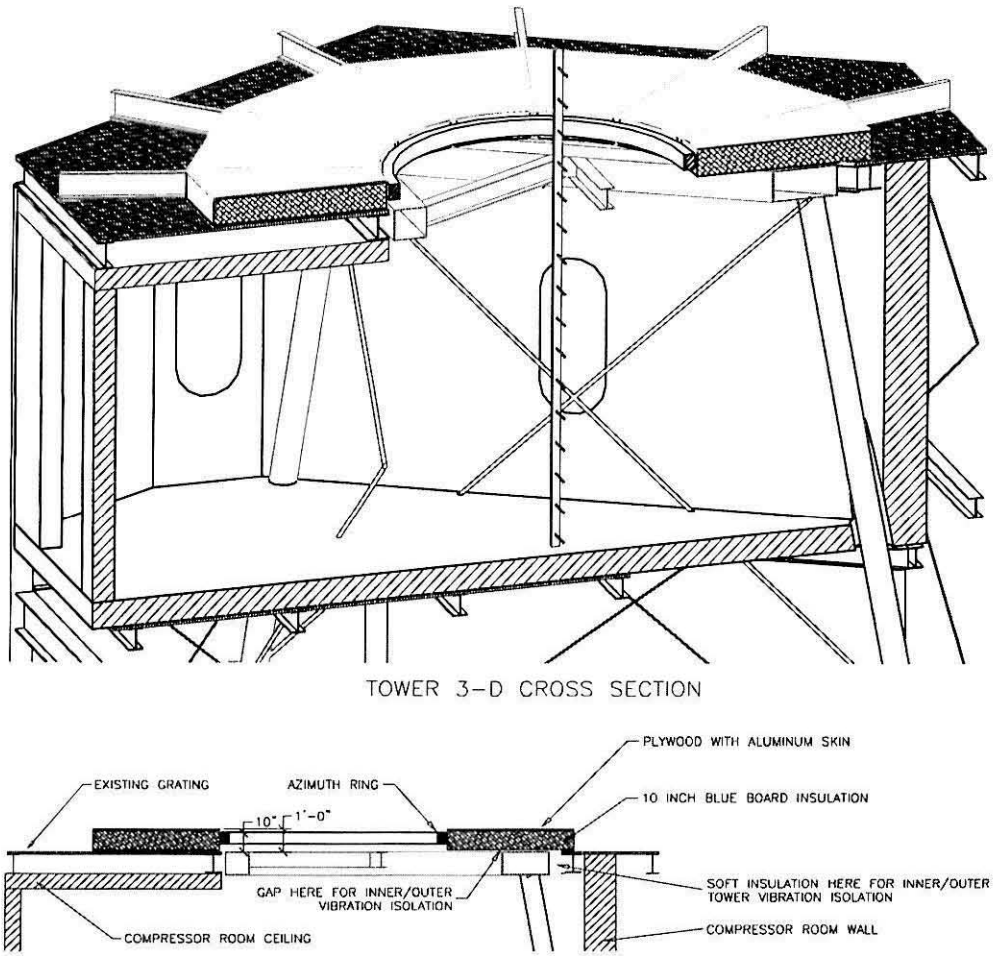

Figure 2.6 Preliminary design of the telescope-tower interface, very similar to the interface as constructed. The drawings show a cross section of the DASI compressor room, the two concentric towers, and the azimuth ring of the telescope. The compressor room is attached to the outer tower, which is vibrationally isolated from the inner tower upon which the telescope sits, with gaps between the two structures.

Figure 2.7 Winter snow accumulation around the aperture plate and azimuth-axis brush seal. The left panel shows one day of snow accumulation on the aperture plate, corrugated horns, and optical camera. Each corrugated horn is covered with a 0.002″ thick Mylar window, which is kept under positive pressure with nitrogen gas. The snow accumulation brushes off easily. The right panel shows the area near the azimuth-axis brush seal on the horizontal ground shield. Constant outward airflow from positive pressure in the compressor room sublimates snow near the brush seal and azimuth ring, preventing snow and ice accumulation.

airflow through the brush seal sublimates snow near the brush seal and azimuth ring, preventing snow and ice accumulation (Fig. 2.7). Teflon insulated wiring is used throughout the telescope wherever possible, since the PVC insulation typically used becomes brittle and shatters when flexed at polar temperatures. Overall the DASI environmental design has worked extremely well. The climate controlled telescope interior allows for easy inspection and repair by the winterover crew, and the telescope has not suffered a climate-related failure.

2.10 Telescope Deployment

The process of shipping and deployment was carefully planned and coordinated with the NSF Office of Polar Programs and its antarctic logistics contractor, Antarctic Support Associates (ASA). This collaboration resulted in a polar deployment of unprecedented speed and success. The DASI mount was delivered to Chicago by Vertex in May 1999. Initial component assembly, wiring, and drive system installation were

performed in a high-bay at the University of Chicago. The telescope was moved outside to a nearby parking lot in July 1999 to test and refine pointing and tracking capability as well as perform initial RF system integration tests. The mount was dismantled and shipped to ASA in Port Hueneme, California, in early September. It arrived at McMurdo Station, Antarctica in mid-October.

Deployment of the DASI telescope progressed rapidly after the opening of the South Pole Station in late October 1999. Telescope mount sub-assemblies were called in from McMurdo as they were needed on site. The telescope assembly was mounted atop the pre-existing tower attached to the Martin A. Pomerantz (MAPO) building in early December 1999, Fig. 2.8. The compressor room, constructed in the first part of the 1999–2000 season by ASA personnel and critical to the telescope's success in surviving the polar winter, was carefully designed and planned in a close cooperation between ASA engineers and DASI team members. The South Pole station provides excellent facility support for the telescope, including a machine shop in the MAPO building as well as engineering, construction, communications, and logistics expertise and support.

The telescope saw first light in mid-January 2000. By the end of the season in mid-February, the telescope was completely operational, with the entire complement of 13 receivers, and operational correlators in all 10 IF bands. The drive system worked well, with the telescope under full computer control. By station closing, the telescope had been calibrated using thermal loads (see §5.3), and initial CMB fields and celestial calibrator sources were being observed.

2.11 Ground Shields

Reflective angled ground shields are desirable to prevent the sidelobes of the interferometer from seeing correlated thermal noise from the ground and structures surrounding the instrument. The shield design for DASI is shown in Fig. 2.9. The

Figure 2.8 The DASI telescope being lifted to the tower attached to the Martin A. Pomerantz Observatory, 3 December 1999. The room underneath the telescope houses Helium compressors, drive amplifiers, and an air handling unit for managing waste heat from the telescope and compressors.

horizon is obscured for every element of the array at all angles greater than the minimum observing angle of 25°. The geometry of the ground shields is designed to reflect the beam of each of the antennas to the cold $\sim$ 4 K sky for all beam angles $\leq$ 90° off of the pointing axis. Several of the ground shield panels are hinged and may be lowered to the horizon to allow observations of planets (always at low elevation at the South Pole), and calibration with a fixed ground transmitter. Due to construction scheduling difficulties at the South Pole, the ground shield construction was delayed until November 2001, after the initial season of observations. However, the stability of the ground signal and instrument allowed us to eliminate ground contamination by observing multiple fields at constant elevation over the same range in azimuth. Observing strategy is discussed in Chapter 5.

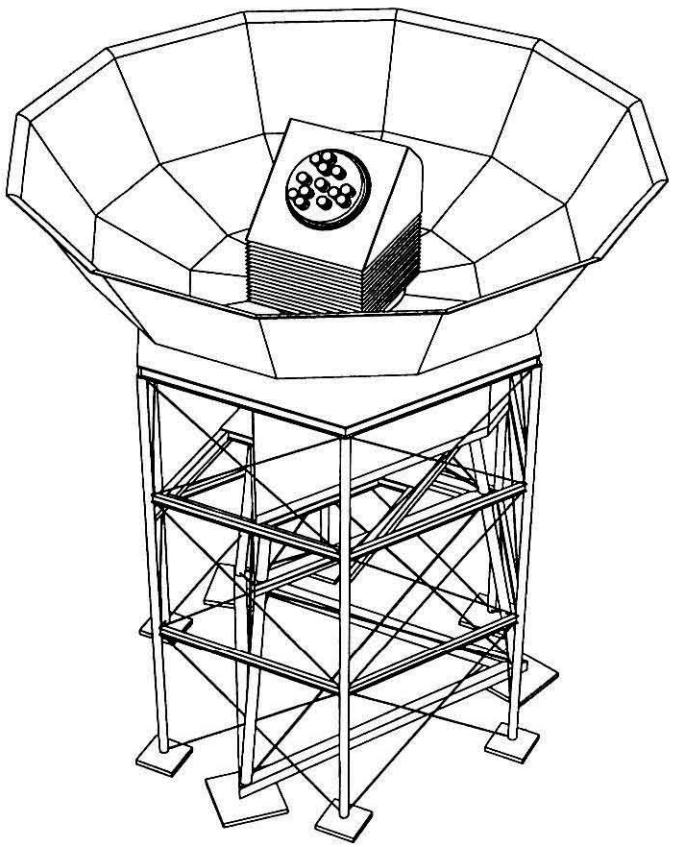

Figure 2.9 A perspective drawing of the DASI telescope on top of its tower, showing the ground shields.

2.12 The South Pole Site

The South Pole has been chosen as a site for several CMB anisotropy experiments over the past decade (see, e.g., Meinhold & Lubin 1991; Tucker et al. 1993; Dragovan et al. 1994; Platt et al. 1997; Coble et al. 1999), and has proven to be a superb site for degree-scale measurement of CMB anisotropy. It is high (2800 m), extremely cold and dry, and is situated on an expansive ice sheet, with the surface wind dominated by weak katabatic airflow from higher terrain several hundred kilometers away to

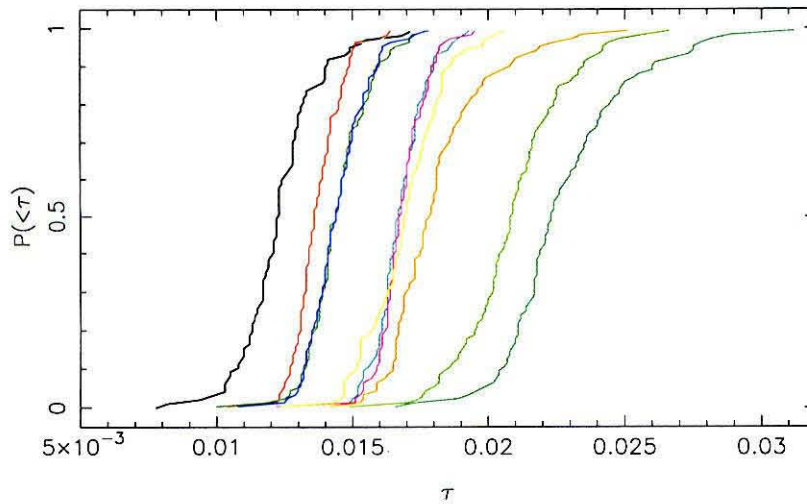

Figure 2.10 Cumulative opacity distributions at the South Pole measured by DASI during the period 05 May–07 November 2000. The ten curves are, from left to right, the ten RF frequency bands centered at 26.5–35.5 GHz.

grid northeast (see discussion in King & Turner 1997). The prevailing atmospheric opacity, as measured by DASI during its first season of observations, confirms previous assessments of the dryness of the site (Chamberlin et al. 1997), with opacity $\tau < 0.02$ at 30 GHz nearly all of the time (see Fig. 2.10).

In addition, the stability of the atmosphere is of critical importance for degree-scale CMB experiments such as DASI, since water vapor entrained in a turbulent atmosphere acts as an additional source of experimental noise. The amplitude of fluctuations in atmospheric emissivity has been compared with and found significantly better than the Cerro Chajnantor plateau in the Atacama desert of Chile, the proposed site for the Atacama Large Millimeter Array (Lay & Halverson 2000). In this study, the atmospheric fluctuations at the South Pole site are found to be bimodal in nature, with extremely smooth airflow present 75% of the time during the austral summer. Observations made by DASI during its first austral winter confirm the superb nature of the site — 95% of the time the data show little increased noise at even the largest angular scales due to atmospheric turbulence, Fig. 2.11. The

atmospheric conditions at the South Pole enable the DASI telescope efficiently and consistently to collect high quality data.

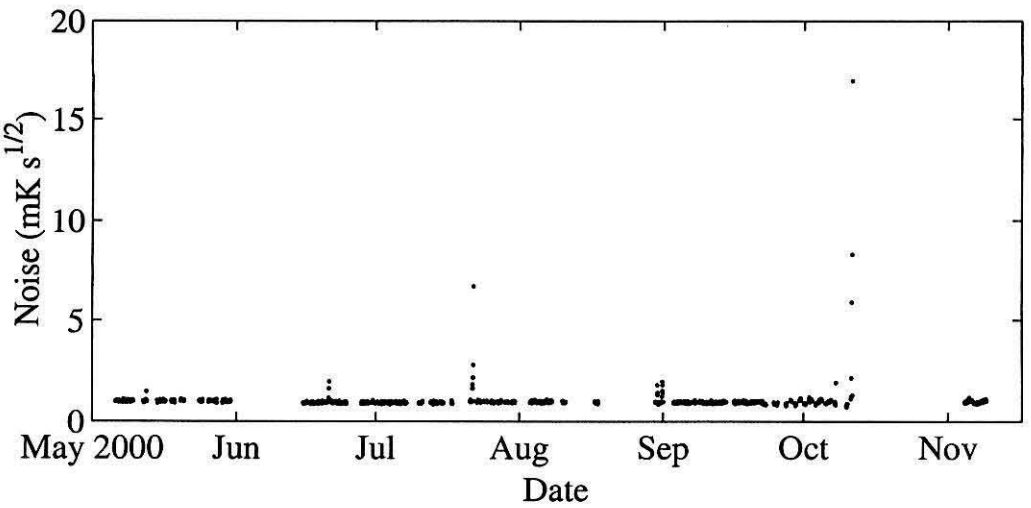

Figure 2.11 Visibility noise for the first season of observations, for one of the shortest baselines, which is sensitive to large angular scales where the atmospheric fluctuations are strongest. The data is instrument noise limited almost all of the time; only 5% of the data were edited due to weather. The noise oscillations that are apparent starting in late September are due to solar fringing (sunrise occurs around September 21 at the South Pole). Short baselines such as the one above were rejected in data where the sun was above the horizon (see Chapter 5).

Chapter 3

Optics Design

3.1 Introduction

Corrugated horns were developed as well behaved feeds for reflector antennas, but they are also used as stand-alone antennas in instruments which require an unobstructed aperture and low sidelobes. We designed a 20-cm aperture diameter lensed corrugated horn as the antenna element for DASI. The necessary sensitivity of the experiment, and the proximity of antenna elements (some are touching) require a diffraction limited aperture antenna with low sidelobes and an unobstructed aperture to reduce coupling between adjacent antenna elements. The antennas must also be broadband, operating from 26–36 GHz, have low return loss (i.e., small reflection coefficient), and be physically compact.

The antenna incorporates a 30° semi-flare angle corrugated horn with a collimating high-density polyethylene (HDPE) lens. Broadband single-mode performance in a wide semi-flare angle horn combined with low return loss is particularly difficult to achieve (see, e.g., Olver & Xiang 1988). We have avoided complex ring-loaded slots in the throat section previously described in the literature as a solution to these design criteria (Thomas et al. 1986). Instead, we have used a narrow-angle throat section incorporating tapered width slots (described in Zhang 1993) with a constant radius-of-curvature transition to the 30° flare section to achieve broadband performance ($>$ 1.4:1 single-mode bandwidth) combined with excellent return loss characteristics.

We have made measurements of the return loss, far-field beam pattern and coupling between antenna elements for the constructed DASI horn. The measured maximum in-band return loss is -20 dB with the lens in place, and -24 dB without lens, with typical values < -25 dB and < -30 dB for the lensed and unlensed horns, respectively. This is considerably better performance than previously reported wide-angle horns in the literature using more conventional throat designs (Olver & Xiang 1988). We find that a simple approximation of the aperture field distribution for the wide-angle horn combined with the Fourier transform method for calculating the far-field is adequate to accurately predict the beam pattern of both the lensed and unlensed horn. Good isolation between adjacent coplanar horns is critical in our application; we measure this coupling to be < -100 dB across the band.

This chapter describes the design and measurement for a wide-angle lensed corrugated horn with low return loss. In §3.2 we outline previous work on both wide-angle corrugated horns and broadband single-moded horns with low return loss. In §3.3, we give the design procedure of the lensed corrugated horn, and in §3.4, we show measurement results of the constructed antenna, including return loss, beam pattern, and coupling measurements between adjacent horns.

3.2 Review of Previous Work

3.2.1 Fundamental Principles of Corrugated Horns

An excellent review of the principles of corrugated horns is given by Zhang (1993). For a more comprehensive discussion, the reader is referred to a book on the subject by Clarricoats & Olver (1984). To a good approximation, a corrugated horn has an aperture amplitude distribution of the zeroth order Bessel function, truncated at its first zero,

$$F(\theta) = J_0\left(\alpha_{01}\frac{\theta}{\theta_{\rm f}}\right), \tag{3.1}$$

where $\alpha_{01} = 2.405$ is the first zero of the zeroth order Bessel function, θ_f is the semi-flare angle of the corrugated horn, and the horn is assumed to be radiating in the fundamental HE_{11} hybrid mode under balanced conditions. The amplitude distribution $F(\theta)$ is on a spherical wavefront at the aperture of the horn; the radius of curvature of the wavefront is determined by the slant length R of the horn. This aperture distribution has the desirable characteristics that it is symmetric in the E- and H-planes, tapers smoothly to zero at the edge of the aperture, and is linearly polarized. A more accurate expression for the aperture amplitude distribution for horns with semi-flare angles $\gtrsim 10°$ is derived in Clarricoats (1969) using spherical hybrid modes. We have calculated the maximum fractional error, out to the -20 dB level in the aperture amplitude, between the simple expression in Eq. (3.1) and that derived in Clarricoats (1969). We found a maximum fractional error of 0.5%, 1.9%, 4.1%, and 6.9% for semi-flare angles of 15°, 30°, 45°, and 60°, respectively. The approximation for the aperture amplitude distribution in Eq. (3.1) is therefore very good for horns with moderate semi-flare angles.

A sometimes confusing distinction is made in the literature between narrow and wide flare-angle horns, although both have the aperture field described above. The far-field beam pattern characteristics differ for the two types of horn, being determined predominantly by diffraction of the aperture amplitude distribution for narrow flare-angle horns, and by the spherical phase front at the aperture for wide flare-angle horns. In both regimes, the beams are circularly symmetric, linearly polarized, and have low sidelobes due to the well tapered aperture distribution. Wide flare-angle corrugated horns are often used as feeds for reflector antennas because their beamwidth is independent of frequency—the aperture of the horn is already in the far-field of the beam waist, so the semi-flare angle θ_f determines the beamwidth and the Gaussian beam waist is fixed at the apex of the conical flare. Because of these properties, wide flare-angle corrugated horns are often referred to in the literature as "wide-band"

or "broadband" horns. In this work, however, we use the term broadband in reference to the frequency bandwidth over which a corrugated horn is single-moded and well-behaved, regardless of its flare angle.

The propagation modes in a corrugated horn can be thought of as a superposition of circular waveguide TE and TM modes. In smooth wall circular waveguide, the guide wavenumber $\beta = 2\pi/\lambda_g$ and cutoff wavenumber k_c of TE and TM modes of corresponding order are different. In corrugated waveguide, however, the boundary conditions (or "surface impedance") at the waveguide wall are anisotropic, allowing the cutoff wavenumbers of the corresponding TE and TM modes to converge. The azimuthal slots are designed to have a depth $d \approx \lambda_0/4$, where λ_0 is the free-space design wavelength, so that the electrical short at the outer radius b of the slot is transformed to an electrical open at the inner radius a (Fig. 3.1). This imposes the boundary conditions

$$H_\phi = 0 \tag{3.2}$$

$$E_\phi = 0 \tag{3.3}$$

$$H_z \neq 0 \tag{3.4}$$

$$E_z \neq 0 \tag{3.5}$$

at the corrugated waveguide inner wall, $r = a$.

The symmetry in the boundary conditions (and in Maxwell's equations) for the E- and H-fields produces corresponding symmetry in the E- and H- fields at the aperture. Since the slots present an open at the inner radius a, $H_\phi/E_z = 0$ and no longitudinal currents flow. This has the effect of tapering both the E- and H-fields to zero at the waveguide wall. The resulting modes are "balanced hybrid" modes, consisting of a superposition of TE and TM circular waveguide modes, with equal amplitudes of the longitudinal fields, $E_z = Z_0 H_z$, where Z_0 is the impedance of free space. In HE hybrid modes the TE and TM modes are in phase; in EH hybrid modes they

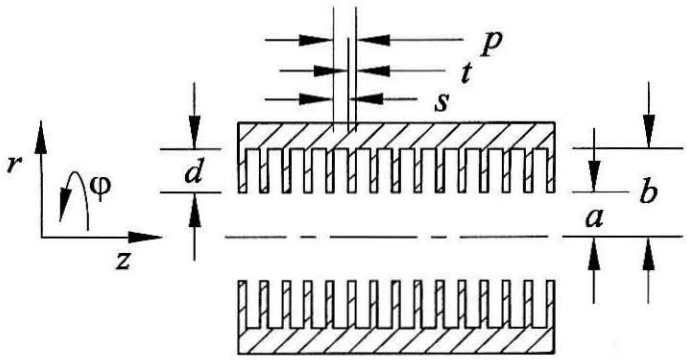

Figure 3.1 Geometry of corrugated waveguide.

are π radians out of phase. The HE modes are the desirable modes because they are linearly polarized; EH modes are not. Away from the design wavelength λ_0, one circular waveguide mode dominates over the other, leading to non-zero fields at the waveguide wall and, in the case of the HE modes, a non-zero E-field component in the orthogonal plane or *crosspolarization*. The fundamental HE_{11} mode described in Eq. (3.1) is the one most often used in corrugated horns, but higher order modes may be used as well. The mode launching region, or throat, of the horn must be designed to excite desired modes and suppress undesired ones. The dispersion curves of the first few HE and EH modes are shown in Fig. 3.2.

3.2.2 Broadband Throat Design

The throat of the corrugated horn provides the transition between the boundary conditions of the smooth wall circular waveguide, and the anisotropic boundary conditions necessary for propagation of the desired balanced HE_{11} mode. In order to reduce return loss, a common practice is to taper the slot depths in the throat from $\lambda/2$ at the first slot (presenting a short at the inner wall) to $\lambda/4$ at the output of the

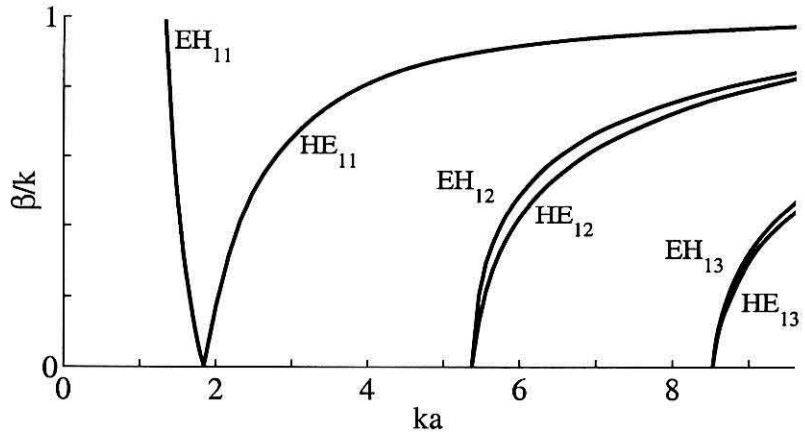

Figure 3.2 Dispersion curves for the first few corrugated waveguide hybrid modes under the balanced hybrid condition, from Zhang (1993). The vertical axis β/k is the ratio of guide wavenumber to free space wavenumber, and ka is the product of the free space wavenumber and the inner diameter of the corrugated waveguide.

throat (Fig. 3.3a). The first slot is designed to be $\lambda/2$ at the high end of the band, so that the slot presents a capacitive (negative) reactance throughout the band of operation to avoid excitation of the EH_{11} "surface wave" mode which can be excited when the surface impedance is inductive. This type of throat design is limited at low frequencies by increased return loss near the cutoff of the HE_{11} mode and at high frequencies by the introduction of undesired higher order modes, either by the inductive reactance of the first slot (producing EH_{11}) or by the changing reactance of the slots in the tapered transition (usually exciting EH_{12}).

One method of increasing the bandwidth of the throat, first implemented by Takeichi et al. (1971) and detailed by James & Thomas (1982), is to produce the desired taper in the waveguide wall boundary conditions using ring-loaded slots (Fig. 3.3b) instead of a simple taper in slot depth. This has the effect of attaining a surface impedance at the first slot that is small and capacitive over a much broader range of frequencies. Ring-loaded slots are difficult to machine, however, making the method impractical for many applications.

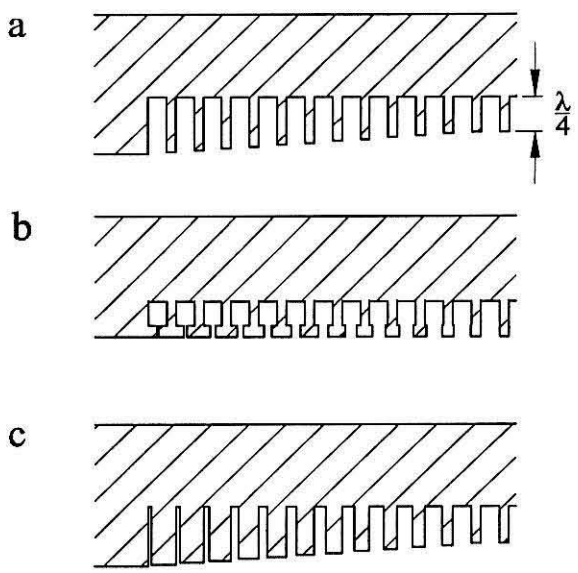

Figure 3.3 Cross sections of three throat types from the literature, which perform the mode conversion between smooth-walled circular waveguide and corrugated waveguide: a) mode conversion employing a taper from $\lambda/2$ to $\lambda/4$ corrugation depth with constant slot width, b) mode conversion using ring loaded slots, c) similar to a), but also employing a taper in slot width.

Another method of increasing the bandwidth, detailed by Zhang (1993) and depicted in an earlier paper by Goldsmith (1982), is to taper the width as well as the depth of the slots (Fig. 3.3c). In the surface impedance approximation, where the pitch $p \ll \lambda/2$, the effective impedance of the waveguide wall is approximately

$$Z_s = jX_s \approx jZ_0 \tan(\beta_{cyl} d) \left(\frac{s}{p}\right), \tag{3.6}$$

where s is the slot width of the corrugations and β_{cyl} is the wavenumber in the cylindrical slot (not to be confused with the guide wavenumber β). The narrow slot widths at the input of the throat have the effect of reducing the frequency dependence of the impedance of the narrow $\lambda/2$ slots, keeping the reactance small and capacitive over a broader range of frequencies. Zhang also argues that the increased distance between the slots in this design diminishes interaction between adjacent slots, improving the

validity of the surface impedance model above.

Zhang has successfully implemented the above throat design for a 12° semi-flare angle horn, measuring a return loss < -30 dB over a bandwidth ratio of 1.4:1. However, she also models return loss for wider flare angles by treating each individual slot and ridge as a section of circular waveguide, and cascading the individual scattering matrices (so-called *modal matching*) to estimate the overall return loss of the horn. She finds that the discontinuity in the flare angle at the output of the horn causes high return loss: -14.2 dB for a 21° semi-flare angle horn and -1.4 dB for a 25° semi-flare angle horn. One may doubt the accuracy of the -1.4 dB figure since even a simple open ended waveguide with the dimensions of the output of the throat has substantially lower return loss; nevertheless, one is cautioned by these numbers against implementing Zhang's design directly in a wide flare-angle horn.

3.2.3 Return Loss in Wide Flare-Angle Horns

Wide flare-angle horns (with semi-flare angle $\theta_f \gtrsim 20°$) are difficult to design for broadband single-mode performance and low return loss because the rapidly increasing inner diameter in the flare gives rise to an impedance mismatch, and may excite undesired higher order modes. Olver & Xiang (1988) have analyzed three types of throat for wide angle corrugated horns using spherical modal matching. They conclude that the throat that yields the best compromise between return loss and generation of higher order modes consists of a short section of smooth wall conical waveguide preceding the first $\lambda/4$ slot. However, for a 30° semi-flare angle horn, they report a theoretical and measured return loss of -14 dB and -12 dB, respectively, at the low-frequency end of the band, 10% below the design frequency. In an earlier paper, Thomas (1978) measured a return loss of -16 dB for a 45° semi-flare angle horn at the low-frequency end of the band. This was improved to -19 dB by tapering the depth of the slots in the throat from $\lambda_H/2$ (where λ_H is the wavelength at the high frequency limit f_H) to $\lambda_0/4$. Olver & Xiang modeled this type of throat as well,

but concluded that it would result in significant generation of higher order modes.

Thomas et al. (1986) have successfully implemented a broadband wide flare-angle horn design using ring-loaded slots in the throat and a constant radius-of-curvature transition from the narrow flare angle in the throat to the wide flare angle at the output flare. They report a measured return loss < -30 dB over a bandwidth ratio $> 1.7{:}1$. While we wish to avoid the complication of ring-loaded slots in the present design, we have incorporated Thomas, James & Greene's criteria for a constant radius-of-curvature throat-flare transition section into our wide flare-angle horn design to provide low return loss over a broader frequency range than that achieved with the other wide flare-angle corrugated horn designs above.

3.2.4 Lensed Corrugated Horns

Dielectric lenses designed using geometric optics have been successfully implemented to change the phase front curvature at the mouth of a wide flare-angle corrugated horn (see, e.g., Padman 1978; Kildal et al. 1984). Clarricoats & Saha (1969) have investigated two types of simple lenses (where one surface is the refracting surface and the other surface is matched to the phase front of the beam) to collimate the phase front of the corrugated horn. One of these lenses, the meniscus simple lens, is shown in Fig. 3.4. The refracting surface is designed using Fermat's principle. The lens, which is used in the present design, has a spherical rear surface and a front surface described by

$$\rho(\theta) = f\frac{(n-1)}{n-\cos\theta}, \tag{3.7}$$

where n is the index of refraction of the dielectric, and the other variables are depicted in Fig. 3.4. The valid range of semi-flare angles in Eq. (3.7) is $\theta_f \leq \cos^{-1}(1/n)$.

The lens also has the effect of redistributing the power in the aperture plane,

$$F_{ap}(r) = F_{corr}(\theta)\sqrt{\frac{\sin\theta}{r}\frac{d\theta}{dr}}, \tag{3.8}$$

where $F_{ap}(r)$ is the lens-modified aperture field as a function of radius, and $F_{corr}(\theta)$

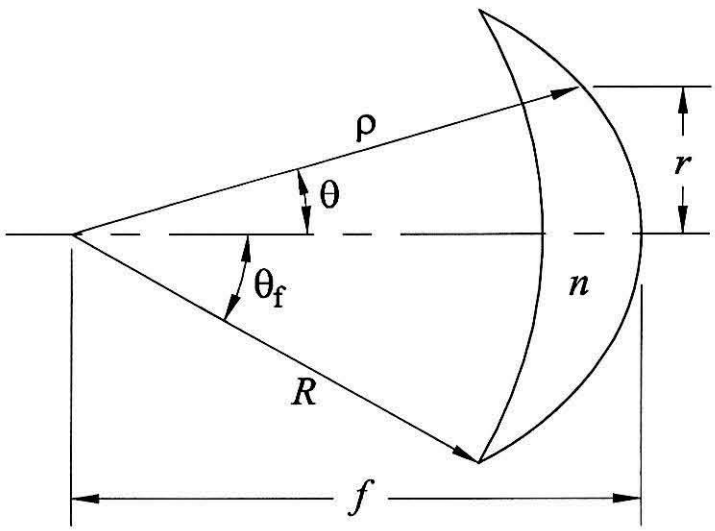

Figure 3.4 Geometry of a meniscus lens.

is the field amplitude of the unlensed corrugated horn as a function of angle [see Eq. (3.1)]. For the meniscus lens described above, power is redistributed toward the edge of the aperture. The modified aperture field distribution is then

$$F_{\rm ap}(r) = F_{\rm corr}(\theta)\sqrt{\frac{(n\cos\theta - 1)^3}{f^2(n-1)^2(n-\cos\theta)}}, \tag{3.9}$$

where

$$\theta(r) = \cos^{-1}\left(\frac{r^2 n + f(n-1)\sqrt{f^2(n-1)^2 + (1-n^2)r^2}}{f^2(n-1)^2 + r^2}\right). \tag{3.10}$$

The resulting aperture efficiency is given by (Collin 1985)

$$\eta_{\rm a} = \frac{1}{A_{\rm p}}\frac{\left|\int d\mathbf{x} F(\mathbf{x})\right|^2}{\int d\mathbf{x}\,|F(\mathbf{x})|^2}, \tag{3.11}$$

where $A_{\rm p} = \pi D^2/4$ is the physical aperture area, and the integrals are over the two-dimensional aperture plane. This lens has the effect of increasing the aperture efficiency above that of an unlensed diffraction limited corrugated horn. Another useful quantity in radio astronomy is the antenna gain expressed as antenna temperature

per unit unpolarized point source flux density. This gain, expressed in units of K/Jy, is given by

$$G = \frac{10^{-23} A_{\rm p} \eta_{\rm a}}{2 k_B} \ \ ({\rm K/Jy}) \tag{3.12}$$

where k_B is Boltzmann's constant. The factor of 1/2 is due to the assumption that the antenna is assumed to be sensitive to only a single polarization mode. For a given physical area $A_{\rm p}$, the gain G is proportional to the aperture efficiency $\eta_{\rm a}$.

To avoid reflections from the surfaces of the lens, the lens surface may be drilled or grooved to simulate a $\lambda/4$ anti-reflecting coating. We have chosen to machine rectangular profile concentric grooves to accomplish this, after Morita & Cohn (1956).

3.3 Design of the DASI Lensed Corrugated Horn

The DASI interferometer requires physically compact, diffraction limited antennas with low sidelobes and unobstructed apertures to reduce coupling between adjacent antenna elements, some of which are touching. Because of the high sensitivity of the experiment, we desire an antenna with a return loss < -20 dB and which contributes $\lesssim$ 3–4 K to the overall system temperature. With the optics at an ambient temperature of $\sim$ 230 K (the mean temperature at the South Pole where DASI is deployed), this translates into a desired attenuation in the antenna of less than 0.07 dB.

To meet these requirements, we have designed a lensed corrugated horn antenna consisting of a 30° semi-flare angle corrugated horn, with a meniscus high-density polyethylene (HDPE) lens at the 20-cm diameter aperture of the horn to collimate the beam, producing a 3.°4 FWHM beam at the design frequency of 30 GHz. An exploded view of the DASI lensed corrugated horn is shown in Fig. 3.5. The DASI lensed corrugated horn consists of four separate parts: the throat section, flare section, lens, and shroud. The entire length of the lensed horn antenna is only 33.6 cm. We have achieved low return loss (< -20 dB at the low end of the band) in a moderately broadband horn (1.4:1) by combining a tapered width slot design in the throat with

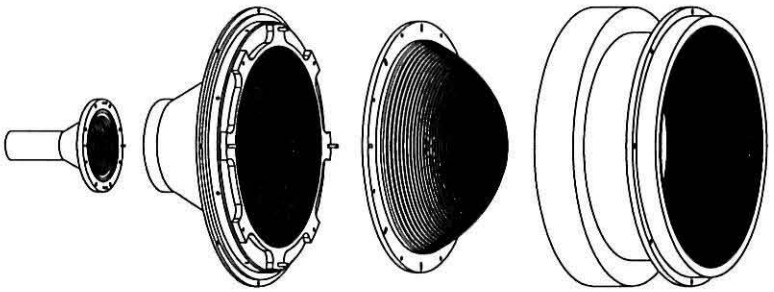

Figure 3.5 An exploded view of the DASI lensed corrugated horn.

a constant radius-of-curvature throat-flare transition. The lens is enshrouded by a corrugated cylindrical shroud to reduce coupling between antennas while avoiding a significant alteration of the beam.

3.3.1 Design of the Wide-Angle Horn

The DASI horn throat consists of two regions, a narrow-angle mode-converter section with tapered-width slots, and a throat-flare transition section where the narrow flare angle of the mode-converter section is converted to the output flare angle θ_f with a constant radius of curvature. Below, we give specific design criteria and parameters for the throat shown in Fig. 3.6.

Aperture Diameter D and Semi-flare Angle θ_f

We chose an aperture diameter $D = 20$ cm to be as large as possible given the minimum antenna separation of ~ 25 cm, in order to maximize the filling factor of the aperture plane. The horn semi-flare angle $\theta_f = 30°$ was chosen as a compromise between our desire for compactness, and the requirements of low return loss and a well behaved beam over the band.

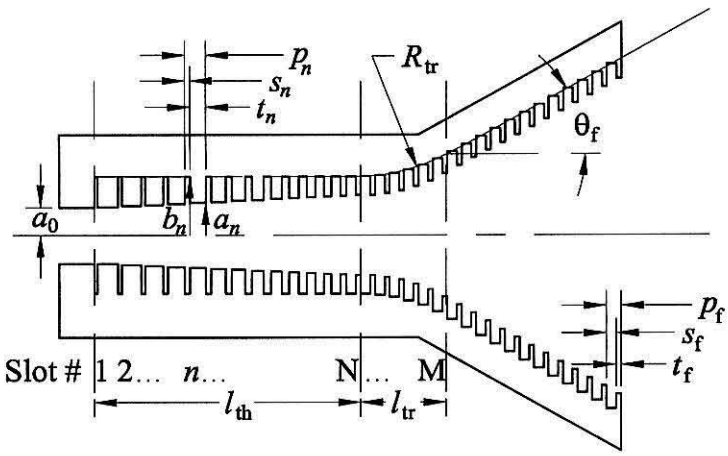

Figure 3.6 Geometry of the DASI corrugated horn throat.

Design Frequency f_0

The design frequency $f_0 = c/\lambda_0$ was chosen to minimize crosspolarization at the edges of the band, a concern since we observe circular polarization and desire to minimize susceptibility to linearly polarized foregrounds[1]. The crosspolarization is primarily due to imbalance in the HE_{11} mode, $\gamma \neq 1$, where γ is the hybrid factor (see Zhang (1993); Clarricoats & Olver (1984) for a discussion of the hybrid factor and Clarricoats & Olver (1984) for details of crosspolar radiation characteristics). An expression for the peak crosspolarization is

$$P_{\rm cr} = 20 \log \left(0.26 \left| \frac{\gamma - 1}{\gamma + 1} \right| \right). \tag{3.13}$$

In general, the hybrid factor γ is derived by numerically solving a transcendental equation. For $ka \gg 1$, γ can be approximated by

$$\gamma \approx 1 - \frac{(k_c a)^2}{2ka} \frac{Z_0}{X_s} \tag{3.14}$$

[1]We are observing CMB polarization during the 2001 season; for these measurements, low crosspolarization is critical in minimizing response to unpolarized CMB radiation.

$$\approx 1 - \frac{(k_c a)^2}{2ka} \cot(kd) \left(\frac{p}{s}\right), \tag{3.15}$$

where $k_c a = 1.84$ of the HE_{11} balanced hybrid mode can be used instead of that of the imbalanced hybrid mode, with an error of a few dB. The design frequency that minimizes the peak crosspolarization at the edges of the band is $f_0 = 30$ GHz, yielding an estimated -55 to -60 dB peak crosspolarization at the edges of the band. This should be taken as a lower estimate, as crosspolarization due to introduction of higher order modes may dominate.

Slot Geometry in the Flare

The pitch in the flare section p_f must be sufficiently fine that only the lowest order TM mode propagates in the slot, $s_f < \lambda/2$, and that the surface impedance model is well approximated ($p_f \ll \lambda$). Using modal matching simulations, Zhang establishes the criterion that $p_f/\lambda < 0.43$ at the high end of the band, to avoid generation of higher order modes. We have chosen $p_f/\lambda_L = 0.225$, where $\lambda_L = c/f_L$ is the wavelength at the low-frequency limit. This pitch that is fine enough to make the radius in the throat-flare transition well defined in order to reduce the return loss. A wide range of ridge-width to slot-width ratios may be successfully used; we used $t_f/s_f = 0.5$.

The slot depth in the flare, d_f, is chosen to give an effective wall impedance near infinity at the design frequency f_0. The slot depth d_f is nearly $\lambda_0/4$, but differs slightly from this value for two reasons. First, $\beta_{cyl} < k$ for $ka \sim 1$; Fig. 3.7 shows this effect as a function of ka, calculated using the TM_1 cylindrical slot mode. Second, interactions between the slots alter the effective impedance. In order to derive the optimal value of d_f, space harmonic analysis must be used. Design graphs for slot depth corrections, given the aperture normalized aperture diameter D/λ_0, normalized slot width s_f/λ_0 and ridge-width to slot-width ratio t_f/s_f are given in Clarricoats & Olver (1984). For $D/\lambda_0 \gtrsim 6$ and $t_f/s_f > 0.5$, negligible correction from the nominal $\lambda_0/4$ depth is needed. For our design, $d_f/\lambda_0 = 0.26$.

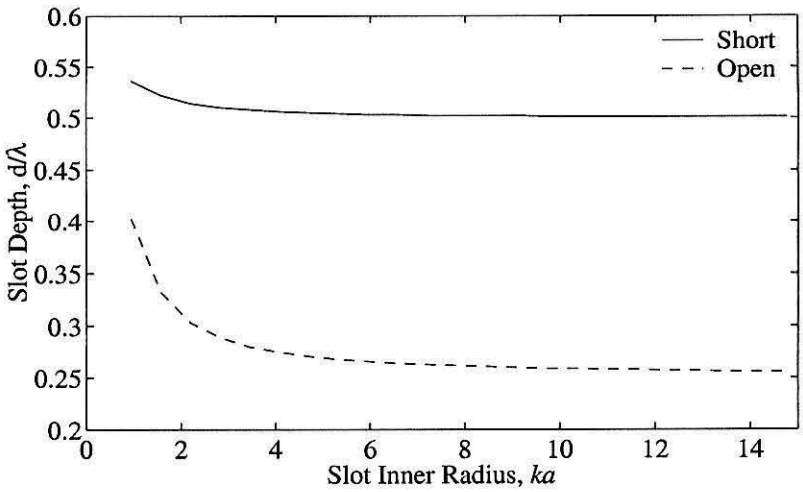

Figure 3.7 Cylindrical slot depth necessary for presenting an open or short at the inner radius a, calculated using the TM_1 cylindrical slot mode. The impedance calculation neglects interactions between slots, which are significant in the flare section where the ridge-width to slot-width ratio is near unity ($t_f/s_f \sim 1$). However, this design graph is adequate for the first slot in the throat where $t_1/s_1 \gg 1$.

Throat-flare Transition Design

The throat-flare transition was designed using criteria from Thomas et al. (1986). Specifically:

- The length of the transition, l_{tr}, must be greater than one wavelength, to reduce return loss.
- The radius of curvature, R_{tr}, must be constant, preferably with constant slot depth, to avoid excitation of EH_{1n} modes.
- A change in flare angle must be avoided at a large waveguide radius, since higher order HE_{1n} modes are excited by a change in horn curvature.

These criteria impose the usual compromise between decreasing return loss with a longer, more gentle transition, and generating higher order modes if the output of the

transition is too large. We restricted the transition length, therefore, to be exactly one wavelength at the low end of the band,

$$l_{\rm tr} = 1.0\lambda_{\rm L}. \tag{3.16}$$

The radius of curvature of the transition is then

$$R_{\rm tr} = \frac{l_{\rm tr}}{\sin(\theta_{\rm f})}. \tag{3.17}$$

The outer slot radius b_M at the output of the transition must be kept in mind when specifying the initial slot radius in the throat, b_1, such that b_M is near or below the HE_{12} cutoff radius, $kb = 7.0155$ in the balanced hybrid condition. The outer slot radius b_M at the output of the transition is given by

$$b_M = b_N + R_{\rm tr}(1 - \cos(\Delta\theta)) \tag{3.18}$$

where b_N is the outer slot radius at the input of the transition, and $\Delta\theta$ is the change in semi-flare angle between the input and output of the transition. In our case, b_n is constant for $n = 1, 2, \ldots, N$ so the flare angle at the input is zero, and $\Delta\theta = \theta_{\rm f}$. In our design, $k_{\rm H} b_M = 8.088$. The slot width s, pitch p and slot depth d in the throat-flare transition are constant and equal to their values in the flare section.

It is not critical that the output of the transition be below the HE_{12} cutoff. Thomas et al. (1986) measured deviation from the expected beam amplitude at an angle of 30° for their 30° semi-flare angle horn, which places limits on the level of contamination of HE_{12} mode. They found a deviation less than 2 dB, even though the input of their transition was above HE_{12} cutoff at the high end of the band.

Throat Input Radius

The throat input radius, a_0, was chosen as a compromise between the desire to suppress the generation of unwanted higher order modes in the throat and throat-flare transition, and the desire for low return loss at the low end of the band. A rough

estimate of the return loss can be achieved by considering the reflection at the junction between circular waveguide and corrugated cylindrical waveguide of the same diameter and slot geometry of that of the initial slot. The return loss can then be estimated by the examining the propagation constants in the two waveguides which have different frequency dependence. The return loss, S_{11}, is given by Clarricoats & Olver (1984),

$$S_{11} = 20 \log \left(\left| \frac{\beta_1 - \beta_2}{\beta_1 + \beta_2} \right| \right) \quad \text{dB} \tag{3.19}$$

where β_1 and β_2 are the propagation constants in the two waveguides. Propagation constant curves for corrugated slot geometry with $s = 0.1\lambda$ and $t = 0.05\lambda$, derived using space harmonics analysis, are given in Clarricoats & Olver (1984). The large ridge-width to slot-width ratio, t_1/s_1, of our throat design improves the return loss by lessening the frequency dependence of wall impedance. A better estimate of the return loss due to the first slot (see Fig. 3.8) assumes a wall impedance given by Eq. (3.6); the propagation constant β in the corrugated waveguide is then calculated using the characteristic equation for the surface impedance model given in Clarricoats & Olver (1984). This estimate does not take into the account reflections off of other discontinuities in the throat, such as the throat-flare transition. A more accurate estimation of the return loss in the horn could be done using modal matching techniques, which we have not performed. We chose a throat input radius, $k_0 a_0 = 2.515$.

Throat Input Slot Geometry

The initial slot depth was chosen so that the wall impedance is zero at the high-frequency edge of the band, with a resulting negative wall reactance throughout the band to avoid the generation of the EH_{11} mode. Using the surface impedance model for the wall impedance, Eq. (3.6), is justified when the initial ridge-width to slot-width ratio is large, $t_1/s_1 \gg 1$, since there is minimal interaction between slots (Zhang 1993). Using cylindrical slot mode calculations (Fig. 3.7), the desired slot depth to produce a short at $\lambda_H = c/f_H$ is $d_1 = 0.509\lambda_H = 0.424$ cm for the above

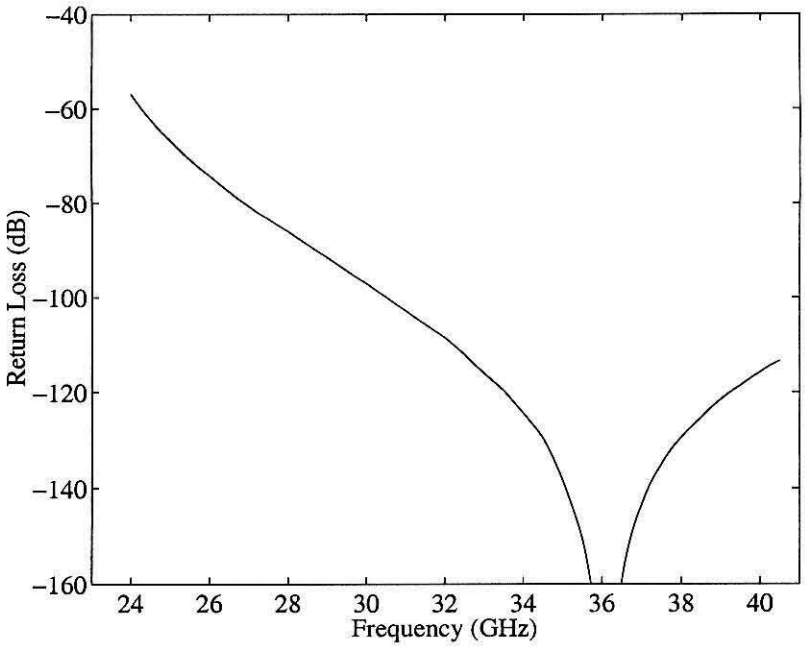

Figure 3.8 The estimated return loss for the DASI throat design due to the impedance discontinuity of the first slot, Eq. (3.19). This simple estimate of the return loss is a lower limit, since the return loss is dominated by other discontinuities, such as the throat-flare transition.

input radius. The initial ridge-width to slot-width ratio t_1/s_1 should be large enough to keep the return loss low over a wide frequency range, in addition to satisfying the above criterion. We chose $t_1/s_1 = 6.63$, close to Zhang's tested throat design.

The throat section of the horn was constructed by electroforming over a mandrel. We set the aspect ratio of the first slot to 10:1 ($d_1/s_1 = 10$) to ensure proper etching of the mandrel. The pitch of the first slot is then $p_1 = 0.320$ cm, so that $p_1/\lambda_H = 0.384$, larger than the pitch in the flare section. Over the length of the throat, l_{th}, the inner radius a_n, the slot width s_n, and the pitch p_n are linearly tapered from their initial values to their final values at the input of the throat-flare transition. Following Zhang, we made the length of the throat several wavelengths long, $l_{th}/\lambda_0 = 3.21$, to sufficiently attenuate evanescent modes and allow for a gradual taper of the slot parameters.

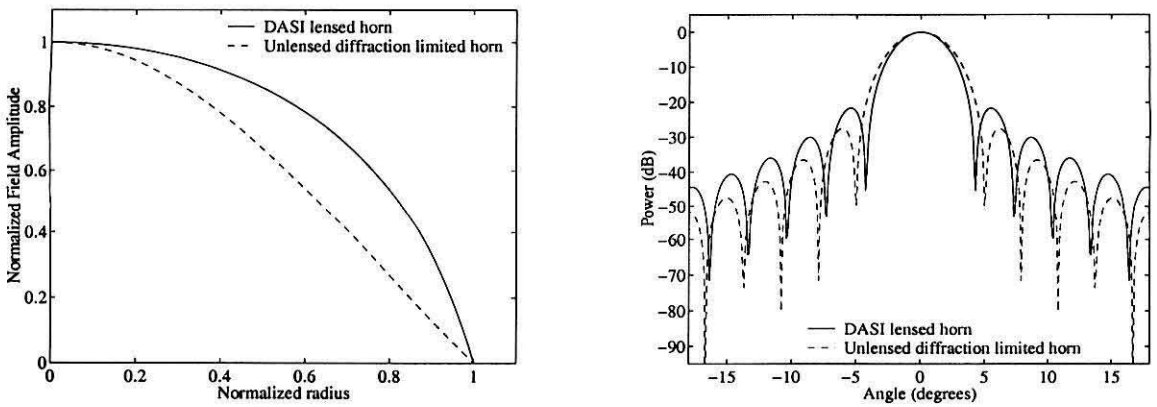

Figure 3.9 Comparison of the theoretical aperture E-field distribution and beam patterns for the DASI lensed horn and an equivalent unlensed diffraction limited horn (i.e., with equivalent aperture diameter and a semi-flare angle $\theta_f \ll 30°$). The meniscus lens redistributes the field toward the edge of the horn, increasing the aperture efficiency to 84% compared to 69% for the unlensed horn. The left panel shows the aperture field distribution for the two types of horn; the right panel shows the central portion of the resulting beam patterns, for horns with a 20-cm aperture diameter at a frequency of 30 GHz.

3.3.2 Design of the DASI Horn Lens and Shroud

For the DASI horn lens, we chose a meniscus lens with a refracting front surface, and non-refracting spherical rear surface to match the spherical wavefront at the aperture of the corrugated horn, as described in §3.2.4. In an interferometer, it is advantageous to have antennas with high aperture efficiency η_a. Antennas with high aperture efficiency enable the interferometer to more efficiently sample the u–v plane, increasing sensitivity, and enabling multiple fields to be more efficiently linked together to increase resolution in the u–v plane (White et al. 1999a). We therefore chose a meniscus lens in order to increase the aperture efficiency. The aperture efficiency of the DASI lensed horn is 84% at 30 GHz, compared to 69% for an unlensed zero flare-angle horn with the same aperture diameter. A plot of the aperture field distribution and corresponding far-field patterns for the two apertures are shown in Fig. 3.9.

High-density polyethylene (HDPE) was selected as the lens material because of its low loss tangent at cm wavelengths and machinability. Published optical constants at cm and mm wavelengths vary in the literature, with one source reporting an index of refraction $n_{\rm d} = 1.524$ and a loss tangent $\tan\delta = 660 \times 10^{-6}$ rad at 180 GHz (Birch et al. 1981), and another reporting $n_{\rm d} = 1.5218$ and $\tan\delta = 134 \times 10^{-6}$ rad at 35 GHz (Degenford & Coleman 1966). We measured $\tan\delta \approx 160 \times 10^{-6}$ rad in the range 22–40 GHz on sample material from the lens stock. We chose 4″ slab stock[2] to ensure uniformity, rather than rod stock, in which the dielectric constant can have radial variation (Plambeck 1999). The maximum thickness of the lens t is 6.200 cm; the lens therefore contributes a noise temperature of $T_{\rm N} \approx 2.2$ K at 30 GHz and a physical temperature of 230 K, the mean ambient temperature at the South Pole where the instrument is deployed. We used a slightly increased index of refraction in the lens design, $n_{\rm d} = 1.527$, taking into account the increase in HDPE density at polar ambient temperatures.

The lens is grooved with concentric rectangular cross-section grooves to act as a $\lambda/4$ anti-reflection coating. The design frequency of the anti-reflection coating is $f_{\rm ar} = 31$ GHz, in the center of the band. The groove parameters are (using the same nomenclature as for the corrugated waveguide) $s_{\rm ar} = 0.119$ cm, $p_{\rm ar} = 0.198$ cm, and $d_{\rm ar} = 0.196$ cm. Although the grooves are machined on a lathe and are parallel to the axis of rotation of the lens, the groove depth $d_{\rm ar}$ is the component of the depth normal to the surface of the lens, and is equal to $\lambda/4$ at the design frequency in a medium that has an index of refraction at the geometric mean of the dielectric and air, $n_{\rm ar} = \sqrt{n_{\rm d} n_{\rm air}}$. Table 3.1 summarizes the design parameters for the DASI lensed horn.

[2]Supplied by Accurate Plastics, Inc., 18 Morris Place, Yonkers, NY 10705.

Horn Section	Parameter Description	Parameter Symbol	Value
General	Low-frequency Limit	$f_L \left(= \frac{c}{\lambda_L} = \frac{ck_L}{2\pi} \right)$	26 GHz
	High-frequency Limit	$f_H \left(= \frac{c}{\lambda_H} = \frac{ck_H}{2\pi} \right)$	36 GHz
	Design Frequency	$f_0 \left(= \frac{c}{\lambda_0} = \frac{ck_0}{2\pi} \right)$	30 GHz
Flare	Aperture Diameter	D	20 cm
	Semi-flare Angle	θ_f	30°
	Pitch	p_f	0.195 cm
	Slot Width	s_f	0.130 cm
	Mean Slot Depth	$d_f \left(= b_n - \frac{(a_n - a_{n-1})}{2} \right)$	0.260 cm
Throat-flare Transition	Length	l_{tr}	1.154 cm
	Radius	R_{tr}	2.308 cm
	Number of Slots	$M - N$	6
	Pitch	p_{tr}	0.195 cm
	Slot Width	s_{tr}	0.130 cm
	Mean Slot Depth	$d_{tr} \left(= b_n - \frac{(a_n - a_{n-1})}{2} \right)$	0.260 cm
	Outer slot radius at output	b_M	1.072 cm
Throat	Length	l_{th}	3.605 cm
	Number of Slots	N	14
	Input Waveguide Radius	a_0	0.400 cm
	Initial Slot Pitch	p_1	0.320 cm
	Initial Slot Width	s_1	0.042 cm
	Initial Slot Depth	$d_1 \ (= b_1 - a_1)$	0.422 cm
	Initial Slot Outer Radius	b_1	0.824 cm
	Output Slot Pitch	p_N	p_f
	Output Slot Width	s_N	s_f
	Output Slot Depth	$d_N \ (= b_N - a_N)$	0.260 cm
	Output Slot Outer Radius	b_N	0.824 cm
Lens	Type		Simple Meniscus
	Dielectric Material		High-density Polyethylene
	Design Temperature	T_d	273 K
	Design Index of refraction (at T_d)	n_d	1.527
	Loss Tangent	$\tan\delta$	160×10^{-6} rad
	Axial Thickness	t	6.200 cm
	Aperture Efficiency	η_a	84%
	Antenna Gain	G	9.5×10^{-6} K/Jy
Anti-reflection Grooves	Design Frequency	f_{ar}	31 GHz
	Groove Pitch	p_{ar}	0.198 cm
	Groove Width	s_{ar}	0.119 cm
	Groove Depth	d_{ar}	0.196 cm

Table 3.1 DASI lensed corrugated horn parameters.

3.4 Measurement Results

3.4.1 Return Loss Measurements

The measured return loss for the DASI horn, shown in the left plot of Fig. 3.10, is < -24 dB across the 26–36 GHz band for the unlensed horn, and < -20 dB for the horn with lens and shroud in place. The typical return loss is < -30 dB and

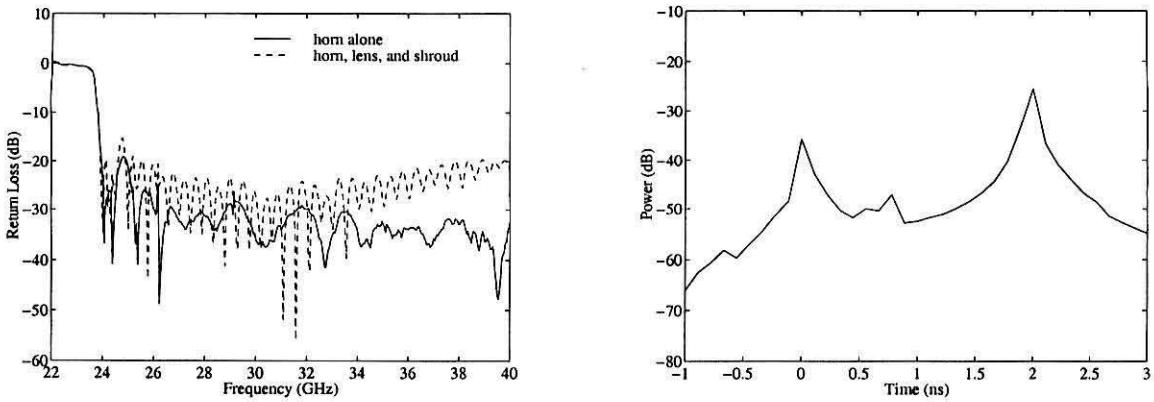

Figure 3.10 The measured return loss for the DASI lensed corrugated horn. The left plot shows the return loss vs. frequency for the horn without the lens or shroud in place (solid line) and with the lens and shroud (dashed line). The right plot shows the return loss for the lensed horn in the time domain. Peaks in the power at 0 ns, 0.8 ns, and 2.0 ns correspond to the input to the circular-to-rectangular waveguide transition, the input to the throat-flare transition, and the rear spherical surface of the lens, respectively.

< -25 dB for the unlensed and lensed horn, respectively. The return loss for the unlensed horn exhibits two resonant spikes at 26.2 GHz and 29.2 GHz. These are due to an RF choke and o-ring flange at the input to the horn, designed electrically to accommodate a Mylar vacuum window (with a dielectric constant $\epsilon_r = 3.0$). The spikes disappear when the vacuum window is in place. The return loss in the lensed horn is dominated by an impedance discontinuity at the lens, and reaches its minimum near the design frequency of the anti-reflection grooves, $f_{ar} = 31$ GHz.

Fourier transforming the return loss to the time domain can be used to discriminate between the contributions from the various regions of the lensed horn. To minimize confusion in the interpretation of the time domain data due to dispersion from frequencies near cutoff in the narrow region of the throat, we only Fourier transformed the return loss for frequencies well above cutoff, 31–40 GHz. The resulting time domain plot, on the right side of Fig. 3.10, reveals peaks in power at times of 0 ns, 0.8 ns, and 2.0 ns. When the group velocity delay due to the circular-to-rectangular

waveguide transition and narrow region of the throat is taken into account, these times correspond to round-trip distances to the input of the circular-to-rectangular waveguide transition, the input of the throat-flare transition, and the rear spherical surface of the lens, respectively. There is no apparent signature due to reflection from the initial slot in the throat. For comparison, the return loss was measured for a 9° semi-flare angle corrugated horn with conventional tapered slot throat geometry, as in Fig. 3.3a. In the time domain, the return loss was dominated by a peak corresponding to the position of the first $\lambda/2$ slot.

The time domain plot, as mentioned above, clearly shows that the amplitude oscillations of the lensed horn return loss in the frequency domain are due to reflections between the impedance discontinuities in the circular-to-rectangular waveguide transition and lens. When the response from the circular-to-rectangular waveguide transition is gated out, these oscillations in return loss are reduced, approaching the mean value between peaks. When the unlensed return loss data are gated in a similar manner, the return loss is reduced to < -35 dB from 31–40 GHz, indicating that the circular-to-rectangular waveguide transition dominates the return loss in the upper half of the band. We chose a commercially available circular-to-rectangular waveguide transition, 3.8 cm in length with an adiabatic taper; the return loss could be improved by changing the transition to incorporate a longer adiabatic taper or a multiple-stepped transition.

3.4.2 Beam Measurements

We measured beam patterns for both the unlensed corrugated horn and the horn with lens and shroud in place. Measurements for both configurations were done outside on a rooftop, sweeping the horn under test toward the zenith to minimize multipath signals. For the unlensed horn, we used a frequency synthesizer as a transmitter, and a spectrum analyzer as a receiver. The beam pattern was measured at 26 GHz, 30 GHz and 36 GHz in both the E- and H-planes. The measured and theoretical

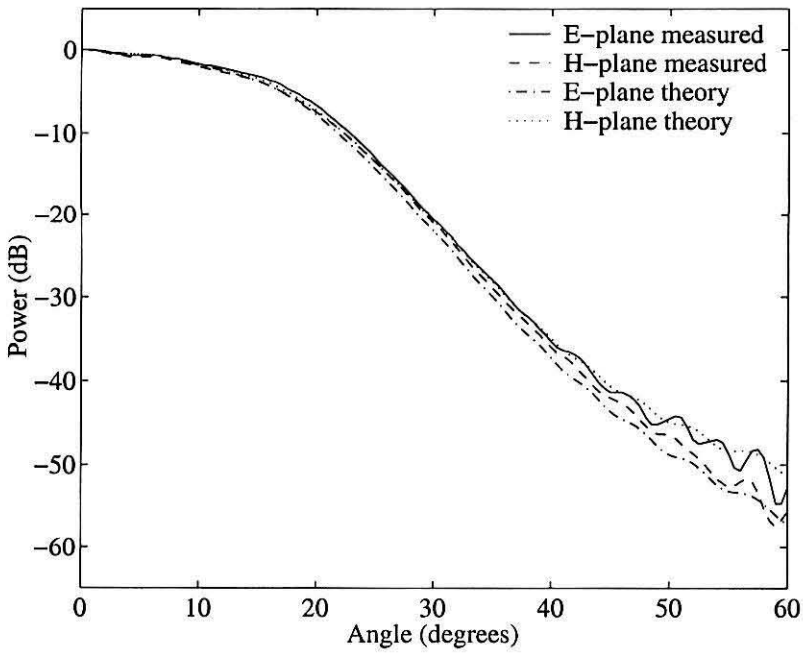

Figure 3.11 The measured and theoretical beam patterns for the DASI corrugated horn, without lens and shroud, at $f = 30$ GHz. The theoretical beam patterns were calculated using the Fourier transform method.

beam patterns at 30 GHz for the unlensed horn are shown in Fig. 3.11.

The theoretical beam pattern for the unlensed horn was calculated by taking the Fourier transform of the transverse component of the field in Eq. (3.1) over the flat aperture plane, taking into account the phase gradient and amplitude falloff as the radial distance to the horn apex increases toward the edge of the aperture. The theoretical E-plane beam pattern is modulated by an additional factor of $\cos^2(\theta_B)$ in power, where θ_B is the angle off of the optical axis, due to the vector nature of the fields (Collin 1985). The measured and theoretical beam patterns agree well out to $\theta_B \approx 50°$. There is little evidence for higher order modes, which would cause a deviation in the measured beam away from that predicted by theory.

The beam pattern of the lensed horn was measured using a frequency synthesizer as a transmitter, and a vector network analyzer as a tuned receiver. A splitter and

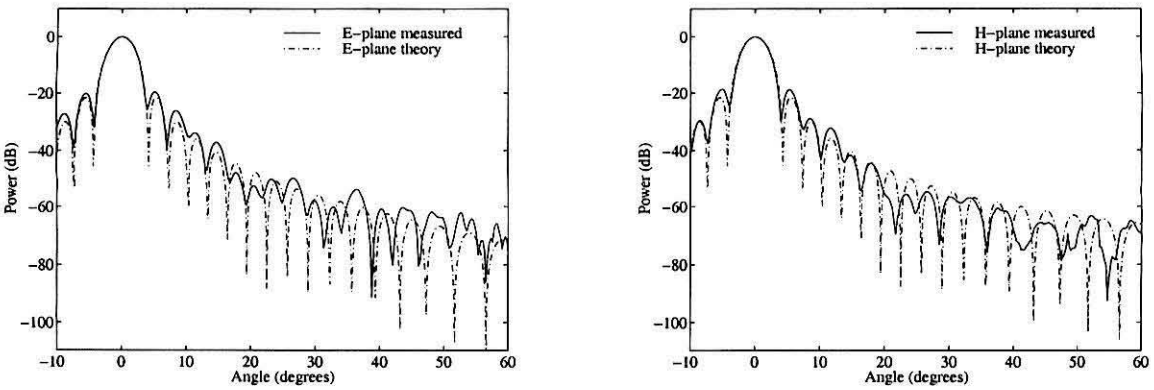

Figure 3.12 The measured and theoretical beam patterns for the DASI corrugated horn, with lens and shroud in place, at $f = 30$ GHz. The theoretical beam patterns were calculated using the Fourier transform method.

coaxial cable were used to route half of the transmitter signal to the second port of the network analyzer, so that both the amplitude and phase of the signal received by the horn could be measured at 801 points across the band. With this phase information, we gated the signal in the time domain, which reduced the response to multipath signals, and allowed us to probe deep into the sidelobe pattern.

The beam pattern of the lensed horn at 30 GHz, Figs. 3.12 & 3.13, demonstrates that the lensed corrugated horn behaves as predicted, with symmetric E- and H-plane beam patterns and evenly tapered sidelobes. The measured beam patterns generally agree with the predicted pattern, again calculated using the Fourier transform method. The first few sidelobes, shown clearly in Fig. 3.13, are a few dB higher than predicted across the band. This may be due to truncation of the beam by the shroud, by a breakdown of the J_0 approximation for the aperture distribution of the unlensed horn, or by a breakdown in the ray-tracing approximation for the power distribution near the edge of the lens. The lens surface contour and index of refraction are designed for a lower ambient temperature (273 K) than that at which the beam was measured. However, this should have only a small effect on the beam pattern.

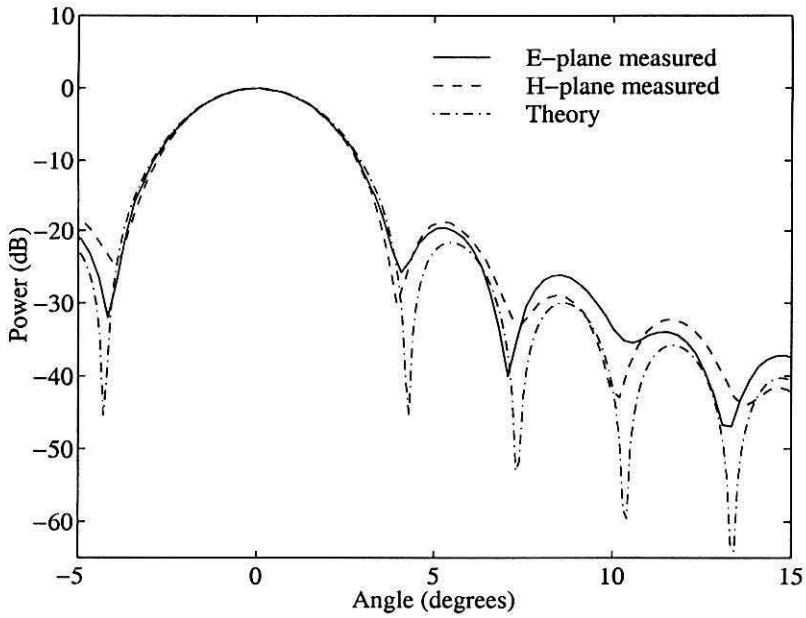

Figure 3.13 DASI lensed horn beam pattern at $f = 30$ GHz, enlarged to show the first few sidelobes. Only one theoretical beam pattern is shown, as E- and H-plane theoretical patterns are indistinguishable at small angles.

	Full width half power (FWHP)				First sidelobe peak response			
Freq.	E-plane measured	E-plane theory	H-plane measured	H-plane theory	E-plane measured	E-plane theory	H-plane measured	H-plane theory
26 GHz	4.1°	4.0°	3.7°	4.0°	-19.8 dB	-21.6 dB	-20.5 dB	-21.6 dB
30 GHz	3.4°	3.4°	3.4°	3.4°	-19.6 dB	-21.6 dB	-18.6 dB	-21.6 dB
36 GHz	2.8°	2.9°	2.8°	2.9°	-19.1 dB	-21.6 dB	-17.1 dB	-21.6 dB

Table 3.2 DASI lensed corrugated horn beam parameters.

The lensed horn behaves well throughout the 26–36 GHz band (Table 3.2), but with generally higher first sidelobes at the high end of the band, most likely due to mode imbalance away from the design frequency.

3.4.3 Coupling Measurements

In the DASI interferometer, the High Electron Mobility Transistor (HEMT) based amplifiers in each receiver emit correlated noise from the input and output ports which, when coupled to an adjacent antenna, produce a signal at the correlator output on the order of (at most) $\sqrt{|S_{21}|}T_{\rm cor}$ in units of antenna temperature, where $|S_{21}|$ is the amplitude ratio of the coupling between antennas and $T_{\rm cor}$ is the correlated noise component from the HEMT amplifiers (see detailed discussion in Padin et al. 2000). Given an expected CMB sky signal of $\sim 10^{-5}$ K (again in units of antenna temperature) and a noise temperature for the HEMT amplifiers $T_{\rm HEMT} \sim 10$ K, we conservatively require a coupling $\ll -120$ dB in order to make the coupling signal subdominant to the CMB sky signal.

We measured the coupling between adjacent coplanar antennas using a network analyzer and Ka-band amplifiers, gating the data in the time domain to remove coupling due to multipath signals in the room. The results were confirmed at a few discreet frequencies using a frequency synthesizer and detector outdoors with the horns pointed at the sky, increasing our confidence in the network analyzer measurement method. The time domain data and gate used for the measurements are shown in Fig. 3.14. The direct path coupling signal lies within the gate; the large peak outside the gate at 17 ns is a signal reflected from a wall of microwave absorber 170 cm in front of the apertures (which we verified by changing the distance to the absorber). The observed coupling signal occurs on longer time scales than expected from the ~ 100 cm path length of the combined horn lengths and separation distance between the centers of the apertures. This may be due to coupling between more dispersive higher order modes in the near-field geometry.

The coupling between adjacent horns shows complex structure in the frequency domain (Fig. 3.15). This has been previously observed in mutual coupling within circular waveguide arrays, and attributed to diffraction in the flange geometry (Bailey 1974). The peaks in the E- and H-plane coupling are at similar levels. The coupling

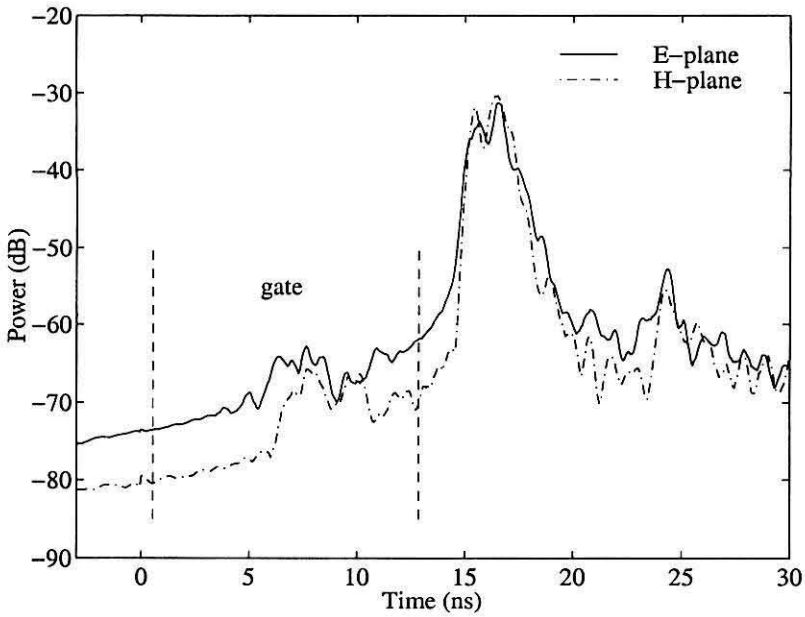

Figure 3.14 Time domain gate used for coupling measurements. The signal within the gate is direct path coupling between the horn apertures. The multipath signal at 17 ns is due to microwave absorber placed 170 cm in front of the apertures and is gated out. The coupling signals shown are for coplanar apertures, with parallel polarization, aligned in the E- and H-planes. The horn edge separation is zero; the aperture edge separation is 5.4 cm due to the width of the horn flanges. The time domain signals have been smoothed for clarity.

decreases monotonically with increased horn separation, decreasing by $\sim$ 20 dB in both the E- and H-planes from zero horn edge separation to a separation of 75 cm. With zero horn edge separation, the coupling peaks near -100 dB in both the E- and H-plane orientations. This does not take into account additional isolation provided by the decorrelation that the propagation delay will cause over the 1 GHz wide DASI correlation channel widths. The unwanted correlated noise between receivers could still dominate the desired CMB signal with -100 dB coupling between horns, we therefore placed cooled waveguide isolators in front of the HEMT amplifiers to further reduce the potential coupling of correlated noise power (see Chapter 4). Additionally, our observing strategy incorporates observations of multiple fields on the sky

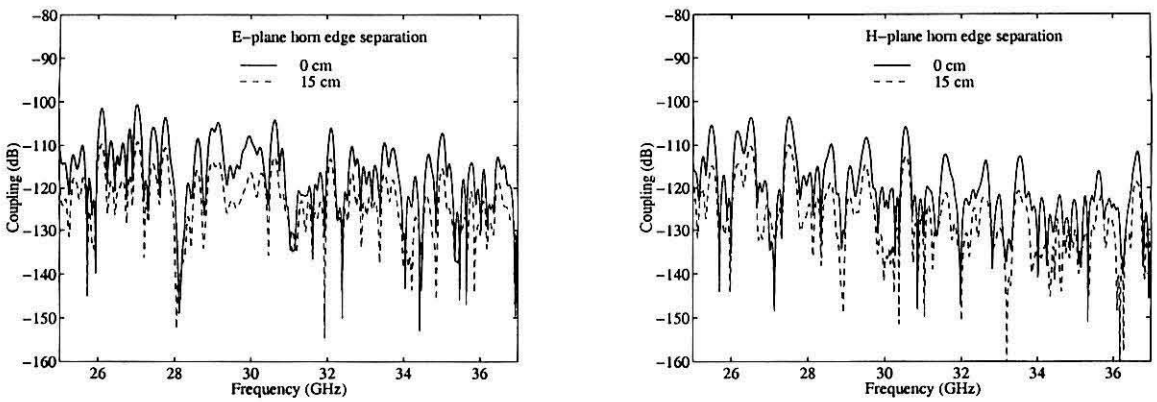

Figure 3.15 Measured coupling between adjacent horns, with aperture separation in the E-plane (left plot) and H-plane (right plot). The aperture edge separation is 5.4 cm greater than the horn edge separation due to the width of the horn flanges.

in the same instrument configuration; this allows us to remove contaminating signals, such as correlated noise due to coupling between antennas, during data analysis (see Chapters 5, 6, and 7).

3.5 Summary

We have designed a wide flare-angle lensed horn with low return loss as the antenna element for the DASI experiment. The combination of a wide flare-angle horn and low return loss, necessary for the DASI experiment, presents a design challenge. In our design, we have employed a narrow throat section with tapered-width slots, and a constant radius-of-curvature throat-flare transition to a 30° semi-flare angle at the output. The resulting return loss characteristics are excellent: we measured a return loss < -24 dB for the horn without lens across the 26–36 GHz band, and < -20 dB with the lens in place, with typical values < -30 dB and < -25 dB for the unlensed and lensed horn, respectively. Unlike horns with fixed-width slots in the throat, the DASI horn return loss is not dominated by reflections from the first slot in the

throat. Likewise, the far-field beam pattern is well behaved, little evidence of higher order mode contamination in the band. We found that the assumption of a simple $J_0(\alpha_{01}\theta/\theta_f)$ aperture distribution and the Fourier transform method for calculating the far-field were adequate to accurately model the beam patterns of both the lensed and unlensed horns. The mutual coupling between adjacent coplanar horns was measured to be < -100 dB across the band. Although small, fluctuations in the CMB are smaller yet, prompting us to insert waveguide isolators in front of the HEMT amplifiers to reduce potential coupling of correlated HEMT noise between adjacent horns.

Chapter 4

Receivers

4.1 Introduction

The receivers are the so-called *front end* of the interferometer. Their job is to collect the signal via the antenna, amplify the signal, and downconvert it to a lower frequency which can be transmitted with less loss and subsequently processed in the *back end* with commercially available components. The receiver is the first component in the signal chain, and is the source of almost all of the system noise — careful receiver design is therefore critical in an instrument capable of achieving the sensitivity required to measure anisotropy in the CMB. To this end, the Ka-band operating frequency (26–36 GHz) was chosen because of the availability of low-noise High Electron Mobility Transistor (HEMT) amplifiers (Pospieszalski 1993; Pospieszalski et al. 1994), as well as low atmospheric emissivity and the expected low level of Galactic foreground emission at these frequencies. Prototype receivers were built and tested at the University of Chicago during the period 1996–1998, with production assembly commencing during 1999 and finished at the South Pole in January 2000.

4.2 RF Design

The DASI receivers consist of a 20-cm aperture-diameter lensed corrugated horn (described in Chapter 3), coupled to a cooled low-noise HEMT amplifier in Ka-band

(see schematic, Fig. 4.1, and layout, Fig. 4.2). A 38 GHz local oscillator (LO) is used to downconvert the signal to a 2–12 GHz intermediate frequency (IF); the lower sideband is selected with a low-pass filter in front of the mixer. The IF signal is further amplified by a cooled IF amplifier prior to exiting the dewar. Attenuators are inserted at the output of the HEMT amplifier and the mixer to improve the impedance match between the amplifiers and other components to prevent oscillations, and to prevent gain compression in the IF amplifier. We employ a quarter-wave dielectric fin in circular waveguide to make the receivers sensitive to circular polarization, which reduces sensitivity to linearly polarized foregrounds such as Galactic synchrotron emission[1]. We periodically inject a correlated broadband noise source to calibrate the correlator output (see §5.3) via a 30 dB waveguide coupler in front of the HEMT amplifier. Also, as discussed in §3.4.3, we have installed a waveguide isolator in front of the HEMT to reduce the amount of correlated noise from the HEMT input that may be coupled through the antenna to adjacent receivers, which would produce an undesired correlated signal. Photos of the receiver assembly are shown in Fig. 4.3.

Many of the components in the receiver are available as stock or custom built items from microwave component suppliers, but some must be designed and/or built in-house. The antennas, described in Chapter 3, and the thermal break, for example, were designed by the author; HEMT amplifiers were built in-house by J. Kovac from an NRAO design (Pospieszalski 1993; Pospieszalski et al. 1994). The gain and noise temperature curves for one of the DASI HEMT amplifiers is shown in Fig. 4.4. Suppliers and specifications of other components are given in Table 4.1.

The design of the DASI instrument was largely driven by the technological feasibility of attaining excellent receiver noise performance, with noise temperatures of ~ 30 K. The noise temperature of a device is defined as the temperature of a blackbody (or matched resistor) which, when inserted at the input of the device, would

[1]During the austral summer 2000-2001 we incorporated a rotating achromatic $\lambda/4$ retarder, which enables us to switch between left- and right-handed circular polarization states, useful for polarization observations.

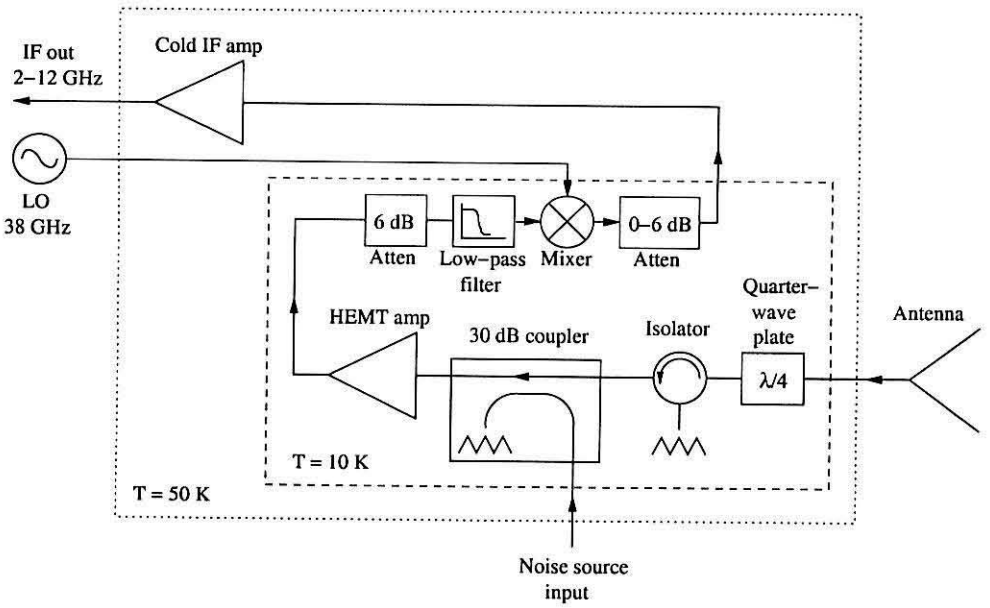

Figure 4.1 DASI receiver schematic diagram.

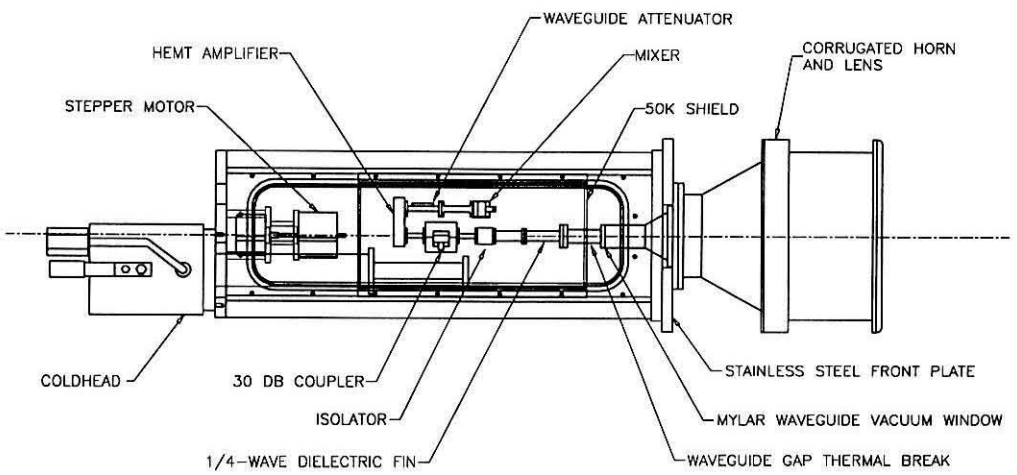

Figure 4.2 DASI receiver physical layout. The dewar is attached to the telescope via the stainless steel front plate. The stepper motor, shown on left, was not used during the first season but is currently being used to manipulate rotating polarizers.

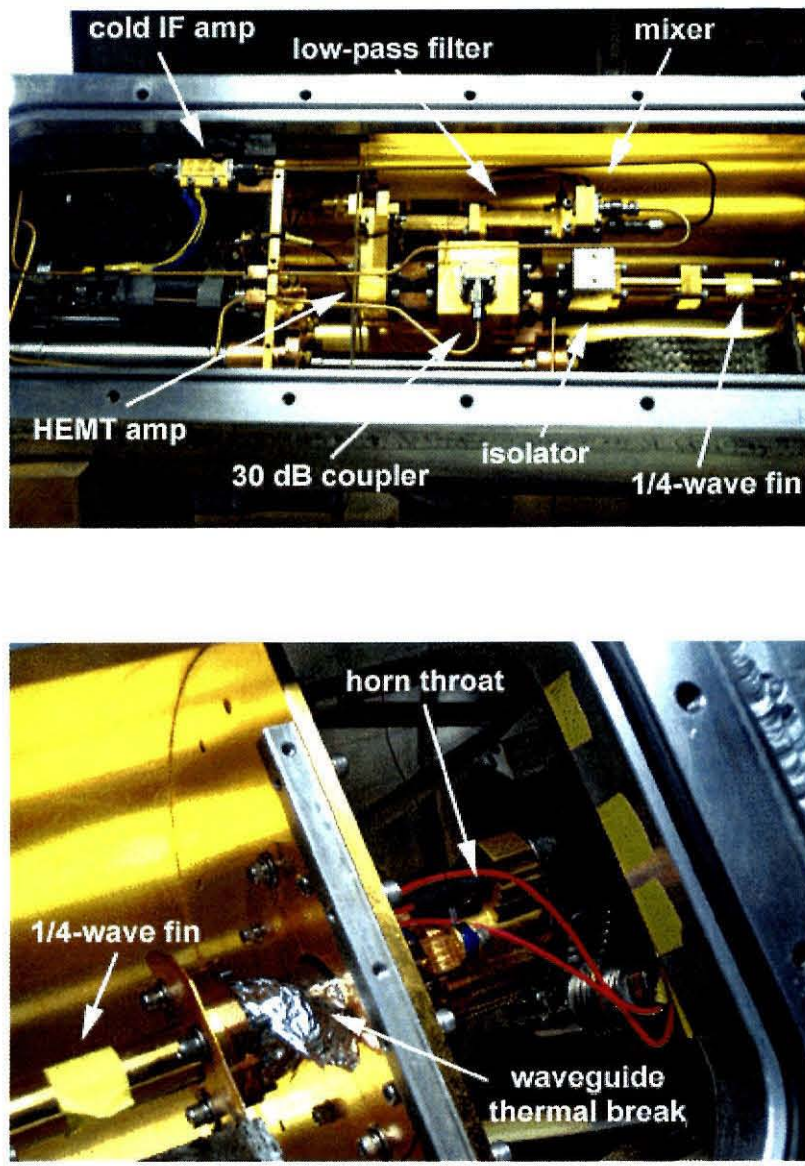

Figure 4.3 Side view of the open DASI receiver, showing the various RF components in the signal chain. In the top photo, the horn antenna (not shown) is to the right. The receiver output is at left. The lower photo shows an interior detail, including the output of the horn throat, waveguide thermal break covered in reflective mylar (superinsulation), and the $\lambda/4$ dielectric fin waveguide section.

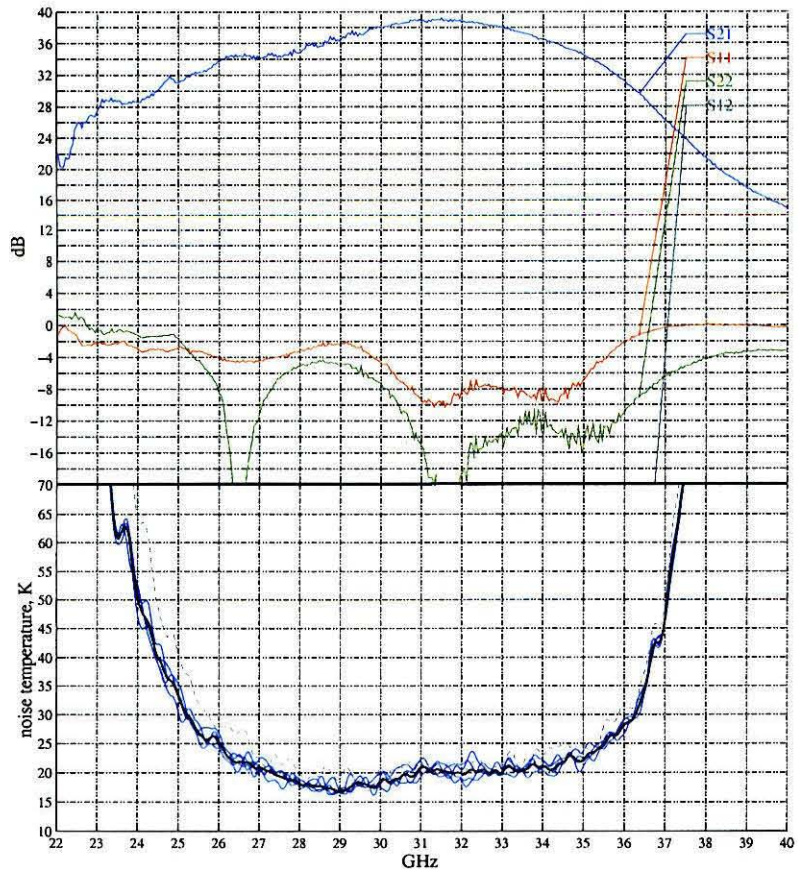

Figure 4.4 HEMT amplifier gain and noise temperature curves for one of the DASI amplifiers (Ka36) built at the University of Chicago. The top panel shows the forward gain (S21), the reflection loss at the input (S11) and output (S22) ports, and the reverse gain (S12, off chart). The lower panel shows the noise temperature performance (multiple curves are repeated measurements). The noise temperature curve has an undetermined overall vertical offset.

double the noise power seen at the output. It is the standard way to express noise performance in radio astronomy, where the observing frequencies are in the Rayleigh-Jeans limit of the calibrator load Planck spectrum, so that output power is linearly related to the temperature of the load

$$P \propto T_n + T_{\rm load}, \tag{4.1}$$

where T_n is the noise temperature of the device and $T_{\rm load}$ is the load temperature.

Component	Supplier	Model #	Spec.
Isolator	Channel Microwave Corp. Camarillo, CA 93012	IR627	Ret. Loss 15.9 dB min Ins. Loss 0.8 dB max Isolation 16 dB min
30 dB Coupler	Millitech, LLC Northampton, MA 01060	CGC-28-SL3 NO	Coupling 30.0 dB Flatness ± 1.5 dB Ins. Loss 0.5 dB Directivity 17.0 dB Input Ret. Loss 23 dB Output Ret. Loss 21 dB
W/G attenuator	Custom Microwave, Inc. Longmont, CO 80501	LA28S	Adjustable atten. (6 dB nominal)
Low-pass w/g filter	Spacek Labs, Inc. Santa Barbara, CA 93101	LPF27-38	Ins. Loss 0.5-0.8 dB, $f < 36$ GHz Rejection > 28 dB, $f = 38$ GHz Rejection > 40 dB, $f > 40$ GHz
Mixer	Spacek	KaKa-9	IF 2–12 GHz LO 38 GHz, +3 dBm Conv. Loss 5.5–5.8 dB, $f = 26$–36 GHz
38 GHz Gunn osc.	Spacek	GKa-380-1	Output power 110 mW, $f = 38$ GHz
Cold IF amplifier	Miteq, Inc. Hauppauge, NY 11788	AMF-4D-0210120- 50K-CRYO	Freq. 2–12 GHz Gain 30.0 dB min Flatness ± 2.0 dB max $P_{\rm out}$ @ 1dB comp. 0 dBm min Input Ret. Loss 9.6 dB max Output Ret. Loss 9.6 dB max Noise Temp. 50 K max @ 77 K

Table 4.1 DASI receiver component specifications.

Given receiver components with noise temperatures T_{ni}, the noise temperature of the receiver is given by

$$T_{\rm rx} = T_{n1} + \frac{T_{n2}}{G_1} + \frac{T_{n3}}{G_1 G_2} + \ldots, \tag{4.2}$$

where T_{ni} is the noise temperature of component i, referenced to its input, G_i is the component gain, and the ordering of the components starts with the first component in the RF chain. If the receiver noise temperature $T_{\rm rx}$ is being calculated, the first component is usually the feed horn, which for DASI is the complete antenna; if the total system noise temperature $T_{\rm sys}$ is being calculated, the first component is the atmosphere. The noise temperature of passive lossy components such as the atmosphere or waveguide is given by

$$T_n = \frac{(1-G)T_{\rm phys}}{G}, \tag{4.3}$$

where $T_{\rm phys}$ is the physical temperature of the component, $(1-G)$ is its emissivity, and $(1-G)T_{\rm phys}$ is the apparent temperature at the output, which must be divided by

the gain G to refer the temperature to the equivalent temperature at the input, T_n. To achieve low noise temperatures, the most crucial components are the first stage amplifier and the components which precede it in the RF chain. All components which follow the first stage amplifier make lesser contributions, mitigated by the first-stage amplifier gain. In the receiver design, we therefore minimize the amount of warm waveguide preceding the HEMT, ensure that the dielectric used in the quarter-wave fin has low-loss, and ensure that the isolator and noise source waveguide coupler have low insertion loss (i.e., gains near unity).

To test the noise temperature of the receiver, the noise temperature of the device is measured by placing both a hot load (usually at ambient temperature $T_h \simeq 300$ K) and a cold load (usually at liquid Nitrogen temperature $T_c = 77$ K) in front of the receiver and measuring the power ratio $y = P_h/P_c$. The noise temperature of the receiver is then given by

$$T_{\rm rx} = \frac{(T_h - T_c)}{(y-1)} - T_c. \tag{4.4}$$

Receiver noise performance, both expected and realized, is discussed in §4.4.

4.3 Cryogenic Design

The first-stage HEMT amplifier and all waveguide RF components are cooled to ~ 10 K by a two-stage Gifford-McMahon cycle DE-202N Helium refrigerator, manufactured by IGC-APD Cryogenics[2]. The motion of the displacer assembly is governed by gas pressure, and rare-earth materials in the second-stage displacer enable a no-load second stage temperature of 6 K, with a no-load first-stage temperature around 35 K. For our expected first and second stage loads of 2.1 W and 0.35 W, respectively, the DE-202N has a performance specification of 43 K for the first stage and 7.5 K for the second stage. In practice, we achieve somewhat higher temperatures, 50–70 K for the first stage (measured at the IF amplifier) and 9–15 K for the second

[2]IGC-APD Cryogenics Inc., 1833 Vultee St., Allentown, PA 18103-4783.

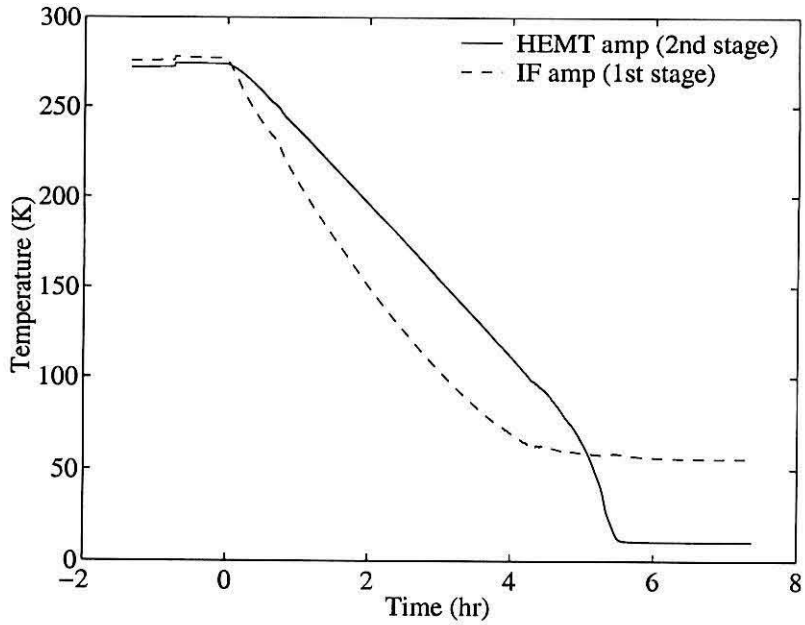

Figure 4.5 Receiver cool down performance for the HEMT amplifier (solid line), which is thermally connected to the second stage, and for the IF amplifier (dashed line), which is thermally connected to the first stage.

stage (measured at the HEMT amplifier). While some of this discrepancy may be due to higher than expected thermal loading, the significant variability in the first-stage temperatures between receivers may indicate deviations in the coldhead performance from that given in the specification sheets. Typical cooldown time for the receivers is 6 hr (see Fig. 4.5).

In the DASI dewar cryogenic design, a gold plated radiation shield thermally connected to the first stage takes the ambient temperature radiative load, and is also used to heat-sink the coaxial cables which run from the rear wall of the dewar to the RF components. The radiation shield is supported from the front plate of the cylindrical dewar by 1/4″ O.D. × 1/32″ wall G-10 support struts. The G-10 struts are epoxied using Stycast 2850FT[3] to angled aluminum blocks which screw into the radiation shield and front plate of the dewar. The structure proved to be both rigid

[3]Manufactured by Emerson & Cuming, Inc., 869 Washington Street, Canton, MA 02021.

and durable.

Unscrewing the front plate from the dewar allows the radiation shield and RF components to be removed in a modular fashion. Electrical connections to the active RF components are made with 32 gauge phosphor bronze wiring[4] to minimize the thermal load. An interior connector bulkhead near the dewar output was used as a convenient break point. The phosphor bronze wiring was mechanically stripped, and soldered to Micro-D[5] connectors. The solder connections were potted in Stycast 2850FT, using embedded heat-shrink tubing for strain relief. This wiring technique proved to be extremely reliable (only one wire has failed in 14 dewars). Short jumper wires bridged the connector bulkhead to the hermetic military-style circular connectors[6] on the rear dewar wall. The RF and IF signals are transmitted in 0.085″ O.D. semi-rigid Be Cu coaxial cable[7] to minimize the thermal load on the first and second stages. Thermal isolation between the horn and cold waveguide components is accomplished with a section of circular waveguide re-entrant in a cylinder of G-10 tubing with a small 0.005″ gap (see Fig. 4.6). A listing of the thermal budget for the DASI dewars is given in Table 4.2.

The waveguide vacuum seal was implemented with a 0.0005″ Mylar film membrane at the termination of the horn throat, with an RF choke and o-ring seal (Fig. 4.7). The three o-rings at the front of the dewar (the throat vacuum seal, and two on the dewar front plate) are designed to operate at polar ambient temperatures. The o-ring grooves are designed with a 30% squeeze, higher than usual in order to maintain seal at polar temperatures. For the o-ring material, we tested sample o-rings made with various low-temperature silicone compounds provided to us by Precision Associates[8] and found their silicone compound # 19701 to be superior to other compounds (including other silicone compounds) for low-temperature performance. This compound

[4]Available from Lake Shore Cryotronics, Inc., 575 McCorkle Blvd., Westerville, OH 43082.
[5]Manufactured by ITT-Cannon, 666 E. Dyer Road Santa Ana, CA 92705.
[6]Supplied by Detoronics Corp., 10660 East Rush St., So. El Monte, CA 91773.
[7]Manufactured by Precision Tube Co., Coaxitube Division, 620 Naylor Mill Road, Salisbury, MD 21801.
[8]Precision Associates, Inc., 740 N. Washington Ave., Minneapolis, MN 55401.

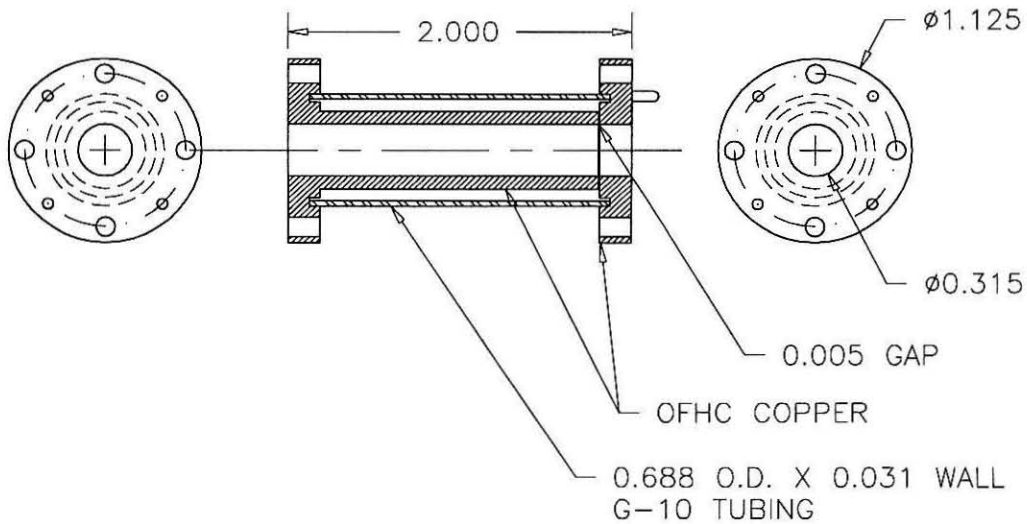

Figure 4.6 Cross section of the DASI receiver waveguide thermal break. The waveguide thermal break consists of a section of cold circular re-entrant waveguide with a G-10 stand-off. A 0.005″ waveguide gap at the throat end provides the thermal isolation. Dimensions are in inches.

First Stage			
Part	Qty	Specifications	Thermal Load (W)
Radiation shield	1	$A \sim 1360$ cm^2, $\epsilon = 0.01$	0.62
G-10 shield standoffs	8	$A = 0.14$ cm^2, $l = 4.1$ cm	0.14
Be Cu coax	3	$A = 0.018$ cm^2, $l = 14$ cm	0.76
Phosphor bronze wires	18	$A = 3.2 \times 10^{-4}$ cm^2, $l = 20$ cm	0.02
IF amp (Miteq)	1	130 mA @ 4.3 V	0.56
		Total first stage load:	2.1
		Second Stage	
Radiation		$A \sim 600$ cm^2, $\epsilon \sim 0.1$	0.00
G-10 web HEMT standoff	1	$A/l \approx 0.08cm$	0.01
Phosphor bronze wires	16	$A = 3.2 \times 10^{-4}$ cm^2, $l = 20$ cm	0.02
Be Cu coax	3	$A = 0.018$ cm^2, $l = 10$ cm	0.11
Mixer (Spacek)	1	2.5 V, 20 mA	0.05
HEMT amp	1	4 stages × 10 mA @ 1.2 V	0.05
HEMT amp LED's	1	6 mA @ 7.8 V	0.05
G-10 waveguide thermal break	1	$A = 0.41$ cm^2, $l = 4.1$ cm	0.06
		Total second stage load:	0.35

Table 4.2 DASI receiver thermal load budget. Assumes ambient, first stage, and second stage temperatures of 300 K, 50 K, and 10 K, respectively.

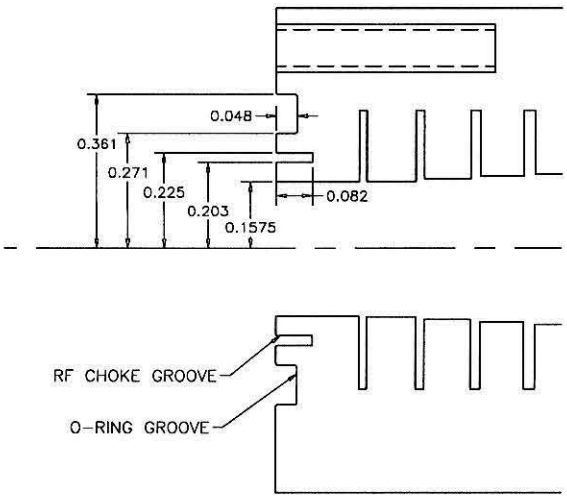

Figure 4.7 Detail of the horn throat, showing the o-ring seal and RF choke. The RF choke is designed to have $\lambda/4$ electrical length both radially, from the waveguide wall to the choke groove, and longitudinally along the depth of the choke groove, to present an electrical short at the waveguide wall. The radial length takes into account the relative dielectric constant of the Mylar vacuum window, $\epsilon_r = 3$. Dimensions are in inches.

maintained elasticity and vacuum at dry ice temperature (195 K). Although silicone is He permeable, we found that this did not affect our ability to leak check the dewars with judicious use of He and a He leak checker (the Mylar vacuum window is much more permeable than the silicone o-rings). As an additional precaution against o-ring failure, we installed a resistive heater on the horn throat near the vacuum window o-ring seal (see Fig. 4.3), since this interface, between the ambient temperature horn and the 10 K cold RF waveguide, was expected to be the coldest and most vulnerable vacuum seal. The actual throat temperatures ranged from 240–260 K during the austral winter, and the throat heaters proved unnecessary. The front plate of the dewar is made with 304 stainless steel, and is pocketed on the interior side to increase thermal isolation between the horn (which is outside at ambient temperature) and the dewar exterior, on the inside of the telescope cabin, in order to prevent ice buildup on the dewar exteriors and prevent excessive heat loss from the telescope cabin.

4.4 Performance

During initial receiver tests, noise temperature performance was significantly worse than expected; the problem was eventually traced to gain compression in the cold IF amplifier. In one test, the bolometric IF output power of the receiver was measured to be 300 μW (-5 dBm), The cold IF amplifier output power at 1 dB compression was specified at 0 dBm minimum, and was measured on one of the amplifiers to be +5 dBm. However, to affect the noise temperature measurement by < 1 K, the output power must be below the 0.03 dB compression level, which for the measured amplifier occurred at an output power of -10 dBm.

The gain compression problem was remedied by inserting an SMA attenuator at the output of the mixer. In production assembly, IF amplifier gain compression was tested by measuring receiver noise temperature at normal HEMT amplifier bias settings, and with the fourth stage voltage reduced, which reduces the HEMT amplifier gain without significantly affecting the noise performance. Attenuators with values of 3–6 dB were inserted at the mixer output if a problem was detected.

A number of tests were performed with various receiver configurations in order to determine the contributions of various components to the overall receiver noise temperature; these are tabulated in Table 4.3. The receiver noise temperatures are somewhat higher than we anticipated. This was due to a combination of factors, most notably, the noise temperature due to the warm throat, thermal break, and cold waveguide were higher than expected; there was also significant variability in the HEMT amplifier performance, and higher noise temperatures near the lower and upper edges of the 26–36 GHz band. A plot of the receiver temperatures, as measured with thermal loads during calibration at the South Pole, is shown in Fig. 4.8.

The only nagging design flaw in the receivers was the semi-rigid IF coax which connects the cold IF amplifier to the feedthrough on the rear dewar bulkhead. Although this coax section has a 90° dogleg bend to accommodate strain relief, the solder joint on the cable connector near the feedthrough mechanically failed on multiple receivers

Component	Expected T_n (K)	Actual T_n (K)
Lens	3	3
Warm throat, thermal break, cold w/g	3	4–5
Front-end isolator	2	2
Directional coupler	0.01	
HEMT amplifier	10–15	10–30 K (across band)
Mixer	0.03	
Cold IF amplifier	0.2	
Total:	16–21	20–40

Table 4.3 Expected and actual noise temperature contributions of various receiver components.

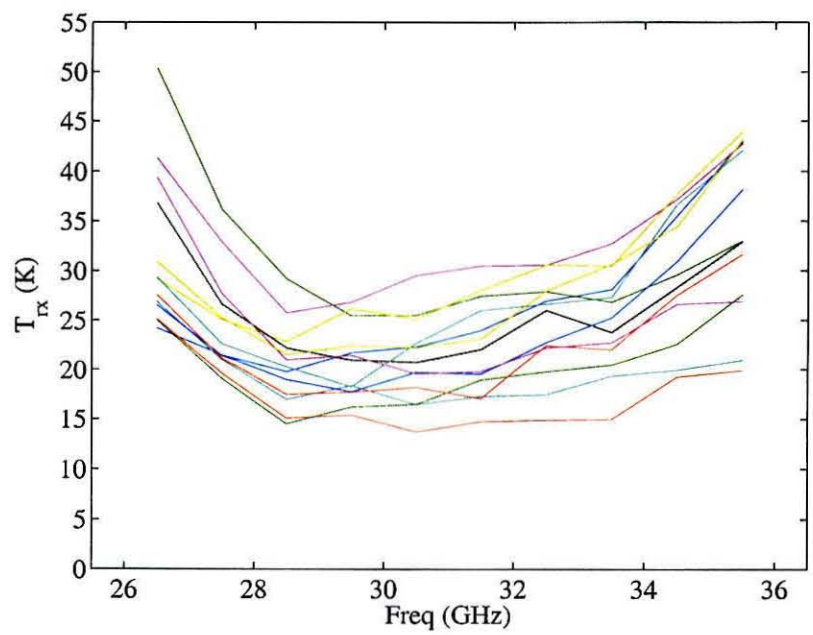

Figure 4.8 DASI receiver noise temperatures measured during calibration, February 2001. The noise temperatures include the corrugated horn and lens.

when cold. The reasons for this may be a thermal length change between the IF amplifier, connected via the radiation shield to the front of the dewar, and the rear dewar bulkhead, or abuse during assembly in the tight space underneath the top o-ring flange of the dewar. The broken solder joints were repaired with a copper braid reinforcement.[9]

Occasionally during the observing season, a receiver would slowly warm; the problem was usually fixed by briefly disconnecting the coldhead valve motor, and allowing the dewar to warm slightly before reconnecting. The likely culprit was contaminants in the He lines which froze in the coldhead, impeding performance. Rarely would the vacuum in a dewar go soft; we found no need to install activated charcoal in the dewars to keep them cold for extended periods of time (Fig. 4.9). After an initial shakedown period, the receivers proved to be very reliable performers, which allowed extended uninterrupted observations.

[9]During the austral summer 2000-2001 the IF amplifier semi-rigid coaxial cables were replaced with cables which incorporated a 360° loop to increase cable flexibility.

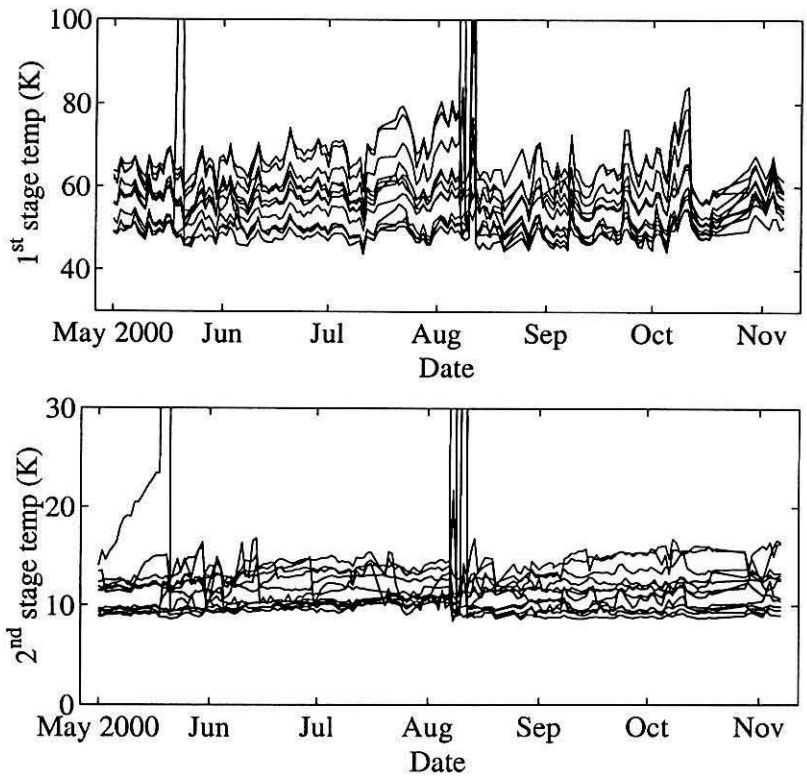

Figure 4.9 DASI receiver physical temperatures throughout the first season of observing. The receivers stayed cold for extended periods of time, mostly without trouble. The abrupt spike in temperatures in mid-August was due to a power outage.

Chapter 5

Observations

5.1 Observing Strategy

The science goal for the initial season was to measure the CMB angular power spectrum in the range $100 < l < 900$ as accurately as possible, and to make high signal-to-noise images of the CMB. To this end, we observed widely separated fields on the sky, both to minimize sample variance through increasing the number of independent sky samples, and to facilitate rapid data analysis by minimizing interfield correlations. CMB fields were observed over the period 05 May–07 November 2000, during which we accumulated 97 days of observations. Observations were never prevented due to weather, and only 5% of data were lost due to weather based edits (see §5.4), confirming previous assessments of the exceptional quality of the site (Lay & Halverson 2000; Chamberlin et al. 1997).

Due to the lack of ground shields in the initial season (now installed), the instrument was susceptible to ground emission, particularly on baselines with a (u, v) radius < 40 ($l \lesssim 250$). Ground signal amplitudes are as much as tens of Jy on the shortest baselines, but show little temporal variability on time scales of many days. One advantage of observing near the South Pole is that sources track at a constant elevation, which helps to reduce azimuthal variability in the ground signal as the source is tracked. To mitigate the ground signal, we sequentially observed a series of 8 fields at constant elevation, separated by 1^{h} in right ascension (RA), over the same

Row	RA (J2000)	Dec (J2000)	Dates Observed	Days Observed
A	22 00 00	−61 00 00	04 May 2000–29 May 2000	14
B	21 30 00	−67 00 00	13 Jun 2000–16 Jul 2000	24
C	22 30 00	−55 00 00	19 Jul 2000–16 Sep 2000	28
D	23 00 00	−49 00 00	12 Sep 2000–08 Nov 2000	31

Table 5.1 DASI CMB field row coordinates and dates observed. Field positions are obtained by adding 0–7^h to the RA listed for each row.

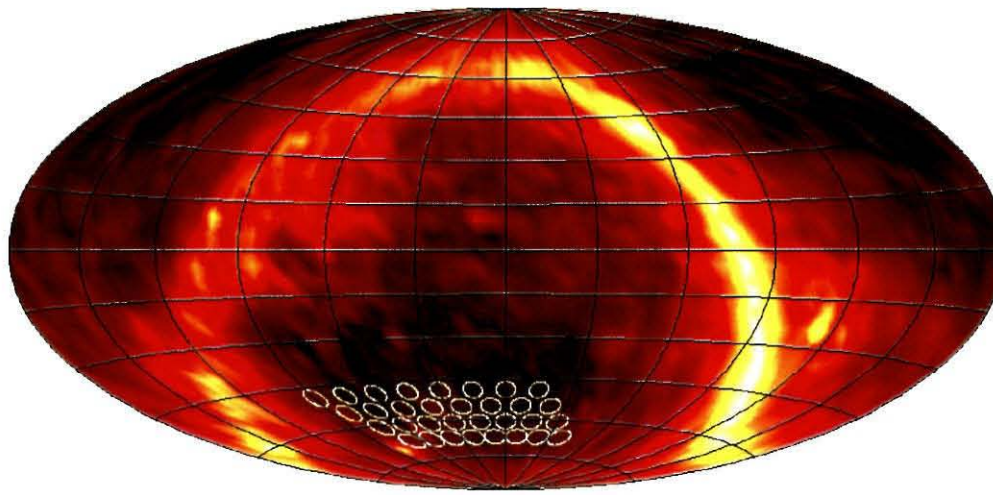

Figure 5.1 Locations of the DASI CMB fields, plotted over the IRAS 100 μm map, in equatorial coordinates. The color map is logarithmic, spanning 4 decades of intensity.

range in azimuth, allowing us to reject a ground contribution common to the 8 fields in the analysis. Observations were divided among 4 constant declination (elevation) rows of 8 fields, on a regular hexagonal grid spaced by 1^h in RA, and 6° in declination. The fields were selected to avoid the Galactic plane and to coincide with the area of lowest emission in the IRAS 100 μm map of the southern sky (Fig. 5.1). The elevation of the rows are $61°, 67°, 55°, 49°$, which we label the A, B, C and D rows for the order in which they were observed (see Table 5.1 for coordinates and dates observed). The field separation of 1^h in RA represents a compromise between immunity to time variability of the ground signal and a desire to minimize interfield correlations.

A given field row was observed daily over two azimuth ranges, for a total of 16

hours per day, with the remainder of the time divided among various calibration and pointing tasks (see §5.2 and §5.3). Phase and amplitude calibration were accomplished through daily observations of bright Galactic sources, permitting determination of the calibrator flux on all baselines to better than 2%. For the A row, the Carina nebula was used for amplitude calibration, and Centaurus A was used for phase calibration. For the B, C, and D rows, PKS J0859-4731, a bright compact HII region nearly point-like at the angular resolution of DASI, was used as both an amplitude and phase calibrator. Both the Carina nebula and PKS J0859-4731 were initially calibrated using thermal loads, as discussed in §5.3. The number of days for which each of the four rows was observed is 14, 24, 28 and 31 for the A, B, C and D rows, respectively, for a total integration time of 28–62 hr per field.

5.2 Pointing

A pointing model for the DASI telescope was developed using images from a 5-inch Schmidt-Cassegrain optical telescope and video camera assembly. Bright stars, detectable year-round, were used to determine values for an 8-parameter pointing model; rms residual offset positions for a set of 80 stars were $\sim 25''$ after the pointing model was applied. The offset between the deck rotation and optical axes of the telescope was determined by a series of star images taken while rotating the deck axis; this offset was included in the radio pointing model. The radio pointing axis was checked by measuring phase variations while rotating the deck axis during observations of PKS J0859-473138; phase offsets were negligible, confirming the pointing model.

One unique aspect of an interferometer is that the pointing (i.e., the center of the reconstructed image) is determined by the phase calibration, not the direction that the antennas are pointed on the sky. The relative pointing error between the celestial phase calibrator and the observed field determines the pointing error. Also, an error in the known position of the celestial phase calibrator will translate into a pointing error. As an additional check of the radio absolute pointing error, we

calculated offsets between DASI detected point source positions and PMN southern catalog coordinates (Wright et al. 1994). The calculated offset was generally less than $2'$, with a drift $\ll 1'$ over the period during which each row was observed. This offset is larger than our pointing error as determined by optical measurements; the discrepancy may be due to point source positional fitting uncertainty or an error in the known position of our celestial phase calibrators. While a constant absolute pointing error does not affect the CMB power spectrum data analysis for widely separated fields, the removal of point sources with positions derived from external information is affected; we therefore applied a derived overall offset for each field row to those PMN point source positions which we constrain in the data (see §7.2.4).

5.3 Calibration

The daily calibration tasks consisted of observations of celestial calibrator sources described in §5.1, and calibration of the relative amplitude of the real and imaginary correlator multiplier outputs. The latter was accomplished by injecting broadband correlated noise into the receivers while modulating the local oscillator (LO) quadrature phases by 90° in turn for each receiver. These data were obtained daily to calibrate the visibility data. Absolute calibration of the celestial amplitude calibrator sources, which we performed twice, was achieved through measurements of thermal loads, as described below.

5.3.1 Absolute Calibration

Absolute calibration sources such as planets and the CMB dipole, which are frequently used in CMB experiments, cannot be used directly by the DASI telescope; the planets are always close to the horizon with signal contaminated by ground emission, and DASI is not sensitive to the large angular scale CMB dipole moment. Initial absolute amplitude calibration was performed by using ambient and liquid Nitrogen thermal

loads placed in front of the antenna apertures to calibrate an internal correlated noise source. The noise source calibration was then immediately transferred to a bright celestial source. This absolute calibration procedure was done twice, in February 2000 and again in February 2001. In the first instance, the calibration was transferred to the Carina nebula. At the termination of the A-row observations in late May, we decided to use PKS J0859-4731 as both an amplitude and phase calibration source since it was more compact and a stronger source on long baselines.[1] We transferred our absolute calibration from the Carina nebula to PKS J0859-4731 through a series of interleaved observations of both sources. In the February 2001 procedure, the noise source calibration was transferred directly to PKS J0859-4731 (a bright, compact HII region). The overall flux scales resulting from the two independent absolute calibrations are found to agree to 0.3%, consistent with our estimate of $\sim 1\%$ overall statistical uncertainty in the measurement and transfer procedure. The systematic uncertainty in determining the thermal load effective temperature is 3%, which is the dominant contribution to the uncertainty in our overall flux scale. This uncertainty was determined through consideration of the specifications and measured error of the DT-470[2] temperature diodes, comparison of measured ambient load temperatures to weather station ambient temperature readings, and specifications of the Eccosorb[3] loads. The 1-σ flux scale calibration uncertainty, expressed as a percentage of $l(l+1)C_l/2\pi$, is 7% (3.5% in $\Delta T/T$) and is constant across all power spectrum bands.

Band power estimates are also affected, though weakly, by errors in the estimated aperture efficiency, on which our uncertainty is 4%. This uncertainty was estimated from discrepancies between the measured and theoretical beam-widths described in §3.4.2. As noted in §6.4.3, the rms sensitivity of any visibility to CMB fluctuations scales as the square-root of the effective aperture area $\sqrt{A_{\rm eff}}$, regardless of the baseline length. Thus an error in the estimated aperture efficiency affects the power spectrum

[1] At 30 GHz, the Carina nebula has visibility amplitudes ranging from 550 Jy on short baselines to 50 Jy on long baselines, as compared to 250 and 100 Jy, respectively, for PKS J0859-4731.

[2] Manufactured by Lake Shore Cryotronics, Inc., 575 McCorkle Blvd., Westerville, OH 43082.

[3] Manufactured by Emerson & Cuming, Inc., 869 Washington Street, Canton, MA 02021.

equally in all bands if the visibilities are uncorrelated. Correlations between visibilities from baselines that are nearby in the (u, v) plane are also affected by an error in the aperture efficiency, but numerical simulations show that this effect tends to cancel the error in the visibility sensitivity estimate. The result is that an uncertainty in our knowledge of the aperture efficiency contributes a band-power uncertainty which is constant at 4% except in the three lowest-l bands, where the cancellation of errors causes it to decrease. In using the current DASI results for parameter estimation, we have found no significant difference between treating this small aperture efficiency (beam) uncertainty separately with its low-l variation included, and treating it as constant at 4% to yield a total 1-σ calibration uncertainty of 8%, constant across all band powers (4% in $\Delta T/T$).

5.4 Data Reduction

Raw data from the correlators, along with monitoring data from various telescope systems, are accumulated in 8.4-s integrations. These short integrations are edited before being combined for analysis. Data edits fall into three categories: edits based on hardware or software deficiencies, edits on observing conditions (sun and moon positions or weather), and calibration edits.

In the first category, we reject data from receivers that have warmed beyond nominal threshold temperatures, are absent, for which the LO has lost lock, or where defective IF channel total power diodes prevent us from properly setting the IF gain. Together, these edits reject $\sim 5\%$ of the data. We reject correlator channels for which the real/imaginary gain ratio falls outside the range 0.9 ± 0.3 in amplitude or $0 \pm 20°$ in phase. The range limits were determined from empirical distributions of the gain ratios, and were set to cut the non-Gaussian tails of the distribution, where hardware defects such as a faulty microstrip or multiplier cell were likely to be responsible for the gain imbalance. (The offset from unity in the mean real/imaginary gain ratio is due to asymmetry between the real and imaginary parts of the correlator card.)

We also reject multiplier real/imaginary gain ratios which vary by more than 10% during any 24-hr observing schedule. Together, the multiplier gain ratio edits reject $\sim 11\%$ of the data. Lastly in this category, we trim field observations so that all eight fields are observed over precisely the same azimuth range, so that we may remove a common ground signal during analysis. This edit rejects $\sim 9\%$ of the data.

In the second category, we edit data based on the positions of the sun and moon, and when we detect significant correlations in the noise due to weather. The closest approach of the moon to the pointing axis of the telescope was 36°, and the closest approach of the sun (while above the horizon) was 89°. We have found that baselines with (u, v) radii < 40 are susceptible to contamination from the sun and moon. For these visibilities, we reject data for which either the sun or moon is above the horizon, which is 69% of the data with (u, v) radii < 40. Because of the strong CMB signal on short baselines, this edit, although severe, does not appreciably affect the power spectrum sensitivity. For data with (u, v) radii ≥ 40, no edits are made based on moon or sun position.

The presence of atmospheric fluctuations in the data is most apparent in noise correlations between different visibilities, which are expected to have independent noise. For the weather edit criterion, we calculate the correlation coefficient matrix in each IF channel for every 1-hr field observation. We reject all data if any off-diagonal correlation coefficient in any IF channel exceeds ± 0.36; this edit rejects 5% of the data. This threshold was chosen to reject periods of obviously poor weather. In the power spectrum analysis, we have found that the data consistency does not depend strongly on this edit threshold.

In the third category, we perform edits based on the quality of bracketing celestial calibrator observations. We reject data for which the bracketing calibrator observations differ by 10% in amplitude or 30° in phase. We also reject data if one of the bracketing calibrator observations is shorter than half of its nominal integration time, increasing the statistical uncertainty of the observation to $\gtrsim 3\%$. Together the

calibrator edits reject $\sim 20\%$ of the data.

To minimize the risk of biasing the power spectrum results, we do not edit the data based on the level of the signal. We have varied the threshold values of the weather, calibrator, and lunar/solar edit criteria with no significant effect on the angular power spectrum results.

Collectively, the edits in the three categories above reject $\sim 40\%$ of the data. The edited and calibrated data are combined into 1-hr bins; the uncertainty in the visibility values are estimated from the scatter in the 8.4-s raw integrations. All observations of a given set of fields are then combined, and it is these 1560 combined visibilities per field (78 complex baselines $\times$ 10 correlator channels, before edits) which form the input to the angular power spectrum likelihood analysis.

5.5 Field Images

Although we estimate the CMB angular power spectrum directly from the visibility data without an imaging step, we can also create field images by taking the Fourier transform of the visibility data. Image generation is useful as a visual check to indicate the source and nature of the detected signal, for identifying point sources in the fields, and for comparison with CMB images generated by other experiments. To generate field images, a common ground signal is removed from each visibility for each 8-field observation. Point sources are also apparent in some of the images; we fit for their positions and flux densities from the data and subtract them from the images. The image at this stage is a *dirty map* which shows radial streaks which are due to gaps in the (u, v) plane coverage (i.e., the synthesized beam). A standard deconvolution algorithm, called CLEAN (Högbom 1974), is used to deconvolve the beam from the signal in the center portion of the image. The field image generation process is shown in Fig. 5.2. CLEANed images of five fields, shown in Fig. 5.3, demonstrate that the rms signal attenuates with the expected shape of the DASI primary beam, and that the residual fluctuations at the edge of the map are consistent with instrument noise.

This is a convincing sign that the origin of the signal is on the sky and is not a near-field or instrumental systematic effect.

We emphasize that the ground and point source subtraction technique used here to generate field images is *not* used in the power spectrum analysis. There we use constraint matrices, described in §6.8 and §7.2.4, to marginalize over the ground and point source contributions. The constraint procedure does not require knowledge of the ground signal amplitude or point source flux densities.

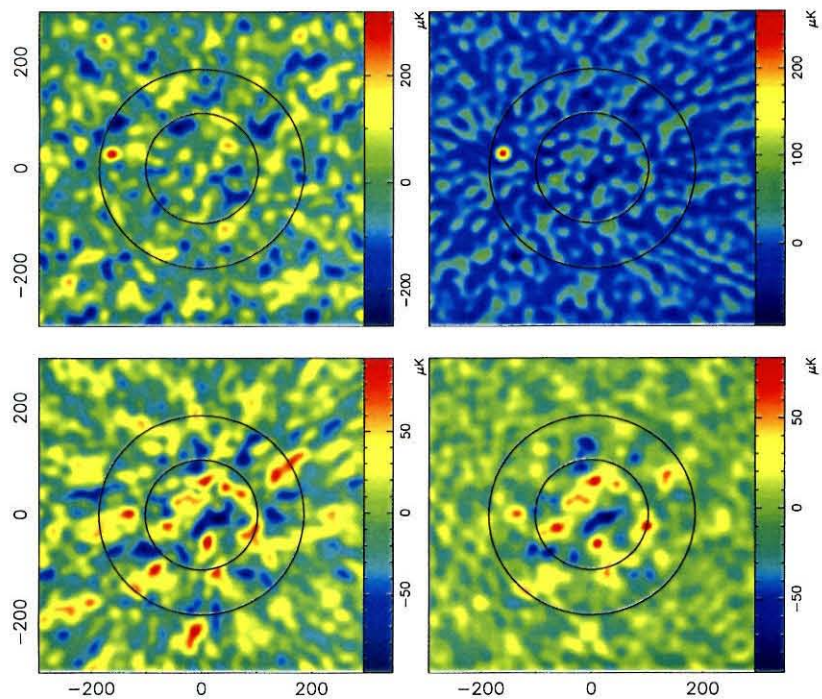

Figure 5.2 A DASI field image (B8) before and after ground and point source removal. The two concentric circles represent the −3 dB and −10 dB taper of the DASI primary beam. The top left panel shows the field image without the ground or point source signals removed. The top right panel shows the image with ground signal removed, revealing a prominent point source. In the lower left panel, both the ground and point source signals have been removed, revealing a spatially extended signal which is tapered by the DASI primary beam. In the lower right panel, the synthesized beam (shown by the point source image in the upper right panel) is deconvolved from the image using the CLEAN algorithm. Field offset coordinates are in arcminutes.

Finally, to display images of the 32 DASI fields (shown in Fig. 5.4), we multiply

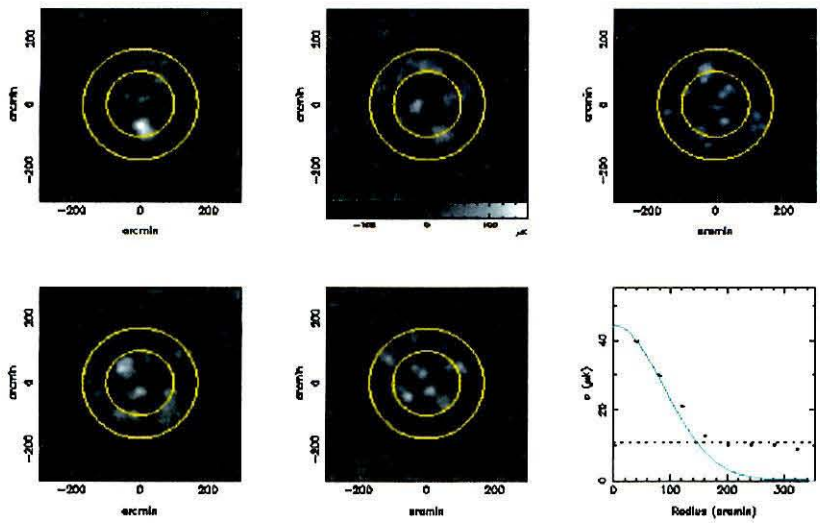

Figure 5.3 CLEANed images of five DASI CMB fields, with ground and point sources signals removed. The two concentric circles represent the −3 dB and −10 dB taper of the DASI primary beam. Fluctuation power enveloped by the primary beam is apparent in the fields, confirming the source is in the far-field of the instrument. The lower right panel shows the rms pixel values for field 5 (lower middle panel) as a function of radius (black points), the primary beam taper normalized to the first rms pixel value (solid line), and the theoretical rms image noise, determined from the scatter in 8.4-s visibility data (dashed line).

the images by the inverse of the DASI primary beam pattern to flatten the response to CMB fluctuations. The resulting rms signal-to-noise ratio is ~ 4 at the centers of the images, and ~ 2 at the edges. These images are high signal-to-noise measurements of CMB anisotropy.

5.6 DASI Detected Point Sources

We employ an iterative technique to detect point sources in the DASI data. We create modified ground-subtracted field images for each field row, excluding baselines $< 64\ \lambda$ where most of the CMB signal is present, to improve the signal-to-noise for point source detection. We divide the individual images by the rms fluctuation level of the CMB and instrument noise. The rms fluctuation level is calculated in annular

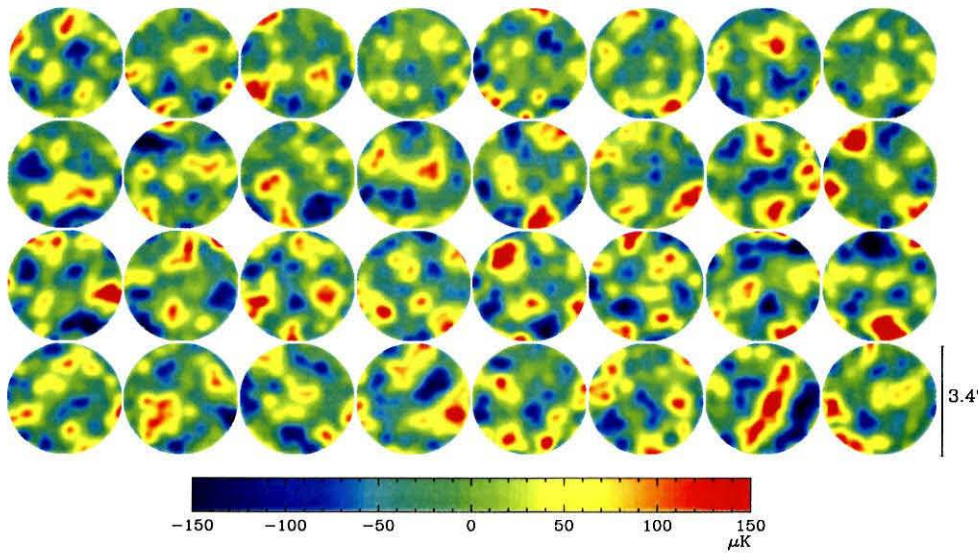

Figure 5.4 Images of the 32 DASI fields, at 20′ resolution. Shown are CLEANed maps of the central 3°.4 FWHM of each primary beam, corrected for the beam taper. Typical rms noise in a 20′ beam is 10 μK at map center, and 20 μK at the edge. Rows are in order of decreasing elevation: B, A, C, D from bottom to top, with RA increasing to the left.

bins for each row of fields, to take into account the primary beam taper. Using the position of the highest amplitude pixel in the 8-fields with at least 4.5-σ significance, a dirty map (i.e., a simulated observation) of a point source with matching flux density is generated, subtracted from the field image, and added back with 1/7 amplitude to the other 7 field images (to compensate for the negative point source flux density in those fields due to ground subtraction). This process is iterated until all point sources detected with $>$ 4.5-σ significance have been removed. Using this technique, we detect 28 point sources in the DASI data; we can detect a 40 mJy source at beam center with $>$ 4.5-σ significance. All have identifiable counterparts in the PMN southern (PMNS) catalog (Wright et al. 1994). The estimated point source flux densities range from 80 mJy to 2.8 Jy, and are tabulated in Table 5.2.

The tabulated point source positions and flux densities are used to subtract the point sources from the field images. These point source positions are also used to

Field	RA (J2000)	Dec (J2000)	X (°) [a]	Y (°) [a]	Flux Density (Jy)[b]	Apparent Flux Density (Jy)[c]
A1	22 03 31.8	-61 37 51.5	0.419	-0.634	0.138	0.105
A3	23 58 51.6	-60 57 51.2	-0.138	0.035	1.319	1.148
A4	01 08 55.4	-60 51 32.7	1.086	0.122	0.622	0.405
A6	03 03 42.0	-62 14 57.2	0.431	-1.252	1.228	0.695
A6	03 09 55.2	-61 03 02.6	1.200	-0.073	1.043	0.639
A6	02 51 21.4	-60 04 12.1	-1.078	0.912	0.499	0.266
A8	05 06 43.5	-61 13 12.5	0.809	-0.231	2.336	1.719
A8	05 03 29.6	-60 52 44.7	0.425	0.118	0.301	0.251
B2	22 28 52.5	-69 08 56.0	-0.100	-2.149	0.550	0.145
B3	23 27 34.1	-66 42 03.9	-0.240	0.298	0.110	0.093
B5	01 12 21.1	-66 35 43.2	-1.751	0.343	0.441	0.172
B7	03 14 24.8	-65 52 26.0	-1.592	1.076	0.141	0.048
B8	04 56 41.0	-66 27 55.4	2.658	0.392	2.801	0.345
B8	04 43 35.4	-66 51 04.0	1.335	0.112	0.090	0.051
C1	22 46 12.7	-56 06 15.9	2.258	-1.170	0.798	0.123
C1	22 38 46.5	-56 59 36.2	1.195	-2.012	0.986	0.204
C5	02 28 10.3	-55 44 03.8	-0.257	-0.735	0.303	0.228
C5	02 23 27.2	-53 44 17.3	-0.968	1.250	0.331	0.155
C5	02 29 01.4	-54 03 41.7	-0.143	0.938	0.081	0.057
C7	04 29 00.9	-53 46 35.9	-0.146	1.223	0.358	0.215
C7	04 25 08.6	-53 31 21.6	-0.722	1.471	0.206	0.092
C8	05 40 29.4	-54 16 37.1	1.531	0.694	0.718	0.308
D2	24 04 29.2	-47 35 54.6	0.756	1.396	0.474	0.220
D2	23 47 40.9	-49 47 10.4	-1.987	-0.827	1.036	0.273
D4	02 10 36.7	-51 00 37.1	1.669	-2.039	6.968	0.934
D5	03 07 20.2	-48 53 10.9	1.206	0.099	0.209	0.127
D7	04 55 52.6	-46 15 18.7	-0.713	2.739	2.280	0.219
D8	05 58 12.9	-50 28 18.7	-0.284	-1.473	0.295	0.147

[a]X and Y offset positions from field center.

[b]26–36 GHz flux density, estimated from the DASI data.

[c]Flux density as measured in the DASI data before compensating for the primary beam taper.

Table 5.2 DASI detected point sources.

constrain point source contributions to the CMB angular power spectrum, §7.2.4.

Chapter 6

Analysis Formalism

6.1 Introduction

The angular power spectrum of the Cosmic Microwave Background is difficult to measure; the fractional temperature fluctuations are $\mathcal{O}(10^{-5})$. Vast improvements in experimental sensitivity have been made since the COBE DMR experiment revealed primordial anisotropy in the CMB with an rms signal-to-noise ratio of unity (Smoot et al. 1992). Yet sophisticated statistical techniques are still required to extract meaningful information from modern-day CMB datasets. In addition, datasets are becoming larger as more sky is measured with increased resolution (de Bernardis et al. 2000; Hanany et al. 2000; Leitch et al. 2001), and two pending all-sky satellite surveys, the Microwave Anisotropy Probe (MAP, Wright 1999), and Planck (Tauber 2000), will yield maps with $\mathcal{O}(10^6)$ pixel elements. Traditional statistical methods to estimate power spectra, such as dense mapping of the likelihood surface, are not computationally feasible with such large datasets, and much effort in recent years has focused on faster algorithms (see, e.g., Tegmark 1997; Bond et al. 2000) to overcome this difficulty.

In this chapter, we discuss the adaptation of these modern techniques, in particular the iterated quadratic estimator of Bond et al. (1998), to interferometer data in general, and to the DASI dataset in particular. We review the formalism of CMB temperature fluctuations (§6.2) and interferometry (§6.3), before we introduce the

datavector and covariance matrix calculations (§6.4) and the simple quadratic estimator (of White et al. 1999a) in §6.5. The maximum likelihood estimator, the iterated quadratic estimator, and refinements are discussed in §6.6 through §6.10, cosmological parameter estimation in §6.11, and finally, an outline of the specific numerical implementation is given in §6.12.

6.2 The Fundamental Observable

Presently favored cosmological theories predict Gaussian random temperature fluctuations on the CMB sky. A given realization of these random fluctuations can be written in terms of a spherical harmonic decomposition,

$$\frac{\Delta T}{T}(\hat{s}) = \sum_{l,m} a_{lm} Y_{lm}(\hat{s}), \tag{6.1}$$

where $\hat{s}$ is a unit 3-vector indicating a point on the celestial sphere. The 2-point correlation function of the sky temperature fluctuations is of particular interest, since for Gaussian random fluctuations it contains all of the information about the underlying Gaussian random variable. The 2-point correlation function is given by (see, e.g., White & Srednicki 1995)

$$C_{\rm sky}(\theta) = \left\langle \frac{\Delta T^*}{T}(\hat{s}_1) \frac{\Delta T}{T}(\hat{s}_2) \right\rangle, \tag{6.2}$$

where $\theta = \cos^{-1}(\hat{s}_1 \cdot \hat{s}_2)$ is the separation angle on the sky, and $\langle\ \rangle$ denotes the ensemble average over many realizations of the CMB sky. Inserting Eq. (6.1) into Eq. (6.2),

$$C_{\rm sky}(\theta) = \left\langle \sum_{l,m} a^*_{lm} Y^*_{lm}(\hat{s}_1) \sum_{l',m'} a_{l'm'} Y_{l'm'}(\hat{s}_2) \right\rangle \tag{6.3}$$

$$= \sum_{l,m} \sum_{l',m'} \langle a^*_{lm} a_{l'm'} \rangle\, Y^*_{lm}(\hat{s}_1) Y_{l'm'}(\hat{s}_2). \tag{6.4}$$

In a Gaussian random realization of the sky, the spherical harmonic coefficients a_{lm} are uncorrelated, have random phase, an expectation value of zero,

$$\langle a_{lm} \rangle = 0, \tag{6.5}$$

and a second moment, or variance, specified by

$$\langle a^*_{lm} a_{l'm'} \rangle = \langle |a_{lm}|^2 \rangle \, \delta_{ll'} \delta_{mm'} \tag{6.6}$$

$$= C_l \delta_{ll'} \delta_{mm'}, \tag{6.7}$$

where

$$C_l \equiv \langle |a_{lm}|^2 \rangle \tag{6.8}$$

is the angular power spectrum, which is independent of m due to the assumed spherical symmetry of the sky. The relationship between the 2-point correlation function $C_{\rm sky}(\theta)$ and the angular power spectrum can be expressed as

$$C_{\rm sky}(\theta) = \sum_l C_l \sum_m Y^*_{lm}(\hat{s}_1) Y_{lm}(\hat{s}_2) \tag{6.9}$$

$$= \frac{1}{4\pi} \sum_l (2l+1) C_l P_l(\hat{s}_1 \cdot \hat{s}_2), \tag{6.10}$$

where in Eq. (6.10) the spherical harmonic addition theorem has been used to convert the series of spherical harmonic products to Legendre polynomials P_l.

For fields that are small in angular extent, the sky can be well approximated as flat. In this limit, the temperature fluctuations can be decomposed into Fourier modes,

$$\frac{\Delta T}{T}(\mathbf{x}) = \int d\mathbf{u} \, \widetilde{\frac{\Delta T}{T}}(\mathbf{u}) \, e^{-i2\pi \mathbf{u}\cdot\mathbf{x}}, \tag{6.11}$$

in analogy with Eq. (6.1); we use $(\tilde{\ })$ to denote the Fourier transform of a function. Here

$$\mathbf{x} \equiv (x, y)$$

$$= ((\hat{s} - \hat{s}_0) \cdot \hat{i}, (\hat{s} - \hat{s}_0) \cdot \hat{j}) \tag{6.12}$$

$$\approx \hat{s} - \hat{s}_0 \tag{6.13}$$

is a 2-vector indicating direction cosines on the sky with respect to the $(\hat{i}, \hat{j})$ sky plane, normal to the field center direction $\hat{s}_0$. For small fields (in which the flat sky approximation applies), x and y are approximately angles on the sky in radians

with respect to $\hat{s}_0$. The Fourier conjugate variable of $\mathbf{x}$ is $\mathbf{u} = (u, v)$, an angular wavevector.

In the flat sky approximation, the sky temperature correlation function, Eq. (6.2), can be written as

$$C_{\rm sky}(|\mathbf{x_2} - \mathbf{x_1}|) = \left\langle \frac{\Delta T^*}{T}(\mathbf{x_1}) \frac{\Delta T}{T}(\mathbf{x_2}) \right\rangle \tag{6.14}$$

$$= \left\langle \int d\mathbf{u} \widetilde{\frac{\Delta T}{T}}^*(\mathbf{u})\, e^{+i2\pi \mathbf{u}\cdot\mathbf{x_1}} \int d\mathbf{u}' \widetilde{\frac{\Delta T}{T}}(\mathbf{u}')\, e^{-i2\pi \mathbf{u}'\cdot\mathbf{x_2}} \right\rangle \tag{6.15}$$

$$= \int d\mathbf{u} \int d\mathbf{u}' \left\langle \widetilde{\frac{\Delta T}{T}}^*(\mathbf{u}) \widetilde{\frac{\Delta T}{T}}(\mathbf{u}') \right\rangle e^{+i2\pi \mathbf{u}\cdot\mathbf{x_1}}\, e^{-i2\pi \mathbf{u}'\cdot\mathbf{x_2}} \tag{6.16}$$

$$= \int d\mathbf{u} \left\langle \widetilde{\frac{\Delta T}{T}}^*(\mathbf{u}) \widetilde{\frac{\Delta T}{T}}(\mathbf{u}) \right\rangle e^{-i2\pi \mathbf{u}\cdot(\mathbf{x_2}-\mathbf{x_1})}, \tag{6.17}$$

where in the last step we have used the fact that

$$\left\langle \widetilde{\frac{\Delta T}{T}}^*(\mathbf{u}) \widetilde{\frac{\Delta T}{T}}(\mathbf{u}') \right\rangle = \left\langle \widetilde{\frac{\Delta T}{T}}^*(\mathbf{u}) \widetilde{\frac{\Delta T}{T}}(\mathbf{u}) \right\rangle \delta(\mathbf{u} - \mathbf{u}') \tag{6.18}$$

in analogy with Eq. (6.6) above, since the temperature fluctuations are assumed to be uncorrelated. The flat sky analog to the angular power spectrum C_l can be identified from Eq. (6.17) as

$$\left\langle \widetilde{\frac{\Delta T}{T}}^*(\mathbf{u}) \widetilde{\frac{\Delta T}{T}}(\mathbf{u}) \right\rangle = \widetilde{C}_{\rm sky}(\mathbf{u}) \tag{6.19}$$

$$\equiv S(u), \tag{6.20}$$

using the notation $S(u)$ for the power spectrum from Hobson et al. (1995) and White et al. (1999a). Note that $S(u)$ is only dependent on the amplitude of $\mathbf{u}$ (here denoted $u \equiv |\mathbf{u}|$, not to be confused with the wavevector components u and v), since the Universe is assumed to have no preferred orientation. For $u \gtrsim 10$, $S(u)$ is related to C_l by (White et al. 1999a)

$$u^2 S(u) \simeq \frac{l(l+1)}{(2\pi)^2} C_l \tag{6.21}$$

where

$$l = 2\pi u. \tag{6.22}$$

The CMB temperature angular power spectrum $S(u)$, or C_l, is a fundamental observable used to test the predictions of cosmological theories. Modern experimental results are usually reported in units of $l(l+1)/(2\pi)C_l$, where scale-invariant primordial fluctuations will appear as constant in l; we define

$$\mathcal{C}_l \equiv \frac{l(l+1)}{2\pi}C_l \tag{6.23}$$

$$\mathcal{S}(u) \equiv u^2 S(u) \tag{6.24}$$

$$= \mathcal{C}_l/(2\pi), \tag{6.25}$$

which we use in the discussion that follows.

6.3 The Interferometer Response

An interferometer such as DASI directly measures the Fourier transform of the sky brightness temperature. For any given pair of antennas, this is achieved by taking the time average of the product of the two signals (see Fig. 6.1). Let the electric field in a given direction of the sky $\hat{s}$ be given by

$$E(\hat{s},t) = E_0(\hat{s})\sin(2\pi\nu t) \tag{6.26}$$

where ν is the RF frequency of the wave. The product of the outputs of the receivers with the geometry depicted in Fig. 6.1 is

$$F(\hat{s}) \propto E(\hat{s},t)E(\hat{s},t-\tau) \tag{6.27}$$

$$\propto E_0(\hat{s})\sin(2\pi\nu t)E_0(\hat{s})\sin(2\pi\nu(t-\tau)) \tag{6.28}$$

$$\propto \frac{1}{2}E_0^2(\hat{s})(\cos(2\pi\nu\tau) - \cos(2\pi\nu(\tau+2t)). \tag{6.29}$$

The output of the correlator is the time average of this product, and the rapidly oscillating second term vanishes with sufficient integration time.

The resulting DC output signal is called the visibility, and represents the amplitude of a corrugation on the sky with a spatial wavelength that is inversely proportional

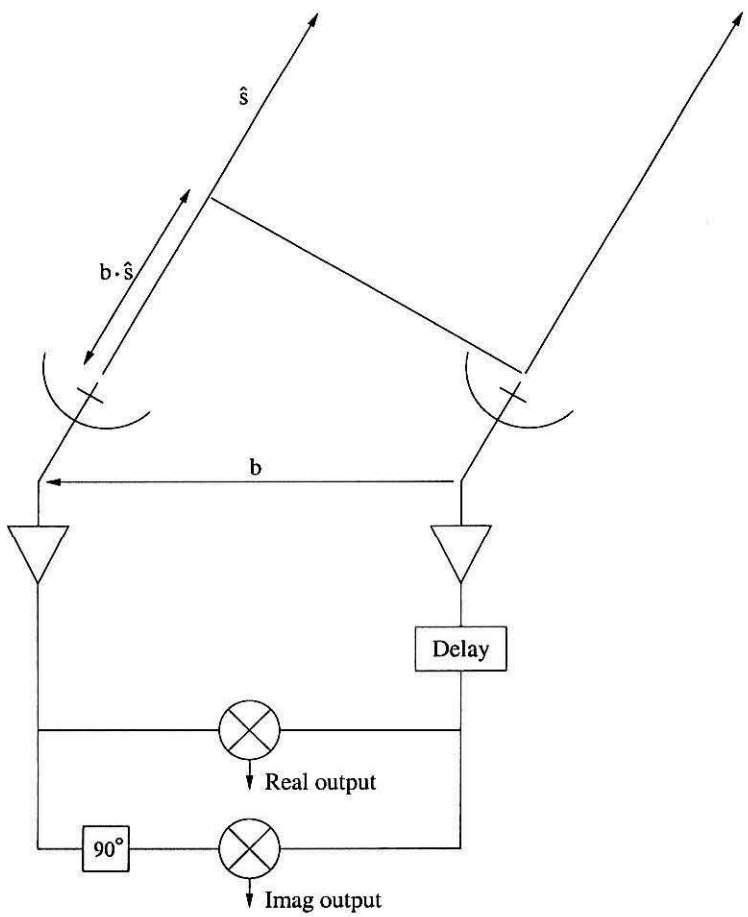

Figure 6.1 Simple schematic of a two-element interferometer. The 90° phase shift in front of one of the output multipliers allows both the real and imaginary components of the complex visibility to be measured. The phase of the integrated output depends on the direction $\hat{\mathbf{s}}$, resulting in a sinusoidal response pattern on the sky which is inversely proportional to the baseline length $|\mathbf{b}|$. The delay at phase center, $\tau_0 = \mathbf{b} \cdot \hat{\mathbf{s}}_0$, is usually compensated with a variable delay, shown on the right receiver. However, in the DASI instrument, all receivers are fixed to an aperture plate which is used to point the array, eliminating the need for a variable delay.

to the projected separation of the antenna pair in the direction of the source. A corrugation with a spatial phase shifted by 90° can also be sampled by taking a second time average product of the receiver output signals, with one signal delayed by 90°; this represents the imaginary part of the visibility. The resulting complex visibility is given by

$$V(\mathbf{u}) = \int d\mathbf{x}\, A(\mathbf{x},\nu) I(\mathbf{x}) e^{-i2\pi \mathbf{u}\cdot\mathbf{x}}. \tag{6.30}$$

Here, $A(\mathbf{x},\nu)$ is the single antenna beam pattern at observing frequency ν, normalized such that $A(\mathbf{0},\nu) = 1$, $I(\mathbf{x})$ is the sky brightness distribution, $\mathbf{u} = (\mathbf{b}/\lambda \cdot \hat{i}, \mathbf{b}/\lambda \cdot \hat{j})$ is the projection of the antenna separation vector $\mathbf{b}$ (called the *baseline*) in the plane normal to the direction of the source $\hat{s}_0$, expressed in units of the observing wavelength $\lambda = c/\nu$. The vector components $\mathbf{x}$ are the direction cosines on the sky; the origin of $\mathbf{x}$, in the direction $\hat{s}_0$, is called the *phase center*. Note that DASI differs from most conventional interferometers in that the antenna elements are fixed on an aperture plate rather than individually steerable. A variable delay line, used to eliminate the delay $\tau = (\mathbf{b}\cdot\hat{s}_0)/c$ in systems with individually steerable antennas, is unnecessary. An exhaustive development of the expression for the visibility can be found in Thompson et al. (1991).

When observing the CMB, the above expression for the visibility can be rewritten in terms of the fractional CMB temperature fluctuations defined in Eq. (6.1),

$$V(\mathbf{u}) = \frac{\partial B_\nu}{\partial T} T \int d\mathbf{x}\, A(\mathbf{x},\nu) \frac{\Delta T}{T}(\mathbf{x}) e^{-i2\pi \mathbf{u}\cdot\mathbf{x}} \tag{6.31}$$

$$= \frac{2k_B T \nu^2}{c^2} g(\nu) \int d\mathbf{x}\, A(\mathbf{x},\nu) \frac{\Delta T}{T}(\mathbf{x}) e^{-i2\pi \mathbf{u}\cdot\mathbf{x}}, \tag{6.32}$$

where T is the temperature of the CMB, B_ν is the Planck function, k_B is Boltzmann's constant, and $g(\nu)$ corrects for the difference between derivatives of the Rayleigh-Jeans and Planck functions, a $\sim 2\%$ correction at our observing frequency. Finally, the visibility can be written in terms of the Fourier transform of the beam pattern convolved with the Fourier transform of the CMB temperature fluctuations,

$$V(\mathbf{u}) = \frac{2k_B T \nu^2}{c^2} g(\nu)\ \widetilde{A}(\mathbf{u},\nu) * \widetilde{\frac{\Delta T}{T}}(\mathbf{u}). \tag{6.33}$$

From this expression, it is clear that the visibility is a direct measure of the Fourier transform of the sky temperature fluctuations centered at the angular wavevector $\mathbf{u}$. The variance of the visibility, $\langle V^*(\mathbf{u})V(\mathbf{u})\rangle$, is closely related to the power spectrum $\mathcal{S}(u)$ [see Eq. (6.20)], the observable we desire to measure, as will be discussed in more detail below.

6.4 The Datavector and Data Covariance Matrix

For any CMB experiment, the raw time-stream data are calibrated and binned to form a manageable set of numbers, called the *datavector*, from which an estimator of the angular power spectrum may be constructed. For a modern single-dish experiment, this datavector is usually a pixelized temperature map of the sky. For an interferometric experiment such as DASI, the datavector consists of calibrated time-averaged visibilities. In the analysis described below, we treat the real and imaginary parts of the visibility as separate elements of the datavector,

$$V(\mathbf{u}) \equiv V^R(\mathbf{u}) + iV^I(\mathbf{u}). \tag{6.34}$$

DASI has 78 baselines $\times$ 10 IF bands $\times$ 2 complex components = 1560 time-averaged visibility values for each pointing on the sky. For the first season of observations with DASI, we observed a total of 32 separate fields, one deck rotation per field, for a total datavector length (before cuts) of $32 \times 1560 = 49,920$. The angular power spectrum is estimated directly from the visibility datavector.

The datavector can be written as

$$\mathbf{\Delta} = \mathbf{s} + \mathbf{n}, \tag{6.35}$$

where $\mathbf{s}$ is the sky signal component and $\mathbf{n}$ is the noise component. A signal datavector element is simply the real or imaginary part of the visibility described above,

$$s_i = V_i^R \text{ or } V_i^I. \tag{6.36}$$

The expectation value of both the signal and noise components is zero,

$$\langle \mathbf{s} \rangle = \langle \mathbf{n} \rangle = \mathbf{0}, \tag{6.37}$$

since the sky signal is assumed to be a Gaussian random variable and the interferometer output is insensitive to the CMB monopole moment, and the noise is also assumed to be well behaved. Of course, in the real world, instrumental (systematic) offsets and non-CMB sky signals which do not fit this model are present at some level; these are addressed with the constraint matrix formalism described in §6.8.

In order to construct an estimator for the angular power spectrum, the covariance matrix of the datavector must be known, since it describes the filter, particular to a given instrument and data binning, through which the sky signal and noise enter the data. The covariance matrix is given by

$$\begin{aligned} C &= \langle \Delta_i \Delta_j \rangle & (6.38)\\ &= \langle s_i s_j \rangle + \langle n_i n_j \rangle & (6.39)\\ &= C_T + C_n, & (6.40) \end{aligned}$$

assuming $\mathbf{s}$ and $\mathbf{n}$ are uncorrelated, where

$$C_T \equiv \langle s_i s_j \rangle \tag{6.41}$$

is called the *theory* or *signal covariance matrix*, and

$$C_n \equiv \langle n_i n_j \rangle \tag{6.42}$$

is the noise covariance matrix.

6.4.1 The Theory Covariance Matrix

The theory covariance matrix contains the information about how a given power spectrum $\mathcal{S}(u)$ presents itself, on average, in the quadratic pairings of the datavector elements. Traditionally (see, e.g., White & Srednicki 1995), the theory covariance

matrix is described in terms of so-called *variance window functions* (or simply *window functions*) $W_{l,ij}$,

$$C_{Tij} = \sum_l \frac{W_{l,ij}}{l} C_l \tag{6.43}$$

$$= \int_0^\infty du \frac{\mathcal{W}_{ij}(u)}{u} \mathcal{S}(u). \tag{6.44}$$

The window functions describe the contribution of the angular power spectrum to a given covariance matrix element as a function of l or u. Window functions for each individual multipole moment l or fine increment du need not be calculated if the theoretical power spectrum is assumed to be flat over larger bands in l or u.

Following White et al. (1999b), we first consider the theory covariance matrix element between two real visibility datavector elements for the same field on the sky. The theory covariance matrix elements are derived using Eq. (6.33) for the visibility:

$$C_{Tij}^{R/R} \equiv \langle V^R(\mathbf{u}_i) V^R(\mathbf{u}_j) \rangle \tag{6.45}$$

$$= \alpha_i \alpha_j \left\langle \mathrm{Re}\left(\widetilde{A}(\mathbf{u}_i, \nu_i) * \widetilde{\frac{\Delta T}{T}}(\mathbf{u}_i) \right) \mathrm{Re}\left(\widetilde{A}(\mathbf{u}_j, \nu_j) * \widetilde{\frac{\Delta T}{T}}(\mathbf{u}_j) \right) \right\rangle \tag{6.46}$$

$$= \alpha_i \alpha_j \left\langle \mathrm{Re}\left(\int d\mathbf{u} \widetilde{\frac{\Delta T}{T}}(\mathbf{u}) \widetilde{A}(\mathbf{u}_i - \mathbf{u}, \nu_i) \right) \right.$$
$$\left. \times \mathrm{Re}\left(\int d\mathbf{u}' \widetilde{\frac{\Delta T}{T}}(\mathbf{u}') \widetilde{A}(\mathbf{u}_j - \mathbf{u}', \nu_j) \right) \right\rangle, \tag{6.47}$$

where

$$\alpha_i = \frac{2 k_B T}{c^2} \nu_i^2 g(\nu_i) \tag{6.48}$$

is the pre-constant in Eq. (6.33). Recall that

$$\mathrm{Re}\,(AB) = \mathrm{Re}\,(A)\,\mathrm{Re}\,(B) - \mathrm{Im}\,(A)\,\mathrm{Im}\,(B)\,, \tag{6.49}$$

so that

$$C_{Tij}^{R/R} = \alpha_i \alpha_j \int d\mathbf{u} \int d\mathbf{u}' \left\langle \left[\mathrm{Re}\left(\widetilde{\frac{\Delta T}{T}}(\mathbf{u}) \right) \mathrm{Re}\left(\widetilde{A}(\mathbf{u}_i - \mathbf{u}, \nu_i) \right) \right.\right.$$

$$
\begin{aligned}
& -\mathrm{Im}\left(\widetilde{\frac{\Delta T}{T}}(\mathbf{u})\right)\mathrm{Im}\left(\widetilde{A}(\mathbf{u}_i-\mathbf{u},\nu_i)\right)\Bigg] \\
& \times\Bigg[\mathrm{Re}\left(\widetilde{\frac{\Delta T}{T}}(\mathbf{u}')\right)\mathrm{Re}\left(\widetilde{A}(\mathbf{u}_j-\mathbf{u}',\nu_j\right) \\
& -\mathrm{Im}\left(\widetilde{\frac{\Delta T}{T}}(\mathbf{u}')\right)\mathrm{Im}\left(\widetilde{A}(\mathbf{u}_j-\mathbf{u}',\nu_j\right)\Bigg]\Bigg\rangle \qquad (6.50)
\end{aligned}
$$

$$
\begin{aligned}
= \; & \alpha_i\alpha_j\int d\mathbf{u}\int d\mathbf{u}'\left\langle \mathrm{Re}\left(\widetilde{\frac{\Delta T}{T}}(\mathbf{u})\right)\mathrm{Re}\left(\widetilde{\frac{\Delta T}{T}}(\mathbf{u}')\right)\right\rangle \\
& \times \mathrm{Re}\left(\widetilde{A}(\mathbf{u}_i-\mathbf{u},\nu_i)\right)\mathrm{Re}\left(\widetilde{A}(\mathbf{u}_j-\mathbf{u}',\nu_j\right), \qquad (6.51)
\end{aligned}
$$

where we have made use of the fact that our beam is symmetric, hence $\mathrm{Im}\left(\widetilde{A}\right)=0$. We can also make use of the fact that the temperature fluctuations are a real (scalar) function on the sky, so that

$$
\widetilde{\frac{\Delta T}{T}}^{*}(\mathbf{u}) = \widetilde{\frac{\Delta T}{T}}(-\mathbf{u}). \qquad (6.52)
$$

Then,

$$
\begin{aligned}
& \left\langle \mathrm{Re}\left(\widetilde{\frac{\Delta T}{T}}(\mathbf{u})\right)\mathrm{Re}\left(\widetilde{\frac{\Delta T}{T}}(\mathbf{u}')\right)\right\rangle = \\
& \quad \left\langle \frac{1}{2}\left(\widetilde{\frac{\Delta T}{T}}(\mathbf{u})+\widetilde{\frac{\Delta T}{T}}^{*}(\mathbf{u})\right)\times\frac{1}{2}\left(\widetilde{\frac{\Delta T}{T}}(\mathbf{u}')+\widetilde{\frac{\Delta T}{T}}^{*}(\mathbf{u}')\right)\right\rangle \qquad (6.53) \\
= \; & \frac{1}{4}\Bigg[\left\langle\widetilde{\frac{\Delta T}{T}}^{*}(-\mathbf{u})\widetilde{\frac{\Delta T}{T}}(\mathbf{u}')\right\rangle+\left\langle\widetilde{\frac{\Delta T}{T}}^{*}(\mathbf{u})\widetilde{\frac{\Delta T}{T}}(-\mathbf{u}')\right\rangle \\
& \quad +\left\langle\widetilde{\frac{\Delta T}{T}}^{*}(\mathbf{u})\widetilde{\frac{\Delta T}{T}}(\mathbf{u}')\right\rangle+\left\langle\widetilde{\frac{\Delta T}{T}}^{*}(-\mathbf{u})\widetilde{\frac{\Delta T}{T}}(-\mathbf{u}')\right\rangle\Bigg] \qquad (6.54) \\
= \; & \frac{1}{4}\left[S(u)\delta(-\mathbf{u},\mathbf{u}')+S(u)\delta(\mathbf{u},-\mathbf{u}')\right. \\
& \quad \left.+S(u)\delta(\mathbf{u},\mathbf{u}')+S(u)\delta(-\mathbf{u},-\mathbf{u}')\right] \qquad (6.55) \\
= \; & \frac{1}{2}\left[S(u)\delta(\mathbf{u},\mathbf{u}')+S(u)\delta(\mathbf{u},-\mathbf{u}')\right], \qquad (6.56)
\end{aligned}
$$

making use of Eq. (6.20) in the third step. Finally, the theory covariance matrix element is reduced to

$$
C_{Tij}^{R/R} = \frac{1}{2}\alpha_i\alpha_j\int d\mathbf{u}\,\frac{\mathcal{S}(u)}{u^2}\widetilde{A}(\mathbf{u}_i-\mathbf{u},\nu_i)\left[\widetilde{A}(\mathbf{u}_j-\mathbf{u},\nu_j)+\widetilde{A}(\mathbf{u}_j+\mathbf{u},\nu_j)\right]. \qquad (6.57)
$$

Similarly, the theory covariance matrix element for two imaginary visibilities is

$$C_{Tij}^{I/I} = \frac{1}{2}\alpha_i\alpha_j \int d\mathbf{u}\, \frac{\mathcal{S}(u)}{u^2} \widetilde{A}(\mathbf{u}_i - \mathbf{u}, \nu_i) \left[\widetilde{A}(\mathbf{u}_j - \mathbf{u}, \nu_j) - \widetilde{A}(\mathbf{u}_j + \mathbf{u}, \nu_j)\right]. \quad (6.58)$$

The covariance between real and imaginary visibilities can be shown to vanish,

$$C_{Tij}^{R/I} = C_{Tij}^{I/R} = 0, \quad (6.59)$$

due to the fact that symmetric (real) and antisymmetric (imaginary) modes are always orthogonal. These do not vanish in the case of interfield correlations, discussed later in this section.

The function $\widetilde{A}(\mathbf{u}, \nu)$ is the autocorrelation function of the aperture field distribution. It therefore falls to zero for $u > D/\lambda$, where $D = 20$ cm is the aperture diameter. A plot of the aperture autocorrelation function for the DASI horns is shown in Fig. 6.2. Note that except for the shortest baselines, only one of the additive terms in the integrand is non-zero, since the autocorrelation functions $\widetilde{A}(\mathbf{u}_j - \mathbf{u}, \nu)$ and $\widetilde{A}(\mathbf{u}_j + \mathbf{u}, \nu)$ are widely separated in the (u, v) plane (see Fig. 6.3).

The window function defined in Eq. (6.44) is given by

$$\mathcal{W}_{ij}(u) = \alpha_i\alpha_j \int_0^{2\pi} d\phi_u \widetilde{A}(\mathbf{u}_i - \mathbf{u}, \nu_i) \left[\widetilde{A}(\mathbf{u}_j - \mathbf{u}, \nu_j) \pm \widetilde{A}(\mathbf{u}_j + \mathbf{u}, \nu_j)\right], \quad (6.60)$$

where ϕ_u is the azimuthal polar coordinate of $\mathbf{u}$ and $+$, $-$ are used for the R/R and I/I covariance matrix elements, respectively. The window function for a diagonal element of the DASI covariance matrix, for a baseline with $|\mathbf{u}_i| = 100$ and an observing wavelength $\lambda = 1$ cm, is shown in Fig. 6.4. As for the autocorrelation function $\widetilde{A}(\mathbf{u})$, the window function goes identically to zero for $|\mathbf{u}| - |\mathbf{u}_i| > D/\lambda$. The integrated area of a given window function $\mathcal{W}_{ij}(u)/u$ indicates the sensitivity to a power spectrum flat in $\mathcal{S}(u)$, and falls off as $1/u^2$.

It is conventional in the modern literature to assume the power spectrum is piecewise flat in $\mathcal{S}(u)$ in several bands for the purposes of estimating the power spectrum from the data. In this case (which we adopt in the likelihood analysis below), it is unnecessary to calculate the one-dimensional window functions of Eq. (6.60). Rather,

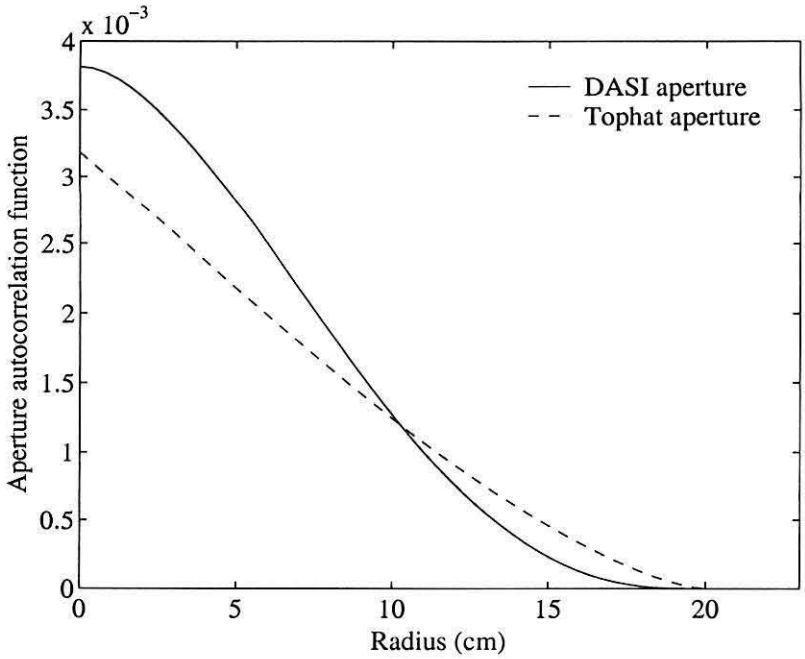

Figure 6.2 The aperture autocorrelation function $\widetilde{A}(r/\lambda)$ for the DASI horn, and a horn with a tophat field illumination, as a function of radius. The normalization shown follows from the beam pattern normalization, $A(0) = 1$.

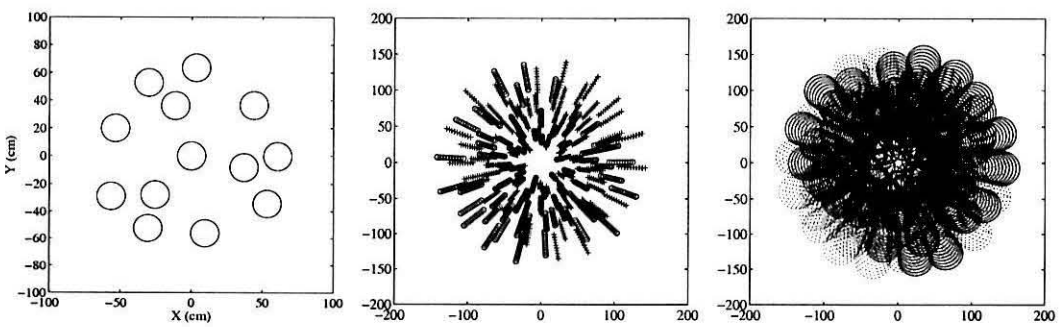

Figure 6.3 The aperture configuration and (u, v) plane coverage. The left panel depicts the physical positions of the antenna apertures on the aperture plate. The central panel shows the center points of the resulting (u, v) coverage (+), and their mirror points (o) which are also measured, due to the fact that the sky intensity is a real (scalar) function. The right panel shows the limits of the autocorrelation function (see Fig. 6.2), for the (u, v) locations in the center panel, with solid lines for the (u, v) locations and dashed lines for their mirror points.

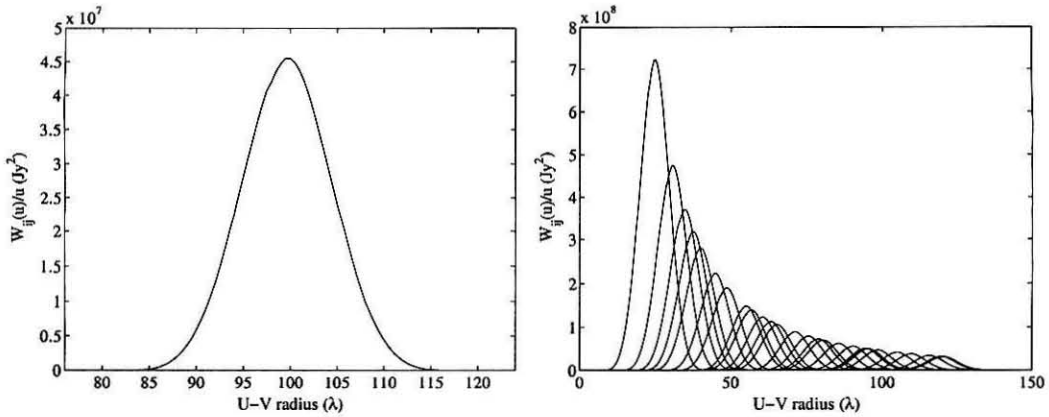

Figure 6.4 The diagonal DASI variance window functions for a baseline with $|\mathbf{u}| = 100$ (left panel) and for all baselines (right panel), for $\lambda = 1$ cm. Each baseline is sensitive to a total range $\Delta u_{\rm tot} = 2D/\lambda \approx 40$ with a FWHM range $\Delta u \approx 10$ corresponding to $\Delta l \approx 60$. The area under a given window function indicates the sensitivity of the baseline to a power spectrum flat in $\mathcal{S}(u)$; the sensitivity falls off as $1/u^2$. Note that since DASI observes at a range of frequencies, the minimum and maximum coverage in u extend beyond the limits shown in the right panel.

for a piecewise-flat band p, the two-dimensional integrals in Eqs. (6.57) and (6.58) may be evaluated directly,

$$B_{p_{ij}} = \frac{1}{2}\alpha_i\alpha_j \int_{u_{l_p}}^{u_{h_p}} \frac{d\mathbf{u}}{u^2}\, \widetilde{A}(\mathbf{u}_i - \mathbf{u}, \nu_i)\left[\widetilde{A}(\mathbf{u}_j - \mathbf{u}, \nu_j) \pm \widetilde{A}(\mathbf{u}_j + \mathbf{u}, \nu_j)\right], \qquad (6.61)$$

where u_{lp} and u_{hp} are the lower and upper (u, v) radii of band p, respectively. Equation (6.61) represents the instrument filter function that translates a theoretical flat band power $\mathcal{S}_p$ into its contribution to the data covariance matrix element. For a set $\mathcal{S}$ of flat band powers

$$C_{Tij}(\mathcal{S}) = \sum_p \mathcal{S}_p B_{p_{ij}}. \qquad (6.62)$$

Numerical calculation of the theory covariance matrix elements is discussed in §6.12.

Interfield Correlations

Correlations between different fields on the sky become important if the fields are spaced sufficiently close together that the primary beams have significant overlap, as

is the case with mosaic mapping. For the first year of DASI observations, the fields were chosen to be widely separated on the sky, to increase the number of independent sky samples; as a result, interfield correlations for most of the DASI fields are small and can be neglected. However, for the highest elevation row, at $\delta = -67°$, the fields are only separated by 5.8° on the sky, where the interfield correlations begin to have a significant impact on the power spectrum estimate at the lowest multipole moments. For this field row only, we take into account the interfield correlations.

In the flat sky approximation, the interfield theory covariance matrix elements are straightforward to derive. We redefine the coordinate system of the sky temperature distribution function to be fixed at an absolute reference position on the sky. For a field m with center position $\mathbf{x}_m$ in this coordinate system, a phase gradient term in the visibility is introduced,

$$\begin{aligned} V_{im} &\equiv V_m(\mathbf{u}_i) && (6.63)\\ &= \alpha_i \int d\mathbf{x}\, A(\mathbf{x},\nu_i)\frac{\Delta T}{T}(\mathbf{x}+\mathbf{x}_m)e^{-i2\pi\mathbf{u}_i\cdot\mathbf{x}} && (6.64)\\ &= e^{+i2\pi\mathbf{u}_i\cdot\mathbf{x}_m}\alpha_i\widetilde{A}(\mathbf{u},\nu_i) * \widetilde{\frac{\Delta T}{T}}(\mathbf{u}_i), && (6.65)\end{aligned}$$

with resulting theory covariance matrix elements:

$$\begin{aligned} C^{R/R}_{Tim,jm'} &= \langle V^R_{im} V^R_{jm'}\rangle && (6.66)\\ &= \frac{1}{2}\alpha_i\alpha_j \int d\mathbf{u}\, \frac{\mathcal{S}(u)}{u^2}\widetilde{A}(\mathbf{u}_i-\mathbf{u},\nu_i)\\ &\quad\times\Big[\widetilde{A}(\mathbf{u}_j-\mathbf{u},\nu_j)\cos(2\pi\mathbf{u}\cdot(\mathbf{x}_m-\mathbf{x}_{m'}))\\ &\quad\quad+\widetilde{A}(\mathbf{u}_j+\mathbf{u},\nu_j)\cos(2\pi\mathbf{u}\cdot(\mathbf{x}_m-\mathbf{x}_{m'}))\Big], && (6.67)\end{aligned}$$

$$\begin{aligned} C^{I/I}_{Tim,jm'} &= \langle V^I_{im} V^I_{jm'}\rangle && (6.68)\\ &= \frac{1}{2}\alpha_i\alpha_j \int d\mathbf{u}\, \frac{\mathcal{S}(u)}{u^2}\widetilde{A}(\mathbf{u}_i-\mathbf{u},\nu_i)\\ &\quad\times\Big[\widetilde{A}(\mathbf{u}_j-\mathbf{u},\nu_j)\cos(2\pi\mathbf{u}\cdot(\mathbf{x}_m-\mathbf{x}_{m'}))\\ &\quad\quad-\widetilde{A}(\mathbf{u}_j+\mathbf{u},\nu_j)\cos(2\pi\mathbf{u}\cdot(\mathbf{x}_m-\mathbf{x}_{m'}))\Big], && (6.69)\end{aligned}$$

$$C^{R/I}_{Tim,jm'} = \langle V^R_{im} V^I_{jm'} \rangle \tag{6.70}$$

$$= \frac{1}{2}\alpha_i\alpha_j \int d\mathbf{u}\, \frac{\mathcal{S}(u)}{u^2} \widetilde{A}(\mathbf{u}_i - \mathbf{u}, \nu_i) \times \Big[-\widetilde{A}(\mathbf{u}_j - \mathbf{u}, \nu_j) \sin(2\pi\mathbf{u}\cdot(\mathbf{x}_m - \mathbf{x}_{m'})) + \widetilde{A}(\mathbf{u}_j + \mathbf{u}, \nu_j) \sin(2\pi\mathbf{u}\cdot(\mathbf{x}_m - \mathbf{x}_{m'})) \Big], \tag{6.71}$$

$$C^{I/R}_{Tim,jm'} = \langle V^I_{im} V^R_{jm'} \rangle \tag{6.72}$$

$$= \frac{1}{2}\alpha_i\alpha_j \int d\mathbf{u}\, \frac{\mathcal{S}(u)}{u^2} \widetilde{A}(\mathbf{u}_i - \mathbf{u}, \nu_i) \times \Big[\widetilde{A}(\mathbf{u}_j - \mathbf{u}, \nu_j) \sin(2\pi\mathbf{u}\cdot(\mathbf{x}_m - \mathbf{x}_{m'})) + \widetilde{A}(\mathbf{u}_j + \mathbf{u}, \nu_j) \sin(2\pi\mathbf{u}\cdot(\mathbf{x}_m - \mathbf{x}_{m'})) \Big]. \tag{6.73}$$

Comparing the equations above to Eqs. (6.57) and (6.58), there is (as expected from the shift theorem) an additional sinusoidally oscillating term with spatial frequency proportional to the field offset vector $\mathbf{x}_m - \mathbf{x}_{m'}$ which has the general effect of diminishing the amplitude of the covariance matrix element relative to the equivalent element with no field offset.

While the above equations serve to lend intuition about the general behavior of interfield correlations, the DASI fields are spaced sufficiently far apart (1^h in RA) that, unfortunately, curvature of the celestial plane cannot be neglected. Among other difficulties, the (u, v) coordinate projection from the orthographic projection plane centered on field m to that centered on field m' introduces a rotation and length distortion. In addition, the finite correlation bandwidth $\Delta\nu$ introduces an effective attenuation (called the *delay beam*), which is important on the angular separations of the DASI fields and which therefore must be taken into account. The angular power spectrum analysis package written by the author, called `dasipower` (see §6.12), accounts for orthographic projection effects and integrates over the finite bandwidth of the DASI frequency channels in order to accurately calculate the interfield covariance matrix elements when necessary.

6.4.2 The Noise Covariance Matrix

The noise covariance of a simple multiplying correlator, or equivalently, the real or imaginary output of a complex correlator, is given by (White et al. 1999b; Thompson et al. 1991):

$$C_{nij} = G^2 \left(\frac{T_{\rm sys}}{\eta_{\rm s}\sqrt{2\Delta\nu\Delta t}} \right)^2 \delta_{ij} \tag{6.74}$$

$$= \left(\frac{k_B T_{\rm sys}}{\eta_{\rm s}\eta_{\rm a} A_{\rm p}} \right)^2 \frac{2}{\Delta\nu\Delta t} \delta_{ij}, \tag{6.75}$$

where G is the antenna gain [Eq. (3.12)], $T_{\rm sys}$ is the system temperature (assumed to be the same for both antennas), $A_{\rm p}$ is the physical aperture area, $\Delta\nu$ is the IF bandwidth of the correlator, Δt is the integration time, and $\eta_{\rm s}$ is a system efficiency factor, generally near unity. This expression is nearly equivalent to the radiometer equation for a single antenna, but for the additional factor $1/\sqrt{2}$, which is due to the fact that the noise voltage for the two separate antennas is uncorrelated. It can easily be shown that the off-diagonal elements of the noise covariance matrix vanish, even for baselines which share one antenna.

6.4.3 Visibility Sensitivity

Taking the square root of the ratio of Eq. (6.57) to Eq. (6.75) will give us an estimate of the rms signal-to-noise ρ for a given visibility:

$$\rho_i \equiv \sqrt{\frac{C_{Tii}}{C_{nii}}} \tag{6.76}$$

$$\approx \frac{\nu^2}{c^2} \frac{T_{\rm CMB}}{T_{\rm sys}} \eta_{\rm s} \left[\Delta\nu\Delta t \frac{\mathcal{S}(u)}{u^2} A_{\rm eff}^2 \int d\mathbf{u}\, \widetilde{A}^2(\mathbf{u},\nu) \right]^{1/2} \tag{6.77}$$

$$\approx \frac{0.24}{u} \left(\frac{\nu}{30\ {\rm GHz}} \right)^2 \left(\frac{T_{sys}}{30\ {\rm K}} \right)^{-1} \left(\frac{\Delta\nu}{1\ {\rm GHz}} \right)^{1/2} \left(\frac{\Delta t}{1\ {\rm s}} \right)^{1/2}$$
$$\times \left(\frac{\mathcal{S}(u)}{2000\ \mu{\rm K}^2} \right)^{1/2} \left(\frac{A_{\rm eff}}{262\ {\rm cm}^2} \right)^{1/2}, \tag{6.78}$$

where we have assumed $\mathcal{S}(u)$ and u^2 are roughly constant over the width of the autocorrelation function in order to remove them from the integral, and $A_{\rm eff} = \eta_{\rm a} A_{\rm p}$

is the effective area of the aperture. For the DASI aperture at $\nu = 30$ GHz,

$$A_{\rm eff}^2 \int d\mathbf{u}\, \widetilde{A}^2(\mathbf{u}, \nu) = 136 \text{ cm}^4. \tag{6.79}$$

This quantity scales linearly with aperture area. Uncertainty in $A_{\rm eff}$ will translate into a scaling uncertainty for the power spectrum which is independent of baseline except for the shortest, most correlated baselines.

6.5 The Simple Quadratic Estimator

Since every visibility, or datavector element, is a direct measurement of the Fourier transform of the sky plane, a simple estimate of the angular power spectrum $\mathcal{S}(u)$ may be constructed from any individual datavector element, or subset of elements. While we choose to implement a full likelihood analysis of the angular power spectrum, described in §6.6 below, the simple quadratic estimator, introduced by White et al. (1999b), is a convenient and quick way to estimate the angular power spectrum from the data, estimate power spectrum sensitivity, and plan observing strategies to achieve a given science goal.

We use the following notational convention in the discussion of various estimators in the sections below. Typically, we assume a probability distribution function (PDF) for the datavector $\mathbf{\Delta}$ which is also a function of some set of parameters κ. The PDF is denoted $P(\mathbf{\Delta}|\kappa)$, and the *true* value of the parameters is denoted κ_0. We desire to estimate κ_0 from the data, so we construct a set of estimators (which are random variables), denoted by $\hat{\kappa}$, from the data $\mathbf{\Delta}$ (another set of random variables), which we hope approximate the true values of the parameters κ_0. An *unbiased* estimator has the property

$$\langle \hat{\kappa} \rangle = \kappa_0. \tag{6.80}$$

We use ($\hat{}$) to indicate estimators and ($_0$) to indicate true values in the sections on estimators below.

For a given datavector element, an estimator of the power spectrum is given by

$$\hat{\mathcal{S}}_i = \frac{\Delta_i^2 - C_{nii}}{B_{ii}} \tag{6.81}$$

where B_{ii} is the instrument filter function, Eq. (6.61), for a single flat band power $\mathcal{S}$ spanning all (u, v) radii. The expectation value of $\hat{\mathcal{S}}_i$ is then

$$\begin{aligned}
\left\langle \hat{\mathcal{S}}_i \right\rangle &= \left\langle \frac{\Delta_i^2 - C_{nii}}{B_{ii}} \right\rangle && (6.82)\\
&= \frac{\langle \Delta_i^2 \rangle - C_{nii}}{B_{ii}} && (6.83)\\
&= \frac{\langle (s_i + n_i)^2 \rangle - C_{nii}}{B_{ii}} && (6.84)\\
&= \frac{\langle s_i^2 \rangle + \langle n_i^2 \rangle - C_{nii}}{B_{ii}} && (6.85)\\
&= \frac{C_{Tii}}{B_{ii}} && (6.86)\\
&= \mathcal{S}_0, && (6.87)
\end{aligned}$$

with variance

$$\begin{aligned}
\mathrm{V}\left[\hat{\mathcal{S}}_i\right] &= \mathrm{V}\left[\frac{\Delta_i^2 - C_{nii}}{B_{ii}}\right] && (6.88)\\
&= \frac{\mathrm{V}\left[\Delta_i^2\right]}{B_{ii}^2} && (6.89)\\
&= \frac{2\left(C_{Tii}(\mathcal{S}) + C_{nii}\right)}{B_{ii}^2}, && (6.90)
\end{aligned}$$

where

$$\begin{aligned}
C(\mathcal{S}_0) &= C_T(\mathcal{S}_0) + C_n && (6.91)\\
&= \mathcal{S}_0 B + C_n && (6.92)
\end{aligned}$$

is the covariance matrix. In practice, the single band power simple quadratic estimator $\hat{\mathcal{S}}_i$ must be used as an approximation for the true band power $\mathcal{S}_0$. Above we have made use of the fact that for a Gaussian random variable x with zero mean,

$$\langle x^4 \rangle = 3(\mathrm{V}\left[x\right])^2, \tag{6.93}$$

and therefore

$$\begin{aligned} \mathrm{V}\left[x^2\right] &= \left\langle x^4 \right\rangle - \left\langle x^2 \right\rangle \left\langle x^2 \right\rangle && (6.94) \\ &= 3(\mathrm{V}\left[x\right])^2 - (\mathrm{V}\left[x\right])^2 && (6.95) \\ &= 2(\mathrm{V}\left[x\right])^2. && (6.96) \end{aligned}$$

An estimator $\hat{\mathcal{S}}_p^B$ can also be created from a linear combination of datavector elements,

$$\hat{\mathcal{S}}_p^B = \sum_i \mathrm{w}_{pi} \hat{\mathcal{S}}_i, \tag{6.97}$$

where $\mathbf{w}_p$ is a normalized weight vector. With a bit of work, it can be shown that the covariance matrix for a set of estimators $\hat{\mathcal{S}}^B$ is

$$\left\langle S_p^B S_{p'}^B \right\rangle = \sum_{ij} \mathrm{w}_{pi} \mathrm{w}_{p'j} \frac{2C_{ij}^2(\mathcal{S}_0)}{B_{ii} B_{jj}}, \tag{6.98}$$

where the covariance matrix,

$$C(\mathcal{S}) = \sum_p \mathcal{S}_p B_p + C_n \tag{6.99}$$

may be constructed using the band power estimates $\hat{\mathcal{S}}_p$ to approximate $\mathcal{S}_{0p}$. The signal and noise contributions to the total variance may be estimated by using only C_T or C_n in the above equation.

To lend intuition about how sample and noise variance contribute to the total variance, let us assume for the moment that the datavector elements are independent (no off-diagonal terms in the covariance matrix) and that B_{ii}, C_{Tii}, and C_{nii} are constant for all datavector elements. Then, for an estimator $\hat{\mathcal{S}}_p$ constructed from equal weighting of N datavector elements, the expected fractional uncertainty is

$$\begin{aligned} \frac{\left\langle \delta \hat{\mathcal{S}}_p \right\rangle}{\left\langle \hat{\mathcal{S}}_p \right\rangle} &\equiv \frac{\sqrt{\left\langle \hat{\mathcal{S}}_p \hat{\mathcal{S}}_p \right\rangle}}{\left\langle \hat{\mathcal{S}}_p \right\rangle} && (6.100) \\ &= \left(\sum_i \left(\frac{1}{N} \right) \left(\frac{1}{N} \right) \frac{2\left(C_{Tii} + C_{nii}\right)^2}{B_{ii}^2} \right)^{1/2} \times \left(\frac{C_{Tii}}{B_{ii}} \right)^{-1} && (6.101) \end{aligned}$$

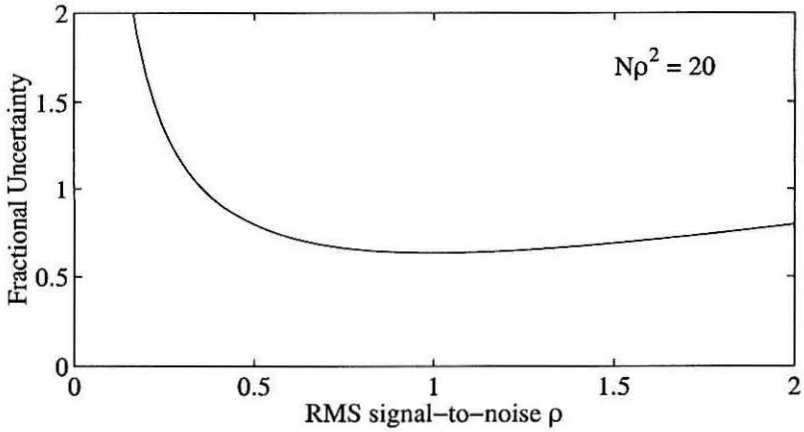

Figure 6.5 Fractional power spectrum uncertainty vs. rms signal-to-noise ratio, for fixed total observing time such that $N\rho^2 = 20$ (arbitrarily chosen). The minimum fractional uncertainty is achieved for $\rho = 1$, regardless of the total observing time.

$$= \sqrt{\frac{2}{N}}\left(1 + \frac{C_{nii}}{C_{Tii}}\right) \tag{6.102}$$

$$= \sqrt{\frac{2}{N}}\left(1 + \frac{1}{\rho_i^2}\right), \tag{6.103}$$

where, recall $\rho_i \equiv \sqrt{C_{Tii}/C_{nii}}$ [Eq. (6.76)] is the ratio of the rms signal to the rms noise for the datavector element Δ_i, and is proportional to the inverse square root of the integration time Δt. While derived using simplifying assumptions, Eq. (6.103) serves to lend intuition about the dependence of the power spectrum uncertainty on the number of independent measurements N and the integration time Δt. For a set amount of total observing time $T = N\Delta t$, Eq. (6.75) is minimized for $\rho = 1$, an rms signal-to-noise of unity. A conservative observing strategy would integrate until $\rho > 1$, since this makes the estimator in Eq. (6.81) above more robust to mis-estimates of the noise variance C_n. A plot of uncertainty vs. sample integration time is shown in Fig. 6.5.

Power spectrum error estimates calculated using the above technique return smaller uncertainties than using the maximum likelihood technique described below; this is due at least partially to the fact that the band power uncertainties reported

above assume the other band powers are fixed, rather than effectively marginalizing over them as is standard in the literature, and as we do in the maximum likelihood analysis below.

6.6 The Maximum Likelihood Estimator

For a given dataset $\mathbf{\Delta}$ and a (general) set of parameters κ that we wish to estimate, it is desirable to construct an estimator which has the minimum possible uncertainty, and for many realizations of the dataset would return, on average, the true values of the parameters. This class of estimator is called the Minimum Variance Unbiased Estimator (MVUE). The maximum likelihood (ML) estimator, defined below, is in common use because, at least in the limit of large datasets, it is a MVUE — no other unbiased estimator has smaller uncertainties. In the discussion below, we draw on Tegmark et al. (1997) for a concise review of MVUE's and the ML estimator in the analysis of CMB datasets, and Gottschalk (1995), unfortunately unpublished, which gives a precise and concise overview of statistic inference. A dense but definitive reference is Stuart et al. (1999).

The likelihood function for a given dataset and set of theoretical parameters is simply the joint PDF of the data $\mathbf{\Delta}$ given the parameters κ,

$$\mathcal{L}(\mathbf{\Delta}|\kappa) \equiv P(\mathbf{\Delta}|\kappa) \tag{6.104}$$

The Fisher information matrix (or simply Fisher matrix), a function of the likelihood function, quantifies the amount of information the dataset contains about the parameters, and is given by

$$F_{pp'} \equiv -\left\langle \frac{\partial^2 \ln \mathcal{L}}{\partial \kappa_p \partial \kappa_{p'}} \right\rangle . \tag{6.105}$$

The Fisher matrix is of fundamental importance because it is directly related to the minimum possible variance an unbiased estimator of a parameter κ can have, known

as the Cramer-Rao bound (see, e.g., Tegmark et al. 1997):

$$\mathrm{V}\left[\hat{\kappa}_p\right] \geq (F_{pp})^{-1}, \tag{6.106}$$

or, if all parameters are estimated simultaneously from the data,

$$\mathrm{V}\left[\hat{\kappa}_p\right] \geq (F^{-1})_{pp}. \tag{6.107}$$

The ML estimator asymptotically achieves the minimum possible variance in the limit of large datasets. The ML estimator for a set of parameters κ is defined to be the parameter values $\hat{\kappa}_{\mathrm{ML}}$ which maximize the likelihood function. If the data are assumed to be Gaussian distributed, the likelihood function has the form

$$\mathcal{L}(\mathbf{\Delta}|\kappa) \equiv \mathcal{L}_{\mathbf{\Delta}}(\kappa) \tag{6.108}$$

$$= \frac{1}{(2\pi)^{N/2}\left|C(\kappa)\right|^{1/2}} \exp\left(-\frac{1}{2}\mathbf{\Delta}^T C(\kappa)^{-1}\mathbf{\Delta}\right), \tag{6.109}$$

where $C(\kappa)$ is the covariance matrix of Eq. (6.99), discussed above. We write the likelihood $\mathcal{L}_{\mathbf{\Delta}}(\kappa)$ as a function of κ for one given realization of the data $\mathbf{\Delta}$. In this analysis we generally choose κ to be the band powers for a piecewise-flat power spectrum $S(u)$. In practice, however, the parameters κ can be any theoretical parameters on which the data covariance matrix depends. For example, in addition to the band powers, we can also parameterize the temperature spectral index of the fluctuations, β, where $T \propto \nu^{\beta}$.

6.7 Iterative Quadratic Estimator

In this analysis, the $N \times N$ square covariance matrix $C(\kappa)$ can have $\mathcal{O}(10^4)$ rows, even with the data compression technique described in §6.12 below. The matrix inversion C^{-1} and determinant $|C|$ operations require $\mathcal{O}(N^3)$ operations and can be time consuming to calculate. It is therefore not feasible to directly evaluate Eq. (6.109) many times, as would be required to locate κ_{ML} and characterize the likelihood surface.

6.7.1 Estimator Formalism

The iterative quadratic estimator algorithm proposed by Bond et al. (1998) cleverly finds the peak and curvature of the likelihood function with only a small number of required matrix inversions. The algorithm proceeds as follows:

1. Seed values of the parameters κ are chosen.

2. The slope and curvature of the log-likelihood function at the values κ are evaluated.

3. The likelihood function is assumed to be Gaussian with respect to the parameters κ, and the increments $\delta\kappa = \hat{\kappa}_{\rm ML} - \kappa$ required to step to the peak of the likelihood function are determined analytically from the slope and curvature of the likelihood function.

4. Because the likelihood function is not Gaussian with respect to the parameters κ, the increments $\delta\kappa$ will move the parameters closer to, but will not precisely attain, the ML value. Repeat steps 2 and 3 until $\delta\kappa = \mathbf{0}$ to within the desired precision.

Once the ML parameters $\kappa_{\rm ML}$ have been found, the curvature of the log-likelihood at the maximum likelihood values $\hat{\kappa}_{\rm ML}$ is used to estimate the uncertainty in the parameters, assuming that the likelihood function is Gaussian near its peak value. The log-likelihood function is given by

$$\ln \mathcal{L} = -\frac{1}{2}\left[N \ln(2\pi) + \ln(|C(\kappa)|) + \mathbf{\Delta}^T C(\kappa)^{-1} \mathbf{\Delta}\right]. \tag{6.110}$$

Using various matrix identities, the slope and curvature of the log-likelihood may be derived from Eq. (6.110) (Tegmark et al. 1997; Bond et al. 1998); the slope is given by

$$A_p \equiv \frac{\partial \ln \mathcal{L}(\kappa)}{\partial \kappa_p} \tag{6.111}$$

$$= \frac{1}{2}\mathrm{Tr}\left[(\mathbf{\Delta}\mathbf{\Delta}^T - C)(C^{-1}C_{,p}C^{-1})\right] \quad (6.112)$$

$$= \frac{1}{2}\mathbf{\Delta}^T C^{-1}C_{,p}C^{-1}\mathbf{\Delta} - \frac{1}{2}\mathrm{Tr}\left[C_{,p}C^{-1}\right] \quad (6.113)$$

and the curvature is given by

$$\mathcal{F}_{pp'} \equiv -\frac{\partial^2 \ln \mathcal{L}(\kappa)}{\partial\kappa_p \partial\kappa_{p'}} \quad (6.114)$$

$$= \mathrm{Tr}\left[(\mathbf{\Delta}\mathbf{\Delta}^T - C)(C^{-1}C_{,p}C^{-1}C_{,p'}C^{-1} - \frac{1}{2}C^{-1}C_{,pp'}C^{-1})\right]$$
$$+\frac{1}{2}\mathrm{Tr}\left[C^{-1}C_{,p}C^{-1}C_{,p'}\right] \quad (6.115)$$

$$= \mathbf{\Delta}^T(C^{-1}C_{,p}C^{-1}C_{,p'}C^{-1} - \frac{1}{2}C^{-1}C_{,pp'}C^{-1})\mathbf{\Delta}$$
$$-\mathrm{Tr}\left[C_{,p}C^{-1}C_{,p'}C^{-1} - \frac{1}{2}C_{,pp'}C^{-1}\right]$$
$$+\frac{1}{2}\mathrm{Tr}\left[C^{-1}C_{,p}C^{-1}C_{,p'}\right] \quad (6.116)$$

where

$$C_{,p} \equiv \frac{\partial C}{\partial \kappa_p}. \quad (6.117)$$

For parameters κ which are piecewise-flat band powers,

$$C_{,p} = B_p \quad (6.118)$$

which we have already calculated in order to assemble the theory covariance matrix C_T [Eq. (6.62)].

If the likelihood function, Eq. (6.109), is approximated as Gaussian with respect to the parameters κ, the function is completely characterized (aside from an irrelevant constant offset) by the slope vector $\mathbf{A}$ and the curvature matrix $\mathcal{F}$, and the steps $\delta\kappa = \hat{\kappa}_{\mathrm{ML}} - \kappa$ required to move to the peak of the likelihood function may be derived from the slope and curvature,

$$\delta\kappa = \mathcal{F}^{-1}\mathbf{A}. \quad (6.119)$$

The likelihood equation is in general not Gaussian with respect to κ, but successive iterations will achieve the ML values $\hat{\kappa}_{\mathrm{ML}}$, where the log-likelihood slopes $\mathbf{A}$ are zero.

Once the peak of the likelihood function is found, the inverse of the curvature matrix $\mathcal{F}$ gives the covariance matrix of the parameters, from which the uncertainties may be estimated, assuming once again that the likelihood function is Gaussian near the peak, usually a reasonably good assumption (see §6.9 for a treatment of non-Gaussian uncertainties).

As a substitute for the curvature matrix, the Fisher matrix, defined in Eq. (6.105) as the expectation value of the curvature matrix, is easier to calculate:

$$F_{pp'} = \langle \mathcal{F}_{pp'} \rangle \tag{6.120}$$

$$= \frac{1}{2}\mathrm{Tr}\left[C^{-1}C_{,p}C^{-1}C_{,p'}\right]. \tag{6.121}$$

The above equation strictly holds only for the *true* covariance matrix $C(\kappa_0)$, which is a function of parameters for which we do not have *a priori* knowledge, but substituting $C(\hat{\kappa}_{ML})$ is the best we can do, with the estimated Fisher matrix $\hat{F}$ given by

$$\hat{F}_{pp'} = \frac{1}{2}\mathrm{Tr}\left[C(\hat{\kappa}_{ML})^{-1}C_{,p}C(\hat{\kappa}_{ML})^{-1}C_{,p'}\right] \tag{6.122}$$

which should be close to F if our assumptions about the Gaussian random nature of the sky, and the properties of the instrument are accurate. The covariance matrix of the parameters κ is then estimated by

$$\hat{P}_{pp'} = (\hat{F}^{-1})_{pp'} \tag{6.123}$$

and the estimated variance on the individual estimators $\hat{\kappa}_{\mathrm{ML}p}$ is

$$\mathrm{V}\left[\hat{\kappa}_{\mathrm{ML}p}\right] \approx \hat{P}_{pp} \tag{6.124}$$

if we marginalize over all other parameters, and

$$\mathrm{V}\left[\hat{\kappa}_{\mathrm{ML}p}\right] \approx (\hat{F}_{pp})^{-1} \tag{6.125}$$

if we fix the other parameters at their ML values. The marginalized uncertainties are the ones commonly reported in the literature. Comparing Eq. (6.124) to the Cramer-Rao bound, Eq. (6.107), it can be seen that the ML estimator in principle yields the

smallest possible uncertainties on the parameters. One should be cautioned, however, that the ML estimator may be biased, especially for small datasets, and should be checked with simulations.

6.7.2 Single Iteration Example

To understand how the ML iterative quadratic estimator is related to the simple quadratic estimator discussed in §6.5, we can explore the simple case of a single band power $\mathcal{S}_p$, with a diagonal covariance matrix C. We start with a seed value $\mathcal{S}_p = \mathcal{S}_p^0$. Then,

$$C(\mathcal{S}_p^0) = C_T(\mathcal{S}_p^0) + C_n \tag{6.126}$$

$$= \mathcal{S}_p^0 B_p + C_n, \tag{6.127}$$

which is assumed to be diagonal. The slope of the log-likelihood function, Eq. (6.113), becomes

$$A_p = \sum_i \left[(\Delta_i^2 - C_{ii})(C_{ii}^{-2} B_{p_{ii}})\right], \tag{6.128}$$

and the Fisher matrix, Eq. (6.121), becomes

$$F_{pp} = \frac{1}{2} \sum_i \left[C_{ii}^{-2} B_{p_{ii}}^2\right], \tag{6.129}$$

so that, using Eq. (6.119),

$$\delta\mathcal{S}_p = \frac{\sum_i \left[(\Delta_i^2 - C_{ii})(C_{ii}^{-2} B_{p_{ii}})\right]}{\sum_i \left[C_{ii}^{-2} B_{p_{ii}}^2\right]} \tag{6.130}$$

$$= \sum_i \mathrm{w}_i \frac{(\Delta_i^2 - C_{ii})}{B_{p_{ii}}} \tag{6.131}$$

$$= \sum_i \mathrm{w}_i \frac{\left[\Delta_i^2 - (\mathcal{S}_p^0 B_{p_{ii}} + C_{n_{ii}})\right]}{B_{p_{ii}}} \tag{6.132}$$

$$= \sum_i \mathrm{w}_i \frac{(\Delta_i^2 - C_{n_{ii}})}{B_{p_{ii}}} - \mathcal{S}_p^0 \tag{6.133}$$

where

$$\mathrm{w}_i = \frac{C_{ii}^{-2} B_{p_{ii}}^2}{\sum_i \left[C_{ii}^{-2} B_{p_{ii}}^2\right]} \tag{6.134}$$

$$= \frac{(\mathcal{S}_p^0 + C_{nii}/B_{p_{ii}})^{-2}}{\sum_i (\mathcal{S}_p^0 + C_{nii}/B_{p_{ii}})^{-2}} \tag{6.135}$$

can be interpreted to be a normalized weight matrix. The single iteration band-power estimator is

$$\hat{\mathcal{S}}_p = \mathcal{S}_p^0 + \delta\mathcal{S}_p \tag{6.136}$$

$$= \sum_i \mathrm{w}_i \frac{(\Delta_i^2 - C_{nii})}{B_{p_{ii}}}, \tag{6.137}$$

and the Fisher matrix estimator is

$$\hat{F}_{pp} = \frac{1}{2} \sum_i \frac{B_{p_{ii}}^2}{\left(\hat{\mathcal{S}}_p B_{p_{ii}} + C_{nii}\right)^2} \tag{6.138}$$

$$= \frac{1}{2} \sum_i \left(\hat{\mathcal{S}}_p + \frac{C_{nii}}{B_{p_{ii}}}\right)^{-2}. \tag{6.139}$$

Equations (6.137) and (6.139) are directly comparable to Eqs. (6.97) and (6.103) for the simple quadratic estimator, with weight vector elements inversely proportional to the expected total variance (signal and noise) of the seed band-power value $\mathcal{S}_p^0$. Recalling Eq. (6.96), w_i is minimum variance weighting in the estimation of a band power which is itself a variance.

6.8 Constraint Matrix Formalism

To reduce near-field ground contamination and point source contributions to the power spectrum, we employ the constraint matrix formalism described in Bond et al. (1998) to marginalize over potentially contaminated modes in the data. We do not subtract ground components or point sources from the data. Instead we render the analysis insensitive to these modes in the data using the method described below.

If some contamination is present in the data, we represent it by adding a component to the signal and noise components of the idealized datavector [Eq. (6.35)],

$$\mathbf{\Delta} = \mathbf{s} + \mathbf{n} + \sum_q \alpha_q \mathbf{T}_q \tag{6.140}$$

where a contaminated mode q is described by a shape vector $\mathbf{T}_q$, with the same size as the datavector $\mathbf{\Delta}$, and α_q is a random variable representing the amplitude of the mode. The covariance matrix of this datavector is then

$$\begin{aligned} C &= \left\langle \mathbf{\Delta}\mathbf{\Delta}^T \right\rangle - \left\langle \mathbf{\Delta} \right\rangle \left\langle \mathbf{\Delta}^T \right\rangle & (6.141)\\ &= C_T + C_n + \sum_{qq'} \left[\left\langle \alpha_q \alpha_{q'} \right\rangle - \left\langle \alpha_q \right\rangle \left\langle \alpha_{q'} \right\rangle \right] \mathbf{T}_q \mathbf{T}_q^T & (6.142)\\ &= C_T + C_n + C_C & (6.143) \end{aligned}$$

where

$$C_C \equiv \sum_{qq'} \left[\left\langle \alpha_q \alpha_{q'} \right\rangle - \left\langle \alpha_q \right\rangle \left\langle \alpha_{q'} \right\rangle \right] \mathbf{T}_q \mathbf{T}_q^T \tag{6.144}$$

is the constraint matrix, and we have assumed that $\mathbf{s}$ and $\mathbf{n}$ are uncorrelated with all α_q. The shape vector $\mathbf{T}_q$ of the potentially contaminated mode can be well defined while we may have no *a priori* knowledge about the amplitude α_q. We may express this lack of knowledge by treating the amplitude α_q as a random variable with zero mean, and variance which is very large compared to the expected signal and noise. Then,

$$C_C = \sum_{qq'} \left\langle \alpha_q \alpha_{q'} \right\rangle \mathbf{T}_q \mathbf{T}_q^T \tag{6.145}$$

or

$$C_C = \sum_q \left\langle \alpha_q^2 \right\rangle \mathbf{T}_q \mathbf{T}_q^T \tag{6.146}$$

if the modes are uncorrelated. Inflating the variance of α_q has the effect of de-weighting the mode $\mathbf{T}_q$ in the data. In practice, we insert for the variance $\left\langle \alpha_q^2 \right\rangle$ a number large enough to de-weight the undesired mode without causing the covariance matrix to become poorly conditioned (or, in the extreme case, singular). This is equivalent to marginalizing over the unknown coefficients α_q.

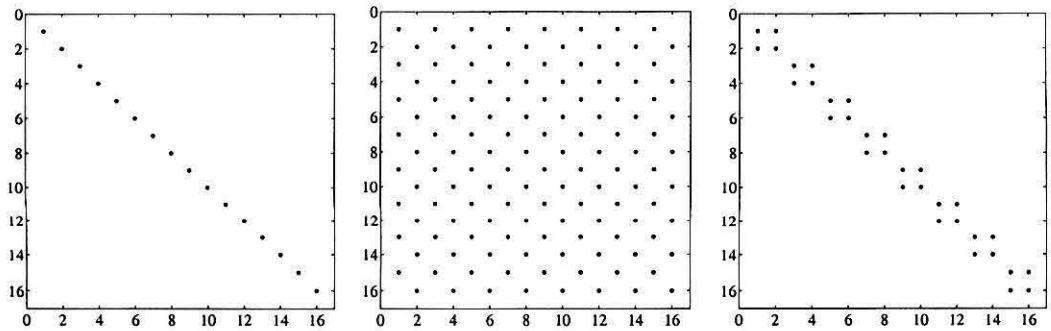

Figure 6.6 Sample of the noise and constraint matrices for a subspace of the datavector consisting of two visibilities observed in each of 8 fields. The datavector order is: {vis a field 1, vis b field 1, vis a field 2, ..., vis b field 8}. The left panel depicts the non-zero elements of the diagonal noise covariance matrix, without constraints. The center panel depicts two co-added constraint matrices, constraining a common component across 8 fields for each of the 2 visibilities. The right panel depicts 8 co-added constraint matrices, constraining a foreground template (such as dust, or point sources of known position), one template for each of the 8 fields.

For example, in the sub-space of the datavector consisting of a single visibility observed in 8 fields, a template vector $\mathbf{T}_q = [1\ 1\ 1\ 1\ 1\ 1\ 1\ 1\ ]^T$ is used to constrain a common mode with the same amplitude in all 8 fields. Any mode in the data which can be described as a relative amplitude between data vector elements, as in the example above, can be constrained. We use this method to eliminate near-field ground contamination in the field rows, and contributions from point sources with known positions. For each point source we also use constraint matrices to marginalize over arbitrary spectral indices, which we approximate as an amplitude slope across the ten frequency bands. Sample constraint matrices are shown in Fig. 6.6, and a sample image of a dust map and the corresponding DASI visibility template are shown in Fig. 6.7. This constraint matrix formalism has proven to be an extremely powerful tool for removing potentially contaminated components from the data, since it requires no knowledge of the contaminant amplitude, only its shape in the datavector.

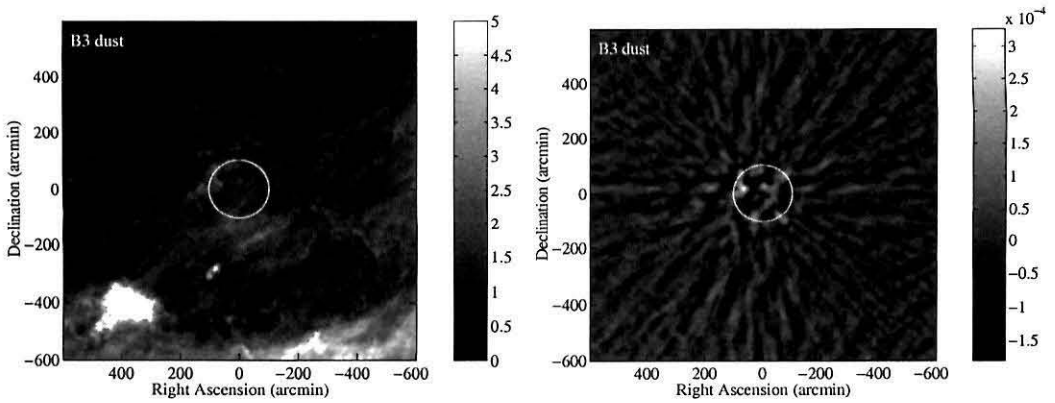

Figure 6.7 Sample dust map and dust template for one of the DASI fields (B3). The left panel is an image from the cleaned IRAS 100 μm survey map of Finkbeiner et al. (1999), projected in orthographic coordinates centered on DASI field B3. The right panel is a synthesized image made from a simulated observation by DASI of the image in the left panel. The (noiseless) simulated visibility data are made into a template vector, which is used to constrain a possible foreground component in the DASI data which fits the shape of the template. Color bar units of brightness are arbitrary, but the same in the left and right panels.

6.9 Non-Gaussian Uncertainties

Using the Fisher matrix to estimate uncertainties in the ML estimators $\hat{\kappa}_{\rm ML}$, as in Eqs. (6.124) and (6.125), assumes that the likelihood function is Gaussian in the parameters κ in the vicinity of $\hat{\kappa}_{\rm ML}$,

$$\mathcal{L}(\kappa) \propto e^{-\frac{1}{2}(\kappa-\hat{\kappa}_{\rm ML})^T P^{-1}(\kappa-\hat{\kappa}_{\rm ML})} \tag{6.147}$$

where $P = F^{-1}$ is the covariance matrix for the parameters κ, and is not itself dependent on κ. However, in our previous simple example assuming a diagonal covariance matrix, the estimated Fisher matrix, Eq. (6.139) is dependent on the band power estimate $\hat{\mathcal{S}}$. As is pointed out by Bond et al. (2000), this is an indication that the likelihood function is *not* Gaussian in the band power parameters $\mathcal{S}$, and has some bias.

It turns out that the ML estimator is, in general, biased. This is a consequence of the fact that it is parameter invariant (Gottschalk 1995). If $\gamma(\kappa)$ are some different

set of parameters which are a function of the parameters κ, then

$$\frac{\partial \mathcal{L}}{\partial \kappa_p} = \sum_q \left(\frac{\partial \mathcal{L}}{\partial \gamma_q}\right)\left(\frac{\partial \gamma_q}{\partial \kappa_p}\right) \tag{6.148}$$

which implies that

$$\hat{\gamma}_{\rm ML} = \gamma(\hat{\kappa}_{\rm ML}) \tag{6.149}$$

assuming $\partial\gamma_q/\partial\kappa_p \neq 0$. If $\gamma(\kappa)$ is a non-linear function, it follows that either $\kappa_{\rm ML}$ or $\gamma_{\rm ML}$ is biased, since

$$\langle \gamma\left(\hat{\kappa}_{\rm ML}\right)\rangle \neq \gamma\left(\langle\hat{\kappa}_{\rm ML}\rangle\right). \tag{6.150}$$

The well-known solution (Gottschalk 1995) is to exploit the parameterization invariance of the ML estimator to refine the uncertainty estimates of Eqs. (6.124) and (6.125) by finding a set of parameter estimators $\gamma(\hat{\kappa}_{\rm ML})$ which are Gaussian distributed. Bounds on a given confidence region in the Gaussian parameters,

$$\hat{\gamma}_N^{\pm} \equiv \hat{\gamma}_{\rm ML} \pm N\sigma_\gamma \tag{6.151}$$

where $\sigma_\gamma = \sqrt{\mathrm{V}\left[\hat{\gamma}_{\rm ML}\right]}$ are the 1-σ uncertainties in γ, can then be associated with bounds on the confidence region in κ

$$\hat{\kappa}_N^{\pm} = \kappa(\hat{\gamma}_{\rm ML} \pm N\sigma_\gamma), \tag{6.152}$$

assuming $\gamma(\kappa)$ is well behaved and invertible, with a possible change in sign depending on the form of the function. This is valid since parameterization invariance guarantees that the likelihood function will be the same fraction of its ML value, regardless of the change of parameters.

Bond et al. (2000) propose a change in parameters based on the functional form of the uncertainty under the assumption of an ideal all-sky experiment with uniform pixel noise. We find the same functional form in the analysis of interferometry data if we make the analogous simplifying assumptions for a power spectrum estimator $\hat{\mathcal{S}}$ in discrete bands: a diagonal covariance matrix (as was assumed in the example in §6.7.2), uniform noise, and a piece-wise flat power spectrum. The estimated

uncertainty becomes, using Eqs. (6.139) and (6.124),

$$\hat{\sigma}_{\hat{\mathcal{S}}_p} = \sqrt{\frac{2}{N}} \left(\hat{\mathcal{S}}_p + \frac{C_n}{B_p} \right) \tag{6.153}$$

[similar to Eq. (6.103) above]. Bond et al. (2000) suggest the change of parameters,

$$\gamma_p = \ln(\mathcal{S}_p + x_p) \tag{6.154}$$

where

$$x_p = \frac{C_n}{B_p} \tag{6.155}$$

is an estimate of the contribution of noise to the total uncertainty. The covariance matrix for the new parameters is then

$$P^{\gamma}_{pp'} = \sum_{qq'} \frac{\partial \gamma_p}{\partial \mathcal{S}_q} P^{\mathcal{S}}_{qq'} \frac{\partial \gamma_{p'}}{\partial \mathcal{S}_{q'}} \tag{6.156}$$

$$= (\mathcal{S}_p + x_p)^{-1} P^{\mathcal{S}}_{pp'} (\mathcal{S}_{p'} + x_{p'})^{-1}, \tag{6.157}$$

or equivalently,

$$F^{\gamma}_{pp'} = (\mathcal{S}_p + x_p) F^{\mathcal{S}}_{pp'} (\mathcal{S}_{p'} + x_{p'}), \tag{6.158}$$

where $P^{\mathcal{S}} = (F^{\mathcal{S}})^{-1}$, $P^{\gamma} = (F^{\gamma})^{-1}$ are the covariance matrices of parameters $\mathcal{S}$ and γ, respectively. The ratio $\mathcal{S}_p/x_p$ is ratio of the signal and noise contributions to the uncertainty in Eq. (6.153), and may be estimated by using Eq. (6.121) to calculate the ratio of the Fisher matrix without signal to the Fisher matrix without noise,

$$\frac{\mathcal{S}_p}{x_p} = \sqrt{\frac{F_N}{F_T}} \tag{6.159}$$

where

$$F_N = \frac{1}{2} \mathrm{Tr} \left[C_N^{-1} C_{,p} C^{-1} C_{N,p'} \right], \tag{6.160}$$

and

$$F_T = \frac{1}{2} \mathrm{Tr} \left[C_T^{-1} C_{,p} C^{-1} C_{T,p'} \right]. \tag{6.161}$$

Alternatively,

$$\frac{\mathcal{S}_p}{x_p} \approx \sqrt{\frac{F_N}{F}} - 1, \tag{6.162}$$

where F is the full Fisher matrix of Eq. (6.121) (Bond et al. 2000). Although Eq. (6.162) only holds in the case of a diagonal covariance matrix with uniform noise and a flat power spectrum $\mathcal{S}(u)$, we make these same assumptions to determine the functional form of the uncertainty and the appropriate change of variables. In practice we have found that calculating both F_N and F_T is not difficult, but for the DASI data we use Eq. (6.162) to calculate x_p since the calculation of F_T requires extra time.

Although a real experiment such as DASI does not obey the simplifying assumptions outlined above, Bond et al. (2000) find that this change of parameters, which they call the offset log-normal formalism, works well for a variety of small datasets for which they were able to compare the results to the true likelihood surface. It has become the standard method in the CMB community for estimating non-Gaussian uncertainties.

6.10 Band-Power Window Functions

Window functions, as given in Eqs. (6.43) and (6.44), have been used in the literature to describe experimental sensitivity as a function of multipole moment l (see, e.g., Coble et al. 1999). Knox (1999) points out that these variance window functions, which are used to calculate the signal contribution to the data variance, are not necessarily appropriate for calculating the expectation value of measured band powers given an underlying power spectrum. Such a function, which Knox (1999) calls the *band-power window function*, is needed to compare theory and measurement when extracting cosmological parameters (see §6.11).

The band-power window function W^B translates the underlying theoretical power spectrum C_l into an expectation value for the band power measurement:

$$\left\langle \hat{C}_p \right\rangle = \sum_l \frac{W^B_{pl}}{l} C_l, \tag{6.163}$$

or in terms of the estimators $\hat{\mathcal{S}}$ which measure band-powers $\mathcal{S}(u)$,

$$\left\langle \hat{\mathcal{S}}_p \right\rangle = \int_0^\infty \mathrm{d}u \, \frac{\mathcal{W}_p^B(u)}{u} \, \mathcal{S}(u). \tag{6.164}$$

Following the derivation of the band-power window function in Knox (1999), we require a simple quadratic expression for the band-power estimators $\hat{\mathcal{S}}_{\mathrm{ML}}$, for which we use simply the first iteration of the quadratic estimator introduced in §6.7 above. In practice, the first iteration estimator is close to the ML estimator, and is in fact a MVUE (Bond et al. 1998; Tegmark 1997). This band-power estimator for band p, which we call $\hat{\mathcal{S}}_p^Q$, is calculated using Eqs. (6.119), (6.116), and (6.113), starting with a seed value $\mathcal{S}_p^0$:

$$\hat{\mathcal{S}}_p^Q = \mathcal{S}_p^0 + \delta\mathcal{S}_p \tag{6.165}$$

$$= \frac{1}{2} \sum_{p'} \left(F^{-1}\right)_{pp'} \mathrm{Tr}\left[\left(\boldsymbol{\Delta}^T \boldsymbol{\Delta} - C_N\right) C^{-1} C_{T,p} C^{-1}\right], \tag{6.166}$$

where we have left the intervening steps, generalized from the simple example in §6.7.2, as an exercise for the reader. Now, if we break each band p into sub-bands q, sufficiently fine that we can assume $\mathcal{S}(u)$ is constant within each sub-band, then

$$C_{T,p} = \sum_{q \in p} C_{T,q} \tag{6.167}$$

and

$$F_{pp'} = \frac{1}{2} \mathrm{Tr}\left[C^{-1} \sum_{q \in p} C_{T,q} C^{-1} \sum_{q' \in p'} C_{T,q'}\right] \tag{6.168}$$

$$= \sum_{q \in p} \sum_{q' \in p'} F_{qq'}. \tag{6.169}$$

Then,

$$\left\langle \hat{\mathcal{S}}_p^Q \right\rangle = \frac{1}{2} \sum_{p'} \left(F^{-1}\right)_{pp'} \mathrm{Tr}\left[\sum_q \mathcal{S}_0(u_q) C_{T,q} C^{-1} \sum_{q' \in p'} C_{T,q'} C^{-1}\right] \tag{6.170}$$

$$= \sum_{p'} \left(F^{-1}\right)_{pp'} \sum_q \mathcal{S}_0(u_q) \sum_{q' \in p'} F_{qq'} \tag{6.171}$$

$$= \sum_q \mathcal{S}_0(u_q) \sum_{p'} \left(F^{-1}\right)_{pp'} \sum_{q' \in p'} F_{qq'}, \tag{6.172}$$

and comparing with Eq. (6.164), we find

$$\frac{\mathcal{W}^B(u_q)}{u_q} = \frac{1}{\Delta u_q} \sum_{p'} \left(F^{-1}\right)_{pp'} \sum_{q' \in p'} F_{qq'} \tag{6.173}$$

where Δu_q is the width of band q or, equivalently, for C_l [Eq. (6.163)],

$$\frac{W^B_{l_q}}{l_q} = \sum_{p'} \left(F^{-1}\right)_{pp'} \sum_{q' \in p'} F_{qq'}. \tag{6.174}$$

The above equations generalize the result given in Knox (1999) for a Fisher matrix with significant off-diagonal elements. Note that the band-power window functions are normalized, with a sum of unity. In practice, for the ML band-power estimators, we start with the estimator values $\hat{\mathcal{S}}_{\rm ML}$, calculate the Fisher matrix in four sub-bands, and interpolate to find the window functions for all u or l. The band-power window functions for the nine bands chosen for the DASI power spectrum analysis are shown in Fig. 6.8. Unlike the variance window functions, shown in Fig. 6.4, the band-power window functions are non-zero over the entire range in l to which DASI is sensitive. This reflects the correlations between the different bands in the ML estimator.

6.11 Cosmological Parameter Estimation

In addition to estimating the angular power spectrum, we would like to estimate the values of cosmological parameters such as the baryon density Ω_b, the cold dark matter density Ω_{cdm}, the vacuum density Ω_Λ, and others. This can be done provided that we can construct a theoretical power spectrum given a set of cosmological parameter values. In large part, the present motivation for measuring the CMB angular power spectrum is driven by the fact that the cosmology community has, in the past decade, converged upon precision predictions for the theoretical angular power spectrum given a set of cosmological parameters. For the past several years, numerical algorithms such as `cmbfast` (Zaldarriaga & Seljak 2000) have been made freely available to the community, and can generate theoretical power spectra in a matter of seconds. A grid

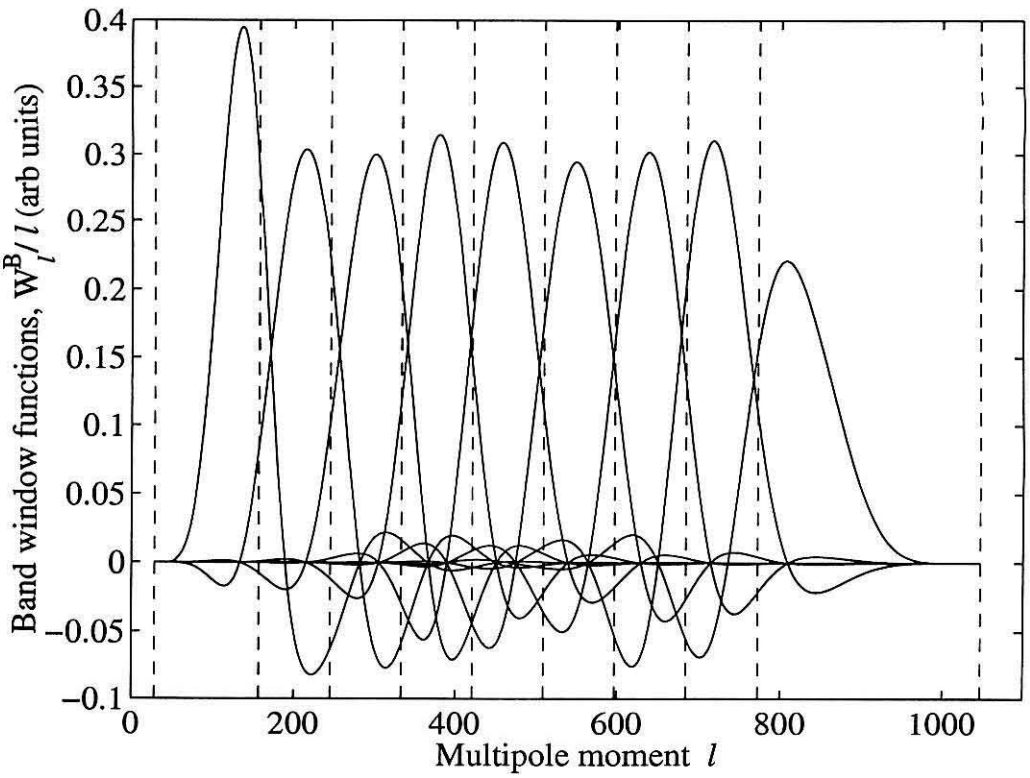

Figure 6.8 Band-power window functions for the nine DASI power spectrum bands (solid lines). Dashed lines indicate the boundaries of the piecewise-flat bands for which the band-powers are estimated. Unlike the variance window functions, the band-power window functions are non-zero over the entire range in l to which DASI is sensitive. This reflects the correlations between the different bands in the ML estimator.

of such theoretical models can be used to place constraints on cosmological parameters given a measured angular power spectrum.

The maximum likelihood (ML) estimator can be used to estimate the cosmological parameters. Using the band-power window functions, Eq. (6.163), to generate expectation values for band-power ML estimators $\hat{\mathcal{S}}_{\rm ML}$ given a theoretical power spectrum, the likelihood function for the expectation values $\left\langle \hat{\mathcal{S}}_{\rm ML} \right\rangle$ is given by

$$\mathcal{L}_{\hat{\mathcal{S}}_{\rm ML}}\left(\left\langle \hat{\mathcal{S}}_{\rm ML} \right\rangle\right) = \frac{1}{(2\pi)^{M/2}\,|P|^{1/2}} e^{-\frac{1}{2}\left(\hat{\mathcal{S}}_{\rm ML}-\left\langle \hat{\mathcal{S}}_{\rm ML} \right\rangle\right)^T P^{-1}\left(\hat{\mathcal{S}}_{\rm ML}-\left\langle \hat{\mathcal{S}}_{\rm ML} \right\rangle\right)}, \qquad (6.175)$$

where M is the number of band-powers. Since the likelihood function is assumed to

be Gaussian in the parameters $\left\langle \hat{\mathcal{S}}_{\rm ML} \right\rangle$, the covariance matrix P is not dependent on $\left\langle \hat{\mathcal{S}}_{\rm ML} \right\rangle$, and maximizing the likelihood function is equivalent to minimizing χ^2,

$$\chi^2 \left(\left\langle \hat{\mathcal{S}}_{\rm ML} \right\rangle \right) = \left(\hat{\mathcal{S}}_{\rm ML} - \left\langle \hat{\mathcal{S}}_{\rm ML} \right\rangle \right)^T P^{-1} \left(\hat{\mathcal{S}}_{\rm ML} - \left\langle \hat{\mathcal{S}}_{\rm ML} \right\rangle \right) \tag{6.176}$$

where we use the inverse of the estimated Fisher matrix, $\hat{F}^{-1}$ for the parameter covariance matrix P.

An overall calibration uncertainty, or a beam uncertainty, is not taken into account in our estimate of the Fisher matrix in §6.7. These uncertainties are usually reported separately in the literature, and must be taken into account when estimating cosmological parameters. If we have a multiplicative uncertainty, completely correlated between all band-powers, with relative weights, or shape, given by the vector $\mathbf{b}$, the band-power estimates are scaled

$$\hat{\mathcal{S}}_p = \hat{\mathcal{S}}^0_p (1 + \alpha \mathrm{b}_p) \tag{6.177}$$

where $\hat{\mathcal{S}}^0$ is the estimator without calibration uncertainty and α is a calibration uncertainty random variable with zero mean. The resulting covariance matrix is

$$\begin{aligned} P_{pp'} &= P^0_{pp'} + \left\langle \alpha^2 \right\rangle \left\langle \hat{\mathcal{S}}^0_p \hat{\mathcal{S}}^0_{p'} \right\rangle \mathrm{b}_p \mathrm{b}_{p'} & (6.178) \\ &\approx P^0_{pp'} + \left\langle \alpha^2 \right\rangle \hat{\mathcal{S}}_p \hat{\mathcal{S}}_{p'} \mathrm{b}_p \mathrm{b}_{p'} & (6.179) \end{aligned}$$

where P^0 is the covariance estimate given by $\hat{F}^{-1}$.

The change of variable introduced in §6.9 may be used to correct for the non-Gaussian shape of the likelihood function, manifested here as a dependence of P on the parameters $\mathcal{S}$. The change of variables is

$$\begin{aligned} \gamma^d_p &= \ln \left(\hat{\mathcal{S}}_{{\rm ML}p} + x_p \right) & (6.180) \\ \gamma^t_p &= \ln \left(\left\langle \hat{\mathcal{S}}_{{\rm ML}p} \right\rangle + x_p \right) & (6.181) \\ P^\gamma_{pp'} &= \left(\hat{\mathcal{S}}_{{\rm ML}p} + x_p \right)^{-1} P \left(\hat{\mathcal{S}}_{{\rm ML}p'} + x_{p'} \right)^{-1} & (6.182) \end{aligned}$$

and the χ^2 statistic is calculated as above,

$$\chi^2 \left(\gamma^t \right) = \left(\gamma^d - \gamma^t \right)^T \left(P^\gamma \right)^{-1} \left(\gamma^d - \gamma^t \right)^T . \tag{6.183}$$

Note that this χ^2 statistic is not rigorous; that is, even assuming γ_p^t is derived from the "true" underlying model, $\gamma_p^t \neq \langle \gamma_p^d \rangle$ in general. This follows from the bias argument, Eq. (6.150). Bond et al. (2000) take this χ^2 statistic, Eq. (6.183), as an ansatz, and show empirically that it works well for various datasets. We adopt this equation for our cosmological parameter estimation, the results of which are summarized in Chapter 8.

6.12 Likelihood Analysis Implementation

The author has written an analysis package called `dasipower` to implement the maximum likelihood estimator for piece-wise flat band-powers described above. Three general steps are required: preparation of the visibility datavector, calculation of the theory and noise covariance matrix elements, and iterating the maximum likelihood quadratic estimator of Bond et al. (1998), described in §6.7. The two-dimensional integrations required to calculate the theory covariance matrix elements are executed by code written in C; the datavector manipulations and iterated quadratic estimator are implemented in `matlab`, which is well suited to the required matrix manipulations. The package takes as input calibrated visibilities, averaged in 1-hr integrations, and other associated data. The data reduction package required to bin and calibrate the raw 8-s integrated visibilities, called `dasi`, was written by a colleague, E. Leitch.

Calculation of the theory covariance matrix elements is performed using the program `covtheory`, written by the author in C. The program calculates matrix elements $B_{p_{ij}}$ by performing the overlap integral of the autocorrelation functions in band p using a simple iterative two-dimensional Reimann sum. The rectangular limits of integration are chosen to bound closely the overlap area, which in general is an irregular shape bounded by arcs (Fig. 6.9). We use an analytical expression for the theoretical aperture field distribution, Eqs. (3.9) and (3.10), which closely matches the actual horn performance (see §3.4.2). The two-dimensional autocorrelation function $\widetilde{A}(\mathbf{u}, \nu)$, shown in Fig. 6.2, is radially symmetric; it is evaluated numerically at ~ 50 points

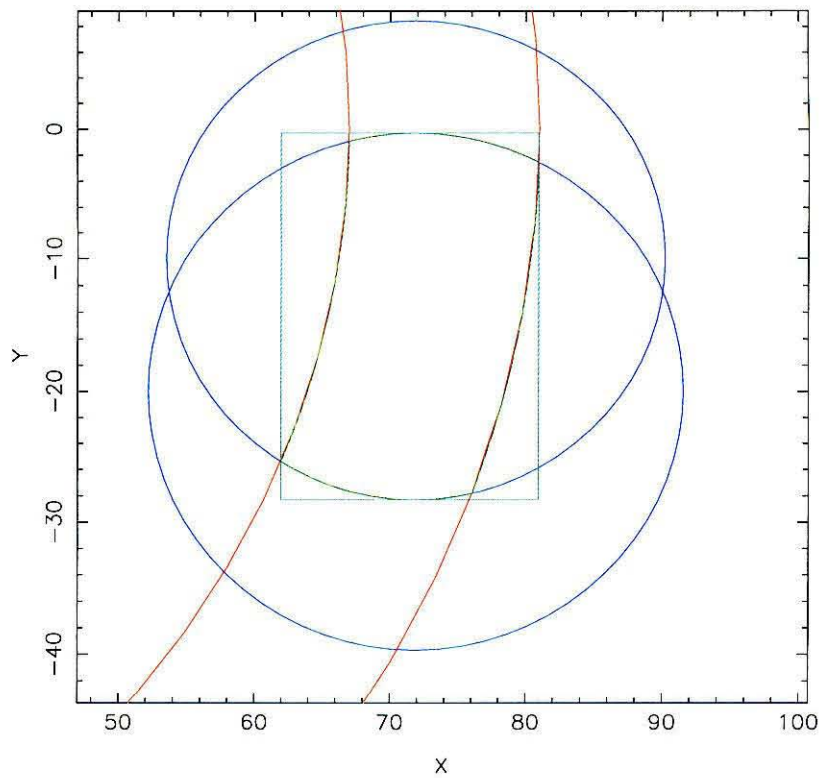

Figure 6.9 Sample area of integration for a theory covariance matrix element, $B_{p_{ij}}$. The overlapping circles represent the outer limits of the autocorrelation functions for the visibilities i and j; the circles have different radii since the observing frequencies ν_i and ν_j differ for the sample element. The concentric arcs represent the lower and upper limits of the band, u_{l_p} and u_{h_p}. The rectangular box is the area over which the numerical integration is performed.

in radius and stored in a lookup table. The program takes as input the filename of a tab-delimited table with rows u, v, ν of (u, v) coordinates and frequencies, and the lower and upper (u, v) radii of the band p. Three additional optional input arguments $\alpha_2 - \alpha_1, \delta_1, \delta_2$ specify the separation in degrees RA and DEC of two fields if interfield covariance elements are desired. The output is a 4-column table $i, j, B_{ij}^{R/R}, B_{ij}^{I/I}$, with an additional two columns $B_{ij}^{R/I}, B_{ij}^{I/R}$ if interfield covariance matrix elements are being evaluated, since the R/I and I/R correlations are in general non-zero. The theory covariance matrix for a single field is shown in Fig. 6.10.

We assume that the noise covariance matrix of the combined visibility data vector

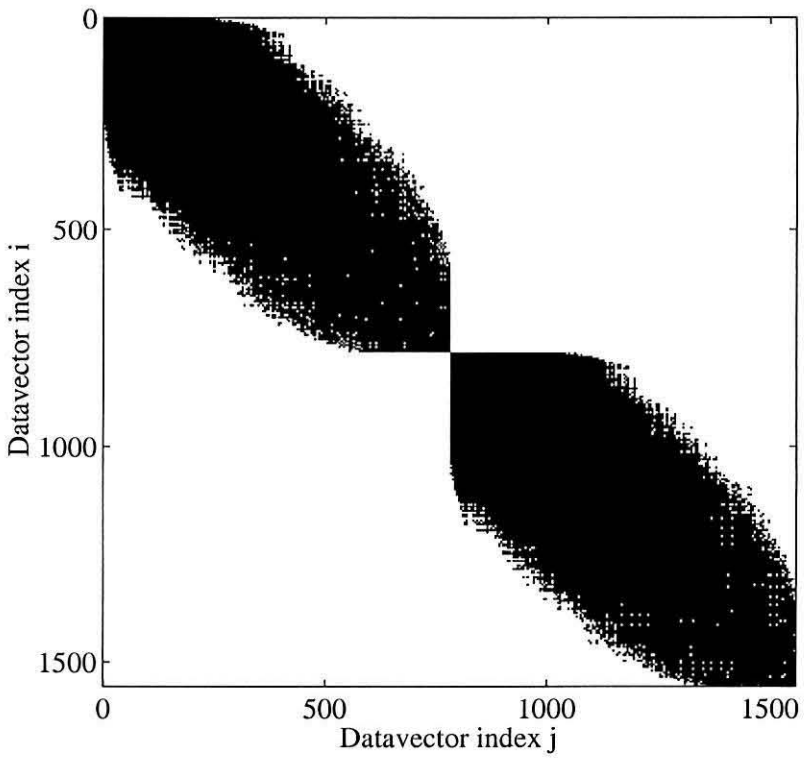

Figure 6.10 Theory covariance matrix non-zero elements for a single field. The upper and lower block diagonal elements are the real and imaginary covariance matrices, $C_{Tij}^{R/R}$ and $C_{Tij}^{I/I}$, respectively. In this plot, visibilities are sorted by (u, v) radius within each of the two blocks. The matrix is 11% filled, and band diagonal, which may be taken advantage of to make matrix inversion faster. However, interfield correlations and the addition of a constraint matrix, discussed in §6.8, add non-zero elements and break the band-diagonal form, slowing inversion.

is diagonal, with elements $C_{nii} = \sigma_{ii}^2$ estimated from the sample variance in the 8.4-s integrations over the 1-hr observations. To verify the assumption that C_n is diagonal, we have calculated the sample covariance matrix from the data in each of the ten frequency channels for all 1-hr observations. We find rare occasions where the visibilities are strongly correlated due to atmospheric fluctuations. Our weather edits, described in Chapter 5, consist of cuts based on the strength of these correlations; we cut observations in which the correlation coefficient exceeds 0.36, but the data consistency does not depend strongly on this value. Consistency tests, discussed in

§7.4, show that this simple noise model is surprisingly accurate.

In our implementation of the ML iterated quadratic estimator of Bond et al. (1998), we calculate the quantities $C^{-1}C_{,p}$ and $C^{-1}\Delta$, and use these to calculate the log-likelihood slope A, Eq. (6.113), and the Fisher matrix F, Eq. (6.121). Typically, only three iterations are needed to converge upon $\mathcal{S}_{\rm ML}$ to within 1%. Because the four sets of 8 fields have independent signal and noise, the covariance matrix is block diagonal by field row, which allows us to manipulate the datavector and covariance sub-matrices for the four field rows separately. The datavector for a single field row consists initially of $156 \times 10 \times 8 \times M = 12,480M$ elements, where 156 is the number of real and imaginary visibilities per band, 10 is the number of frequency bands, 8 is the number of fields, and M is the number of 1-hr observations of the field row, which ranges from 28 for the A row to 62 for the D row. Various cuts, described in Chapter 5, are performed, and the observations are combined, resulting in a combined datavector length $< 12,480$. The covariance matrix for a datavector of this length is quite cumbersome, occupying ~ 1.2 GB of memory, assuming a filled matrix of double-precision floating point numbers, and takes about three hours to invert on an Intel[1] Pentium III 800 MHz CPU running Matlab[2] version 5, the CPU and matrix manipulation software used for the analysis. For each field row, the matrix $C^{-1}C_{,p}$ must be calculated for p band powers, and typically three iterations (this is significantly faster than calculating C^{-1} once and doing matrix multiplications for each $C_{,p}$), making the analysis prohibitively time consuming. Since the number of operations required to invert a matrix of dimension N scales as $\mathcal{O}(N^3)$, reducing the dimension of the matrix by a factor of two results in an order of magnitude reduction in time required for the analysis. We therefore compress the datavector by combining visibilities from adjacent frequency bands, which are nearby in the (u, v) plane and

[1]Intel Corp., 2200 Mission College Blvd., Santa Clara, CA 95052-8119.
[2]The MathWorks, Inc., 3 Apple Hill Drive, Natick, MA 01760-2098.

are therefore highly correlated. The combined datavector element is given by

$$\Delta_i = \frac{\sum_l \mathrm{w}_{il}\Delta_{il}}{\sum_l \mathrm{w}_{il}} \tag{6.184}$$

where Δ_{il} is the datavector for band l in baseline i, and w_{il} is a weight vector. Then the covariance matrix element for the combined datavector elements i and j is

$$C_{ij} = \frac{\sum_{lm} \mathrm{w}_{il}\mathrm{w}_{jm}C_{il,jm}}{\sum_{lm} \mathrm{w}_{il}\mathrm{w}_{jm}}. \tag{6.185}$$

Looking at Eq. (6.185) above as applied to the theory and noise covariance matrices, we can see that if we combine two completely uncorrelated visibilities (say from points far apart in the (u,v) plane) with equal weight, we will lose a factor of $\sqrt{2}$ in sensitivity, defined above as $\sqrt{C_{Tii}/C_{nii}}$, compared with combining completely correlated visibilities. This represents a loss of information in compressing the data which we wish to minimize. The effect of compression on the power spectrum uncertainties can be assessed using simulated data. In practice, we are able to compress the field row datavector length to $\sim$ 4200 elements with negligible effect on the uncertainties. An analysis consisting of three iterations on nine band-powers at this compression level takes about two days, with each field row processed in parallel on a separate CPU. For all but the final analysis run, we compress the field row datavector to $\sim$ 2600 elements, allowing a complete analysis in roughly ten hours using two dual-CPU machines.

The constraint matrix formalism discussed in §6.8 has proven to be an extremely powerful tool for effectively removing contaminating effects in the data, ranging from a ground signal component to point sources and possible diffuse foregrounds. Specific modes removed from the data are discussed in Chapter 7. The resulting power spectrum is robust against the choice of large variance inserted as the pre-constant for the constraint matrix in Eq. (6.146); the pre-constant may range over at least seven orders of magnitude from the lower value at which it becomes effective to the upper value at which the covariance matrix becomes poorly conditioned.

A limitation of the constraint matrix formalism is that, in order to preserve the "shape" of the constraint template vector, data must be combined with uniform

weighting. Thus, in constraining a common ground component between 8 fields, the N observations must all be combined with equal weight (rather than, say, weighting by the inverse variance). When using data compression, as discussed above, a different problem results from failure to use uniform weighting — the resulting compressed ground constraint matrices preserve their uncompressed rank, i.e., they constrain the same number of degrees of freedom as the uncompressed constraint matrices, as they must to keep track of the change in "shape" of the various ground constraints when they are added with different weights. The result is that the compressed datavector can (and has, much to the author's consternation) become reduced to a length less than the effective degrees of freedom constrained, which is a problem. Uniform weighting in both the observation-combine and compression steps is the solution, and therefore care must be taken to remove particularly noisy data beforehand. In practice, the DASI instrument noise is very stable, resulting in very little loss in sensitivity due to uniform weighting of data as compared to inverse variance weighting.

The likelihood analysis software was extensively tested through analysis of simulated data, generated using independent software written by E. Leitch. The analysis software reliably recovered the input theoretical model within the estimated uncertainty. Omitting the constraint matrix leaves a sparse covariance matrix which can be rapidly inverted, and we can analyze a simulated data set in a few minutes of CPU time. Through Monte Carlo studies of many simulated data sets we are able to accurately recover the input power spectrum with mean uncertainties matching those predicted by the likelihood analysis. Ground signal and point source constraints were tested by constraining these modes in simulated data which contained both ground and point source components; both ground signal and point sources are effectively eliminated, and the constraint matrices do not introduce artifacts into the power spectrum (Fig. 6.11).

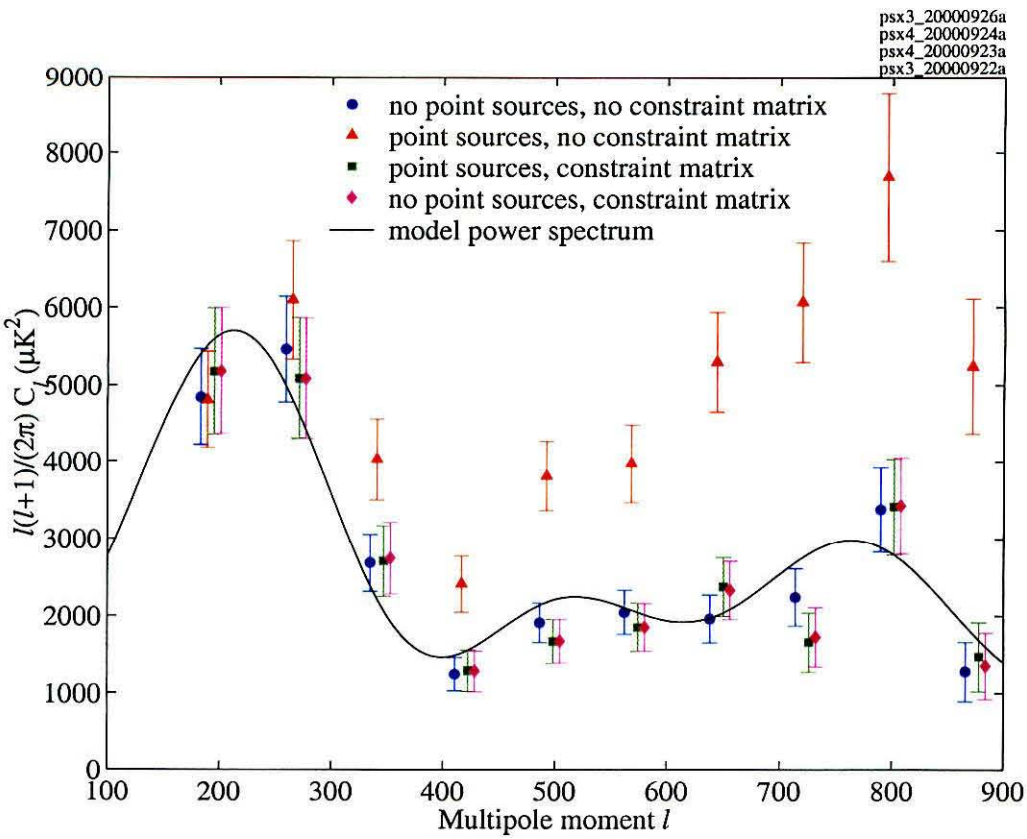

Figure 6.11 Test of the analysis software using simulated data. The data simulates DASI observations of one realization of the sky generated from an input theoretical model (solid line), as well as instrument noise and, optionally, point sources. Shown are the recovered power spectrum with (triangles) and without (circles) added point sources. We test the effectiveness of constraint matrices in removing the point source contribution (squares), and the effect of using the point source constraint matrices on data where no point sources are present (diamonds). Data points are incrementally offset to the right for display purposes. Direct comparison by eye of the simulated measurement to the underlying theoretical power spectrum should be done with the caveat that the band-power window functions, Fig. 6.4, and band-power covariance matrix are needed to quantitatively assess consistency.

6.13 Summary

We have successfully adapted the iterated maximum likelihood (ML) estimator techniques of Bond et al. (1998) and Bond et al. (2000), commonly used in the angular power spectrum analysis of swept-beam type experiments, to the analysis of interferometry data. Unlike swept-beam experiments, no map-making step is required; the angular power spectrum may be estimated directly from the visibility data. The theory covariance matrix elements, which describe how statistical fluctuations in the sky brightness are manifested in the datavector, are straightforward to calculate (White et al. 1999a,b; Hobson et al. 1995); only knowledge of the aperture field (or beam pattern) and baseline vectors is required. A simple quadratic estimator constructed from the square of the individual visibilities (White et al. 1999b) is fast, and useful for making sensitivity estimates, but the iterated ML estimator, although slower because of the required matrix inversions, allows the use of a constraint matrix to effectively marginalize over potentially contaminated modes in the data. Although this technique can be computationally prohibitive for large datavectors, the ability of the DASI interferometer to make pointed observations on widely-separated (and therefore uncorrelated) fields on the sky makes the ML estimator computationally feasible while allowing us to tailor the length and number of observations to achieve a given science goal. CMB datasets are notoriously difficult to analyze due to the weakness of the measured signal and the presence of potentially dominating systematic effects. Despite the apparent complexity and sophistication of the techniques described above, power spectrum analysis with interferometry data is relatively straightforward, allowing for rapid analysis and systematics checks even as data are being taken.

Chapter 7

Results

7.1 Introduction

In the first season of CMB observations with DASI, our goal was to make a precise measurement of the CMB angular power spectrum in the multipole moment range $100 < l < 900$, the region of the predicted first to third harmonic peaks in a flat Universe. The observations described in Chapter 5 were designed to achieve this goal; we took measurements in 32 well separated fields on the sky, a strategy designed to minimize sample variance and facilitate rapid analysis while allowing us to effectively remove any ground signal. In the observations of the four rows of eight fields, observed for 28–62 hr per field, we conservatively chose long integration times, which allowed us to probe deeply for possible systematic effects, and produce a power spectrum dominated by sky sample variance, rather than instrument noise, making the analysis robust against possible mis-estimates of the noise. We have successfully extracted a power spectrum, making detections in the nine bands with fractional uncertainties of 10–20%, and have extracted fundamental cosmological parameters from the power spectrum measurements. These results were recently reported in Leitch et al. (2001), Halverson et al. (2001), and Pryke et al. (2001). In this Chapter we report the power spectrum results from Halverson et al. (2001), along with tests for consistency and possible contamination by diffuse foregrounds. A discussion of the results, including constraints on cosmological parameters, is reserved for Chapter 8.

7.2 Angular Power Spectrum Analysis

7.2.1 Analysis Formalism Summary

We apply the maximum likelihood analysis formalism described in Chapter 6 to measure the CMB angular power spectrum for a piecewise flat ($l(l+1)C_l$) power spectrum in nine bands, as well as its temperature spectral index. As input to the analysis, we use the calibrated and edited DASI data discussed in Chapter 5, for 32 fields of observations. A datavector $\mathbf{\Delta}$ of length $N = 1560 \times 32$ (before data edits) is constructed by combining observations of each visibility for each of the 32 fields. The likelihood function for a set of parameters κ is

$$\mathcal{L}_{\mathbf{\Delta}}(\kappa) = \frac{1}{(2\pi)^{N/2}\,|C(\kappa)|^{1/2}} \exp\left(-\frac{1}{2}\mathbf{\Delta}^T C(\kappa)^{-1}\mathbf{\Delta}\right), \tag{7.1}$$

where the covariance matrix

$$C(\kappa) = C_T(\kappa) + C_n + C_C \tag{7.2}$$

is the sum of the theory, noise, and constraint covariance matrices, and is a function of the parameters. For the power spectrum analysis, the parameters κ that we estimate are the band powers, $u^2 S(u) \approx l(l+1)C_l/(2\pi)^2$. The theory covariance matrix, C_T, is then given by

$$C_T(\kappa) \equiv \left\langle \mathbf{V}\mathbf{V}^T \right\rangle = \sum_p \kappa_p B_p, \tag{7.3}$$

where $\mathbf{V}$ is the vector of noiseless theoretical visibilities. The matrices B_p represent the instrument filter function to fluctuation power on the sky, Eq. 6.61. They are constructed from the overlap integral of the aperture field autocorrelation functions of pairs of baselines where they sample the same Fourier modes on the sky. We use the theoretical aperture fields in this calculation, which is justified by the good agreement between the theoretical and measured beams (§3.4.2). Fields are separated such that the interfield datavector elements are essentially uncorrelated except in the highest elevation row, for which we calculate the appropriate correlations.

7.2.2 Noise Estimation

We model the noise covariance matrix of the combined visibility datavector as diagonal, with elements $C_{nii} = \sigma_{ii}^2$ estimated from the sample variance in the 8.4-s integrations over the 1-hr observations. To verify the assumption that C_n is diagonal, we have calculated the sample covariance matrix from the data in each of the ten frequency channels for all 1-hr observations. We find rare occasions where the visibilities are strongly correlated due to atmospheric fluctuations. Our weather edits, described in §5.4, consist of cuts based on the strength of these correlations; we cut observations in which any off-diagonal correlation coefficient exceeds ± 0.36, but the data consistency does not depend strongly on this value.

7.2.3 Ground Constraints

To reduce near-field ground contamination and point source contributions to the power spectrum, we employ the constraint matrix formalism described in §6.8 to marginalize over potentially contaminated modes in the data. Specifically, for a given mode q, we construct a constraint matrix from the outer product of a template vector $\mathbf{T_q}$,

$$C_{Cq} = \mathbf{T_q}\mathbf{T_q}^T \tag{7.4}$$

and

$$C_C = \alpha \sum_q C_{Cq}, \tag{7.5}$$

where α is a number large enough to de-weight the undesired modes without causing the covariance matrix to become singular to working precision. In practice we are able to vary α over seven orders of magnitude without affecting the results. To reduce sensitivity to the ground signal, we apply a constraint which marginalizes over a common component across eight fields in a given observation for each visibility, as described in the example in §6.8. Additionally, using sensitive consistency tests described in §7.4, we find evidence of a temporally drifting component of the ground

signal on 1- to 8-hr time scales, subtle but present for all baselines and noticeably stronger for short baselines. We therefore apply a linear drift constraint to all visibilities, and a quadratic constraint for $|\mathbf{u}| < 40$. The additional constraints have little effect on the power spectrum, which makes us confident that sensitivity to ground signal is effectively eliminated.

7.2.4 Point Source Constraints

As predicted for our experimental configuration (Tegmark & Efstathiou 1996), point sources are the dominant foreground in the DASI data. To remove point source flux contributions using the constraint matrix formalism above, we require only the positions of the sources, *not their flux densities.* We constrain 28 point sources detected in the DASI data itself, in which we can detect a 40 mJy source at beam center with $> 4.5\,\sigma$ significance. The estimated point source flux densities range from 80 mJy to 7.0 Jy (see Table 5.2). We also constrain point sources from the PMN southern (PMNS) catalog (Wright et al. 1994) with 4.85 GHz flux densities, S_5, which exceed 50 mJy when multiplied by the DASI primary beam. We use this flux density limit for the constrained point sources because the loss of degrees of freedom resulting from the inclusion of all point sources in the PMNS catalog would be prohibitively large. We have tested for the effect of possible absolute pointing error by displacing the point source position templates. A uniform displacement of the PMNS catalog coordinates by less than or equal to our estimated pointing error of $2'$ (see §5.2) does not have a significant effect on the angular power spectrum, except in the three highest-l bins where the effect is $\sim 10\%$. For the brightest point sources, positions accurate to $< 1'$ are required. We can extract positions to the necessary accuracy from the DASI data.

In addition to the point sources constrained above, we make a statistical correction for residual point sources which are too faint to be detected by DASI or included in our PMN source table. To do this, we estimate the point source number count per

unit flux density at 4.85 GHz, dN/dS_5, derived from the PMNS catalog, and the distribution of 31 GHz to 4.85 GHz flux density ratios, S_{31}/S_5, derived from new observations for this purpose with the OVRO 40 m telescope in Ka band (paper in preparation). We proceed to calculate the statistical correction for unconstrained residual point sources $S_{31} > 1$ mJy using Monte Carlo techniques; we generate random point source distributions at 4.85 GHz using dN/dS_5 and statistically extrapolate the flux density of each source to each of our ten frequency channels using S_{31}/S_5. These simulated point sources are superimposed on CMB temperature fluctuations and observed with DASI simulation software; a power spectrum is then generated with the analysis software. The resulting mean amplitudes and uncertainties of the residual point source contribution to the nine band powers are [20±70, 70±80, 90±70, 180 ± 70, 240 ± 80, 330 ± 100, 400 ± 100, 500 ± 170, 430 ± 170] μK^2. The reported uncertainties are due to sky sample variance of the point source population in the simulations, uncertainty in dN/dS_5, and uncertainty in S_{31}/S_5. The residual point source contribution diminishes in the ninth band since that band power is dominated by visibilities from the highest frequency channels where the average point source flux density is lower relative to its mean flux density across all ten frequency channels. We use these statistically estimated amplitudes and uncertainties to adjust our CMB band-power estimates and uncertainties reported below.

7.3 Angular Power Spectrum Results

The CMB angular power spectrum from the first season of DASI data is shown in Figure 7.1, with maximum likelihood estimates of nine band powers, piecewise flat in $l(l+1)C_l/(2\pi)$, spanning the range $100 < l < 900$. Adjacent bands are anticorrelated at the 20% level. In addition, we show an alternate analysis of the same data, for nine bands shifted to the right with respect to the original band edges, in order to demonstrate the robustness of the analysis against possible effects due to the anticorrelation of adjacent bands. Note that these two analyses use the

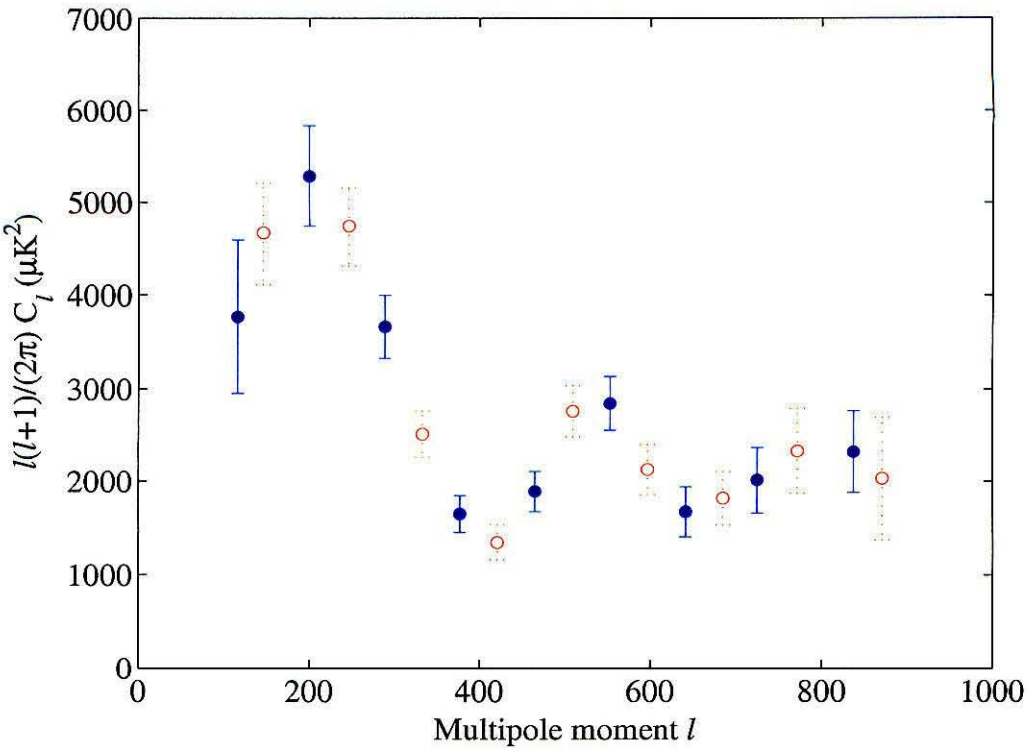

Figure 7.1 The angular power spectrum from the first season of DASI observations, plotted in nine bands (filled circles). We have analyzed the same data in nine bands shifted to the right (open circles). The alternate set of band powers is shown to demonstrate the robustness of the likelihood analysis code. To extract cosmological parameters, only the nine bands shown in the primary (filled circle) analysis are used. Adjacent bands are anticorrelated at the 20% level (see Table 7.2). In addition to the uncertainties plotted above, there is an 8% calibration uncertainty in units of power (4% in $\Delta T/T$), which is completely correlated across all bands due to the combined flux scale and beam uncertainties.

same data to estimate band powers in two different piecewise flat theoretical power spectra; only the first nine-band analysis (filled circles) is used for the cosmological parameter estimation. While increasing the number of bands above nine may in principle provide more information about the underlying power spectrum, in practice we find that increasing the number of bands does not improve our ability to constrain cosmological parameters.

In a separate analysis, we fit for the maximum likelihood value of an additional

parameter, the temperature spectral index of the fluctuations, β, where $T \propto \nu^{\beta}$. Fitting a single spectral index for all nine bands, we find $\beta = -0.1 \pm 0.2$ ($1\ \sigma$), while fitting a separate spectral index for $l < 500$ and $l > 500$ yields $\beta = -0.2 \pm 0.3$ and 0.0 ± 0.4 respectively, indicating the fluctuation power is consistent with CMB.

Values and marginal uncertainties for the angular power spectrum in the primary nine bands are given in Table 7.1. The center and $e^{-1/2}$ widths of the bands are calculated using band-power window functions adapted from Knox (1999) which are plotted in Paper III. These are the relevant window functions for calculating the expectation value of the band power given a theoretical power spectrum. We give the ratio of the uncertainty due to sky sample variance to the uncertainty due to noise, $\sigma_{\rm s}/\sigma_{\rm n}$, estimated using the offset log-normal formalism of Bond et al. (2000). In their notation, $\sigma_{\rm s}/\sigma_{\rm n}$ is given by $\mathcal{C}_B/x_B$, where $\mathcal{C}_B$ is the band power estimate expressed as $l(l+1)C_l/(2\pi)$ and x_B is proportional to the instrument noise contribution to the band-power uncertainty. These values may be used to estimate the non-Gaussianity in the band-power marginal likelihood distributions for parameter estimation calculations — asymmetric uncertainties due to non-Gaussianity are negligible for most of our band powers and we do not plot them here. We also tabulate the band-power correlation matrix (Table 7.2). All of the data products necessary for performing cosmological parameter estimation from this data are available at our website[1].

7.4 Consistency Tests

We perform three types of tests to check the consistency of the data: i) χ^2 tests on the difference between two visibility datavectors constructed from observations of the same fields on the sky, ii) construction of a nine-band power spectrum of the epoch-differenced visibility datavector, to test for significant deviation from zero power, and iii) χ^2 tests on the difference between two power spectra constructed from independent fields on the sky. In the second and third types of test, we increase

[1] `http://astro.uchicago.edu/dasi`

$l_{\rm eff}$[a]	$l_{\rm l}$[b]	$l_{\rm h}$[b]	$l(l+1)C_l/(2\pi)$ (μK^2)	$\sigma_{\rm s}/\sigma_{\rm n}$ [c]	$l(l+1)C_l^{\rm E1-E2}/(2\pi)$ (μK^2)[d]
118	104	167	3770 ± 820	23.6	-250 ± 160
203	173	255	5280 ± 550	31.6	140 ± 120
289	261	342	3660 ± 340	18.7	120 ± 120
377	342	418	1650 ± 200	7.3	160 ± 140
465	418	500	1890 ± 220	4.3	70 ± 240
553	506	594	2840 ± 290	4.0	0 ± 300
641	600	676	1670 ± 270	2.3	120 ± 420
725	676	757	2010 ± 350	1.7	-90 ± 580
837	763	864	2320 ± 450	1.1	-490 ± 850

[a] $l_{\rm eff}$ is the band-power window function weighted mean multipole moment (see text).

[b] $l_{\rm l}$ and $l_{\rm h}$ are the low and high $e^{-1/2}$ points of the band-power window function.

[c] $\sigma_{\rm s}/\sigma_{\rm n}$ is the ratio of the uncertainty attributable to sky sample variance to the uncertainty attributable to noise (see text).

[d] Power spectrum of the epoch-differenced datavector described in §7.4.

Table 7.1 Angular power spectrum band powers and uncertainties. The uncertainties listed above do not include flux scale and beam calibration uncertainties. The total combined calibration uncertainty is 8% ($1\,\sigma$), expressed as a fractional uncertainty on the C_l band powers (4% in $\Delta T/T$).

the number of frequency channels which are combined in the datavector in order to reduce the computational time required to produce the power spectra. This increased data compression yields a power spectrum similar to the one reported above.

Of the three types of test, the first is the most powerful tool for detecting non-Gaussianity or incorrect estimates of the noise. The reduced χ^2 statistic is

$$\chi^2/N = (\mathbf{\Delta}_1 - \mathbf{\Delta}_2)^T (C_{n1} + C_{n2} + C_{Cg})^{-1} (\mathbf{\Delta}_1 - \mathbf{\Delta}_2)/N, \tag{7.6}$$

1	−0.243	0.0349	-5.87×10^{-3}	1.09×10^{-3}	-3.01×10^{-4}	-1.08×10^{-4}	-1.24×10^{-4}	-1.99×10^{-4}
	1	−0.182	0.0286	-6.65×10^{-3}	3.90×10^{-4}	-1.00×10^{-3}	-6.88×10^{-4}	-4.85×10^{-4}
		1	−0.196	0.0372	-8.84×10^{-3}	-1.61×10^{-3}	-2.82×10^{-3}	-2.74×10^{-3}
			1	−0.234	0.0334	−0.0149	-5.52×10^{-3}	-6.69×10^{-3}
				1	−0.193	0.0247	−0.0193	-8.22×10^{-3}
					1	−0.219	0.0394	−0.0200
						1	−0.275	0.0339
							1	−0.220
								1

Table 7.2 Correlation coefficient matrix for the DASI band powers given in Table 7.1.

where $\mathbf{\Delta}_1$ and $\mathbf{\Delta}_2$ are the two datavectors, C_{n1} and C_{n2} are the (diagonal) noise covariance matrices, C_{Cg} is the same ground constraint matrix that is used in the power spectrum likelihood analysis, and $N = \dim \mathbf{\Delta} - \text{rank } C_{Cg}$ are the degrees of freedom. We split the visibilities between the two epochs of available observations for each field row, yielding $\chi^2/N = 1.03$. This χ^2 value is significant given the $N \sim 3\times10^4$ degrees of freedom — it indicates that the noise may be slightly non-Gaussian. In fact, we see improvement of this statistic if we increase the severity of the lunar cuts, but the effect on the power spectrum is negligible. It may also indicate that we slightly underestimate the noise of the data. However, the uncertainties in all bands are dominated by sky sample variance, rather than instrument noise, making the power spectrum robust against a noise underestimate of this magnitude.

A power spectrum in nine bands was created from the epoch-differenced datavector, and tested for deviation from zero power using a χ^2 statistic, with the result $\chi^2/N = 9.5/9$, which is consistent within the 68% confidence interval. The band powers for the epoch-differenced power spectrum are given in Table 7.1.

We use a χ^2 statistic to test the consistency between power spectra generated from each of the four field rows, shown in Fig. 7.2. The χ^2 statistic is constructed from the difference between two power spectra which sample independent sky, $\chi^2 = (\mathcal{D}_1 - \mathcal{D}_2)^T (P_1 + P_2)^{-1} (\mathcal{D}_1 - \mathcal{D}_2)$, where $\mathcal{D}_1, \mathcal{D}_2$ are the band-power vectors and P_1, P_2 are the band-power covariance (inverse Fisher) matrices. The non-Gaussianity of the DASI power spectrum uncertainties is small, which justifies using a χ^2 statistic; we have tested its validity with Monte Carlo techniques on simulated data and have not found a significant deviation from a χ^2 distribution. The resulting values, with format χ^2/N (χ^2 cumulative distribution function percentile), are: 14.9/9 (91%), 13.3/9 (85%), 10.9/9 (72%), 4.5/9 (12%), 6.2/9 (28%) and 3.7/9 (7%) for the A–B, A–C, A–D, B–C, B–D, C–D differenced field row pairs, respectively. The power spectra of the four field rows are in reasonable agreement.

To test the efficacy of the point source constraints described in §7.2.4, we split

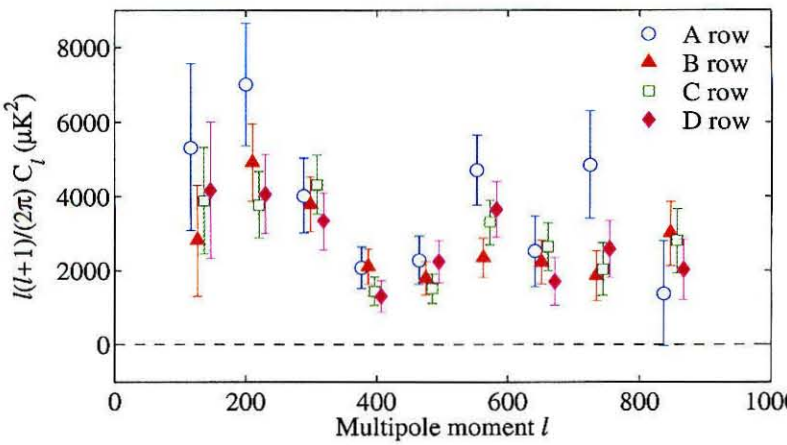

Figure 7.2 The angular power spectrum of the four individual field rows, used for χ^2 consistency tests. The integration time for each field row is 28, 38, 56, and 62 hr per field for the A, B, C, and D rows, respectively. The power spectra shown here are not corrected for the residual point source contribution.

the data in each field row between the four fields with the highest and the four with the lowest detected point source flux, and create power spectra from the two sets of combined fields. The χ^2/N value for the difference between the two power spectra is 11.5/9 (75%) indicating they are consistent within the 68% confidence interval.

Although point sources are the foreground of primary concern for DASI, constraint matrices are demonstrably effective in removing this point source power, and the consistency tests above show that the power spectra from sets of fields with very different point source flux contributions are in good agreement after the constraint matrix is applied.

7.5 Diffuse Foregrounds

We place limits on the contribution of other diffuse foregrounds to the power spectrum by creating constraint matrices from foreground templates. The constraint matrix formalism is a powerful technique to place limits on foregrounds with a known relative

intensity distribution, since it allows for arbitrary scaling of the template amplitude and spectral index, without knowledge of these quantities at microwave frequencies. We create foreground images centered on each of the DASI fields from the cleaned IRAS 100 μm maps of Finkbeiner et al. (1999), cleaned 408 MHz Haslam survey maps (Haslam et al. 1981; Finkbeiner 2001), and Hα maps (Gaustad et al. 2000; McCullough 2001). These images are converted to visibility template vectors with the DASI simulation software. We marginalize over modes in the data which match the templates using the constraint matrix formalism described in §6.8. We constrain a separate arbitrary template amplitude and spectral index for each DASI field. With the addition of all of these foreground constraints, the maximum change in a band power is 3.3%, with most bands changing by less than 1%.

The Haslam map has a resolution of $\sim 1°$, making it inadequate as a template for multipole moments $\gtrsim 200$; however, the power spectrum of synchrotron emission is expected to decrease with l (Tegmark & Efstathiou 1996). Also, the Hα images show very low emission in the region of the DASI fields, and are of questionable use as a template. As a second method of characterizing possible free-free emission, we convert the Hα images to brightness temperature at our frequencies assuming a gas temperature of 10^4 K (Kulkarni & Heiles 1988). Subsequent power spectrum analysis of the converted image visibility templates yields a $< 1\%$ contribution to our band powers in all bands.

We conclude that dust, free-free, and synchrotron emission, as well as emission with *any* spectral index that is correlated with these templates, such as spinning dust grain emission (Draine & Lazarian 1998), make a negligible contribution to the CMB power spectrum presented here.

Chapter 8

Conclusions

In its initial season, the Degree Angular Scale Interferometer has successfully measured the angular power spectrum of the CMB over the range $l = 100$–900 in nine bands with high precision. The interferometer provides a simple and direct measurement of the power spectrum, with systematic effects, calibration methods, and beam uncertainties which are very different from single-dish experiments. We have made extensive use of constraint matrices in the analysis as a simple method for projecting out undesired signals in the data, including ground-signal common modes and point sources with arbitrary spectral index. The constraint matrix formalism is also used as a powerful test of correlations with foreground templates having arbitrary flux and spectral index scaling; we find no evidence of diffuse foregrounds in the data.

We see strong evidence for both first and second peaks in the angular power spectrum at $l \sim 200$ and $l \sim 550$, respectively, and a rise in power at $l \sim 800$ that is suggestive of a third. The detection of harmonic peaks in the power spectrum is a resounding confirmation that sub-degree scale anisotropy in the CMB is the result of gravitationally driven acoustic oscillations seeded by primordial adiabatic density perturbations.

Within the context of standard cosmological models, we can use the DASI angular power spectrum results to place quantitative constraints on fundamental cosmological parameters. As discussed in Chapter 1, the theoretical angular power spectrum is dependent upon cosmological parameters such as the density of baryons Ω_b, cold

dark matter density Ω_{cdm}, vacuum energy density Ω_Λ, the Hubble parameter h, the spatial spectral index of the primordial fluctuations n_s, and the optical depth due to reionization τ_c, among others. The total matter density is $\Omega_m \equiv \Omega_b + \Omega_{cdm}$ and the total density is $\Omega_{tot} \equiv \Omega_m + \Omega_\Lambda$, where all density parameters Ω_i are given as ratios with respect to the critical density, for which the Universe is spatially flat. The models which we use assume there are no significant tensor perturbations due to gravity waves and no "hot" dark matter component such as massive neutrinos, since these are thought to be unlikely to contribute to the CMB angular power spectrum at a significant level compared with the DASI measurement uncertainties (Lyth 1997; Dodelson et al. 1996). We can compare theoretical power spectra which depend on the above cosmological parameters to the DASI measured power spectrum shown in Fig. 7.1 using the χ^2 statistic discussed in §6.11, and place constraints on cosmological parameters. We calculate theoretical power spectra using `cmbfast` (Zaldarriaga & Seljak 2000) on a seven-dimensional grid over the parameters (Ω_{tot}, Ω_Δ, $\Omega_b h^2$, $\Omega_{cdm} h^2$, τ_c, n_s, C_{10}), where $\Omega_\Delta = \Omega_m - \Omega_\Lambda$ and C_{10} is an overall normalization constant. In addition, we use $l \leq 25$ band-power measurements from the COBE-DMR satellite experiment (Bennett et al. 1996), as provided in the `RADPACK` distribution (Knox 2000; Bond et al. 2000) to constrain the power spectrum at low multipole moments. Details of the cosmological parameter estimation are given in Pryke et al. (2001); the results of that paper are summarized here.

We find both the simultaneous maximum likelihood (minimum χ^2) value for all seven cosmological parameters, as well as marginal distributions for each of the parameters. The peak of the seven-dimensional likelihood surface lies at the parameter values $(\Omega_m, \Omega_\Lambda, \Omega_b h^2, \Omega_{cdm} h^2, \tau_c, n_s, C_{10}) = (0.725, 0.325, 0.020, 0.15, 0.0, 0.95, 800)$, equivalently $(\Omega_b, \Omega_{cdm}, \Omega_\Lambda, \tau_c, n_s, h) = (0.09, 0.64, 0.33, 0, 0.95, 0.48)$, with $\chi^2 = 29.5$ for the 9 DASI plus 24 DMR band-powers which indicates the model has a reasonable fit to the data, if we assume seven degrees of freedom or less taken away by the parameters. This "best fit" power spectrum is shown in Fig. 8.1, along with the "median"

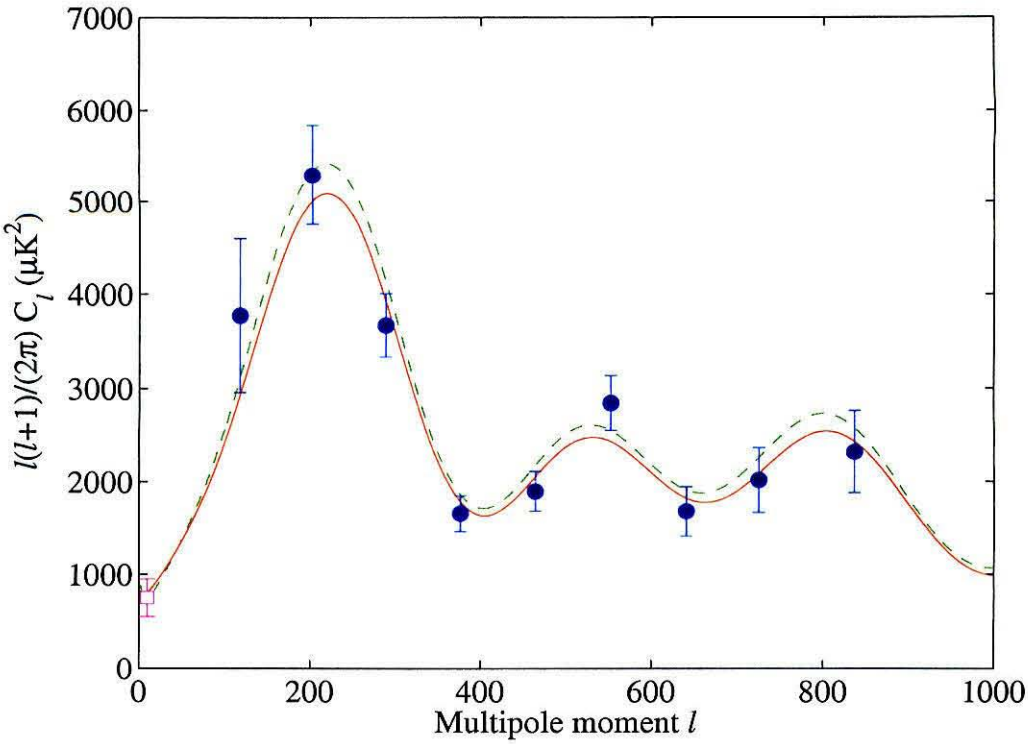

Figure 8.1 The DASI first-season angular power spectrum in nine bands (filled circles) with cosmological models. The DMR data are shown compressed to the single lowest-l point (open square). The solid (red) line is the best fitting model which falls on our grid, $(\Omega_m, \Omega_\Lambda, \Omega_b h^2, \Omega_{cdm} h^2, \tau_c, n_s, C_{10}) = (0.725, 0.325, 0.020, 0.15, 0.0, 0.95, 800)$, while the dashed (green) shows the model using the median values of the individually marginalized parameters with the priors $0.0 \leq \tau_c \leq 0.4$ and $h \geq 0.45$ (see Table 8.1).

model from the individually marginalized constraints described below. Because of a degeneracy between Ω_m and Ω_Λ, this best fit model is not particularly meaningful, but it demonstrates that there are models within the model grid which are good fits to the data.

We break this degeneracy in the marginal constraints by invoking priors in the Hubble parameter, both a weak prior, $h \geq 0.45$, and a strong prior, $h = 0.72 \pm 0.08$, from the HST Key project (Freedman et al. 2001). Figure 8.2 shows the marginal likelihood distributions for the implicit priors $(\Omega_{tot} \leq 1.3, \Omega_\Delta \leq 3.4, 0.0 \leq \tau_c \leq 0.4)$

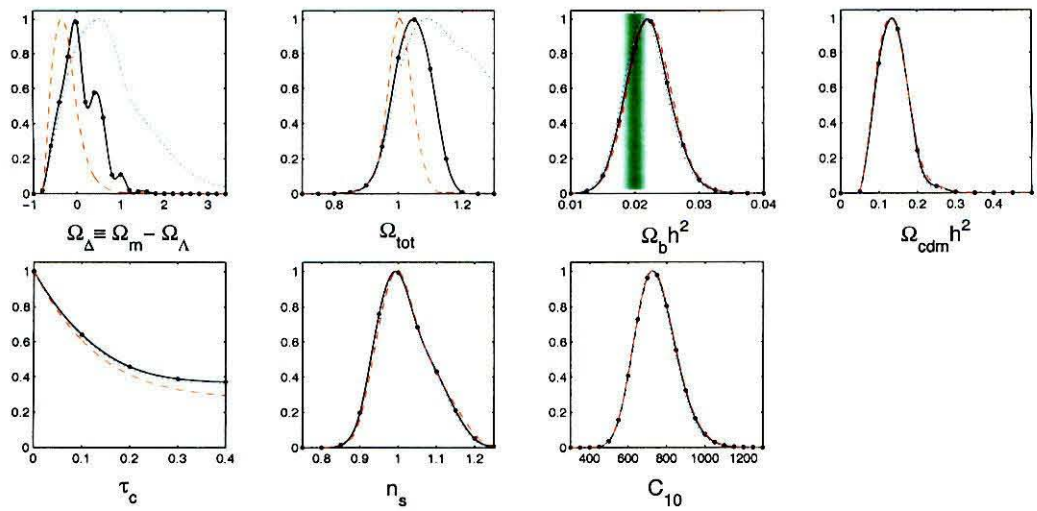

Figure 8.2 Cosmological parameter marginal likelihood distributions for each parameter on the model grid. The three sets of lines show the effect of varying the prior on the Hubble parameter h. The dotted (blue) lines use no h prior, the solid (black) lines use a weak prior, $h > 0.45$, and the dashed (red) lines use a strong prior, $h = 0.72 \pm 0.08$. The panel for the parameter $\Omega_b h^2$also shows the Big Bang Nucleosynthesis (BBN) constraint as a (green) shaded region (see text). All curves are normalized to a peak height of unity, and are spline interpolations of the actual model grid values shown by the points.

imposed by our grid boundaries, as well as the weak and strong h priors. The power to constrain Ω_{tot} and Ω_Δ is almost wholly dependent on the strength of the h prior, whereas all other parameters are barely affected by the choice of h prior. When the weak h prior is invoked, the model grid encompasses the significant likelihood region in all parameters but the optical depth due to reionization, τ_c. Table 8.1 summarizes parameter confidence intervals, assuming the weak h prior and $0.0 \leq \tau_c \leq 0.4$, but excludes Ω_Δ since our constraint on this parameter depends wholly on the h prior.

The prior on τ_c imposed by the choice of grid boundary is significant, and until very recently, τ_c has not been a well known parameter. Our external knowledge of τ_c is derived from searches for the Gunn-Peterson effect in the line of sight to high-redshift quasars, and theoretical considerations of structure formation and energy emission in the early Universe, which indicate $0.02 \leq \tau_c \leq 0.4$ (Haiman & Knox

Parameter	2.5%	16%	50%	84%	97.5%	mode
Ω_{tot}	0.927	0.986	1.045	1.103	1.150	1.047
$\Omega_b h^2$	0.0156	0.0187	0.0220	0.0255	0.0292	0.0220
$\Omega_{cdm} h^2$	0.075	0.100	0.137	0.175	0.225	0.135
n_s	0.901	0.949	1.010	1.092	1.166	0.993
C_{10}	558	642	741	852	973	728

Table 8.1 Cosmological parameter constraints from DASI+DMR data for a seven-dimensional grid, assuming the weak prior $h > 0.45$ and $0.0 \leq \tau_c \leq 0.4$. Tabulated are percentiles on the marginal cumulative distribution functions, as well as the mode (maximum likeliood value).

1999), making our prior $0.0 \leq \tau_c \leq 0.4$ reasonable. Very recently (a few weeks ago!), new results were reported in which the Gunn-Peterson effect was observed toward a $z = 6.28$ quasar discovered by the Sloan Digital Sky Survey (SDSS), yielding for the first time strong evidence for reionization at a redshift $z \sim 6$ (Becker et al. 2001). If this result is confirmed, the optical depth due to reionization is $\tau_c \sim 0.02$, a boon to CMB observers, since it indicates negligible scattering of the CMB photons due to reionization. In Fig. 8.3 we show the effect of setting $\tau_c = 0$; the primary effect is on our estimation of n_s, which is expected due to the degeneracy of these parameters, both of which produce tilts in the power spectrum.

The DASI power spectrum and associated cosmological parameter constraints confirm key predictions of inflation. The DASI detection of the predicted harmonic peaks in the CMB angular power spectrum confirms the presence of primordial adiabatic density perturbations, which rise naturally in inflationary theories. The DASI constraints on the total density, $\Omega_{tot} = 1.04 \pm 0.06$, and on the spatial spectral index of the primordial fluctuations $n_s = 1.01^{+0.08}_{-0.06}$ (both assuming the conservative priors $0.0 \leq \tau_c \leq 0.4$ and $h \geq 45$) are remarkably consistent with a spatially flat Universe and with scale invariant primordial density fluctuations predicted by non-baroque inflationary theories. (All DASI constraints reported here are with 68% confidence limits.) The implications of inflation are astounding; our Universe is many times more vast than the visible Universe with which we are causally connected.

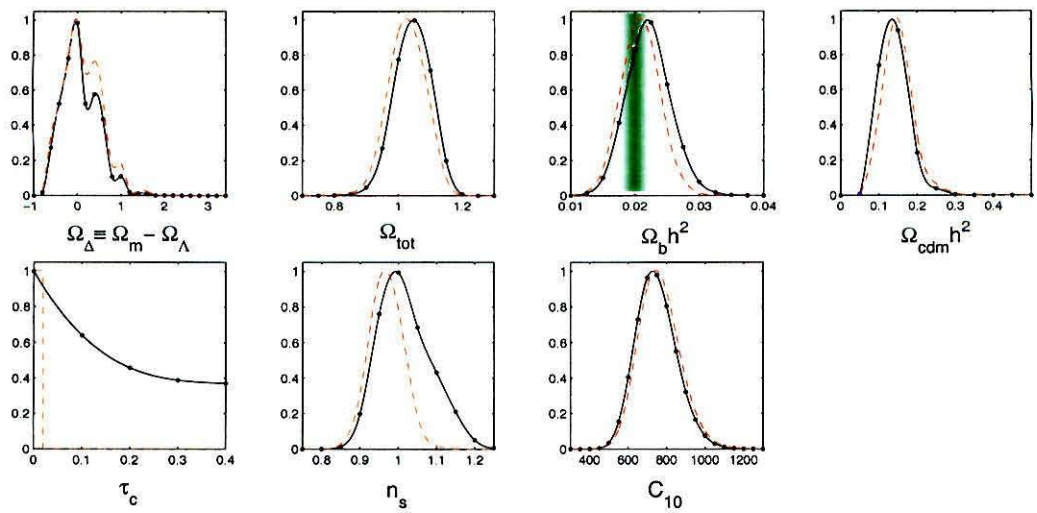

Figure 8.3 Marginal likelihood distributions when varying the prior on τ_c. The solid (black) lines are the same as in Fig. 8.2 and assume $0.0 \leq \tau_c \leq 0.4$, while for the dashed (red) lines $\tau_c = 0.0$. All curves assume the weak prior $h > 0.45$.

The DASI results also place stringent limits on the densities of the various components which constitute the Universe. The DASI results provide a measurement of the matter content of the Universe which is independent of, but in excellent agreement with, a host of previous measurements probing entirely different epochs and physical processes. The DASI constraint on the baryonic matter density $\Omega_b h^2 = 0.022^{+0.004}_{-0.003}$ (assuming the same conservative priors) is consistent with the constraint, $\Omega_b h^2 = 0.020 \pm 0.002$ (95% confidence limits), set by Big Bang Nucleosynthesis (BBN) theory in conjunction with the primordial Deuterium-Hydrogen ratio as measured in adsorption along the line of sight to high-redshift quasars (Burles et al. 2001). The DASI results, along with a new analysis of the BOOMERanG data (Netterfield et al. 2001, see Fig.8.4), provide constraints which are in very good agreement with the BBN value. This agreement beautifully links together two pillars of the Big Bang theory, and buttresses our understanding of the early Universe as it evolved from the the epoch of nucleosynthesis in the first few minutes after creation to the generation of the CMB some 400,000 years later.

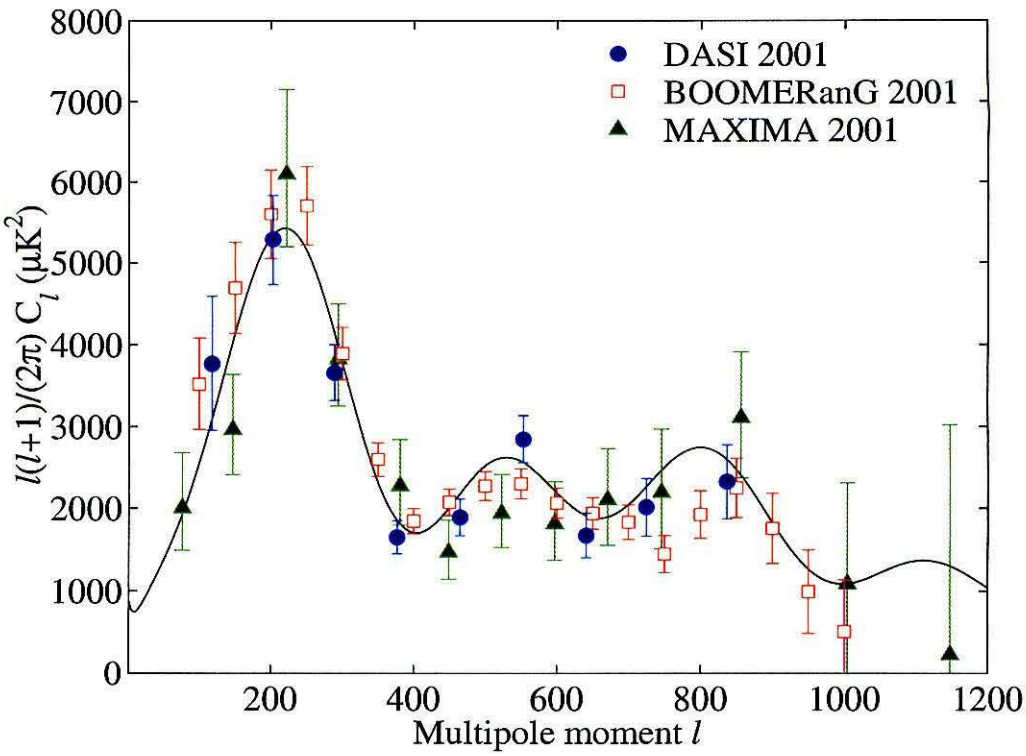

Figure 8.4 The DASI power spectrum, shown with new analyses of the BOOMERanG (Netterfield et al. 2001) and MAXIMA-1 (Lee et al. 2001) data, all three released at the April 2001 American Physical Society meeting in Washington, DC. Beam and calibration uncertainties are not shown.

The DASI constraint on the dark matter content of the Universe, $\Omega_{cdm}h^2 = 0.14 \pm 0.04$ (again with priors $0.0 \leq \tau_c \leq 0.4$ and $h \geq 0.45$), agrees well with strong evidence for non-baryonic matter in the Universe indicated by a variety of previous observations and theoretical arguments (e.g., see review by Turner 1999, and references therein). As an example, recent measurements of the gas mass fraction in clusters of galaxies in combination with BBN constraints for the baryon density place an upper limit $\Omega_m \lesssim 0.4$, with an intracluster gas mass fraction of ~ 0.1 (Mohr et al. 1999; Grego et al. 2001). Since the intracluster gas is believed to comprise the vast majority of baryonic matter in the clusters, this upper limit is roughly an equality ($\Omega_m \sim 0.25$), with the majority of matter non-baryonic. In adiabatic inflationary models, the

amplitude ratio of the first to higher-order peaks at $l \sim 10^3$ in the CMB angular power spectrum yields an estimate of the total matter content of the Universe (White 2001). In the DASI power spectrum, the rise in power in the region of the predicted third peak strongly supports, from CMB data alone, the presence of dark matter in the Universe.

Finally, "dark energy," modeled as vacuum energy, is confirmed by the DASI data. The vacuum energy, indistinguishable from Einstein's cosmological constant, Λ, was most recent resurrected in the mid-1990's in "concordance" models as a way to bridge the gap between the evidence for low matter content in the Universe and a strong theoretical prejudice for a spatially flat Universe arising from inflation theory (Ostriker & Steinhardt 1995; Krauss & Turner 1995). Measurements of the Hubble constant from observations of high-redshift type Ia supernovae revealed the Universe is accelerating, providing strong evidence for dark energy, assuming a flat Universe, $\Omega_m + \Omega_\Lambda = 1$ (Perlmutter et al. 1999; Riess et al. 1998). CMB data provide constraint ellipses in the Ω_m–Ω_Λ plane which are orthogonal to those provided by the supernovae data. The DASI data constrain $\Omega_{tot} = 1.00 \pm 0.04$, $\Omega_m = 0.40 \pm 0.15$, and $\Omega_\Lambda = 0.60 \pm 0.15$, assuming a strong Hubble parameter prior, $h = 0.72 \pm 0.08$, in remarkable agreement with concordance models and intersecting constraints from high-redshift supernovae observations.

With evidence from a diverse set of measurements probing entirely different epochs in cosmological history, a consistent story has emerged about the makeup of the Universe, at the same time verifying to a remarkable degree the hot Big Bang cosmology with inflationary origins. While some may be disappointed at the apparent lack of controversy, there are many questions yet to be answered; we have very little understanding of the matter and energy that comprise 95% of the energy density of the Universe. We can be proud of the recent achievements in our understandings of the origins of the Universe, but at the same time they reveal that our still nascent awareness of the cosmos has only just begun.

Bibliography

Albrecht, A. and Steinhardt, P. J. 1982, Phys. Rev. Lett., 48, 1220

Bailey, M. C. 1974, Analysis of finite size phased arrays of circular waveguide elements, Tech. Rep. TR R-408, NASA

Bardeen, J. M., Steinhardt, P. J., and Turner, M. S. 1983, Phys. Rev. D, 28, 679

Becker, R. H. *et al.* 2001, ApJ, submitted, astro-ph/0108097

Bennett, C. L. *et al.* 1996, ApJ, 464, L1

Birch, J. R., Dromey, J. D., and Lesurf, J. 1981, Infrared Physics, 21, 225

Bond, J. R. and Efstathiou, G. 1984, ApJ, 285, L45

Bond, J. R., Jaffe, A. H., and Knox, L. 1998, Phys. Rev. D, 57, 2117

—. 2000, ApJ, 533, 19, astro-ph/9808264

Burles, S., Nollett, K. M., and Turner, M. S. 2001, Phys. Rev. D, 63, 063512, astro-ph/0008495

Chamberlin, R. A., Lane, A. P., and Stark, A. A. 1997, ApJ, 476, 428

Clarricoats, P. J. B. 1969, Electron. Lett., 5, 189

Clarricoats, P. J. B. and Olver, A. D. 1984, Corrugated Horns for Microwave Antennas, IEE Electromagnetic Wave Series 18 (London: Peter Peregrinus)

Clarricoats, P. J. B. and Saha, P. K. 1969, Electron. Lett., 5, 592

Coble, K. *et al.* 1999, ApJ, 519, L5

Collin, R. E. 1985, Antennas and Radiowave Propagation (New York: McGraw-Hill)

de Bernardis, P. *et al.* 2000, Nature, 404, 955

Degenford, J. E. and Coleman, P. D. 1966, Proc. IEEE, 54, 520

Dicke, R. H., ed. 1970, Gravitation and the Universe (Philadelphia: American Philosophical Society)

Dodelson, S., Gates, E., and Stebbins, A. 1996, ApJ, 467, 10, astro-ph/9509147

Dragovan, M., Ruhl, J. E., Novak, G., Platt, S. R., Crone, B., Pernic, R., and Peterson, J. B. 1994, ApJ, 427, L67

Draine, B. T. and Lazarian, A. 1998, ApJ, 508, 157

Finkbeiner, D. P. 2001, private communication

Finkbeiner, D. P., Davis, M., and Schlegel, D. J. 1999, ApJ, 524, 867

Freedman, W. L. *et al.* 2001, ApJ, 553, 47

Gaustad, J. E., Rosing, W., McCullough, P. R., and van Buren, D. 2000, PASP, 220, 169

Goldsmith, P. F. 1982, in Infrared and Millimeter Waves, ed. K. J. Button, Vol. 6 (New York: Academic), 277

Gottschalk, T. D. 1995, A Short Overview of Statistical Inference, unpublished

Grego, L., Carlstrom, J. E., Reese, E. D., Holder, G. P., Holzapfel, W. L., Joy, M. K., Mohr, J. J., and Patel, S. 2001, ApJ, 552, 2

Guth, A. H. 1981, Phys. Rev. D, 23, 347

Guth, A. H. and Pi, S. Y. 1982, Phys. Rev. Lett., 49, 1110

Högbom, J. A. 1974, A&AS, 15, 417

Haiman, Z. and Knox, L. 1999, in ASP Conf. Ser. 181: Microwave Foregrounds, ed. A. de Oliveira-Costa & M. Tegmark, 227

Halverson, N. and Carlstrom, J. E. 2001, in preparation

Halverson, N. W., Carlstrom, J. E., Dragovan, M., Holzapfel, W. L., and Kovac, J. 1998, in Proc. SPIE, Vol. 3357, Advanced Technology MMW, Radio, and Terahertz Telescopes, ed. T. G. Phillips, 416

Halverson, N. W. *et al.* 2001, ApJ, submitted, astro-ph/0104489

Hanany, S. *et al.* 2000, ApJ, 545, L5, astro-ph/0005123

Harrison, E. R. 1970, Phys. Rev. D, 1, 2726

Haslam, C. G. T., Klein, U., Salter, C. J., Stoffel, H., Wilson, W. E., Cleary, M. N., Cooke, D. J., and Thomasson, P. 1981, A&A, 100, 209

Hawking, S. W. 1982, Phys. Lett. B, 115, 295

Hobson, M. P., Lasenby, A. N., and Jones, M. 1995, MNRAS, 275, 863

Hu, W., Sugiyama, N., and Silk, J. 1997, Nature, 386, 37, astro-ph/9604166

James, G. L. and Thomas, B. M. 1982, IEEE Trans. Microwave Theory Tech., MTT-30, 278

Jones, M. E. 1997, in Proc. XVIst Moriond Astrophysics Meeting: Microwave Background Anistropies, ed. F. Bouchet, R. Gispert, B. Guiderdoni, & J. Van (Gif-sur-Yvette: Editions Frontieres), 161

Jungman, G., Kamionkowski, M., Kosowsky, A., and Spergel, D. N. 1996, Phys. Rev. D, 54, 1332

Kildal, P. S., Jacobsen, K., and Sudhakar Rao, K. 1984, IEE Proc. H, 131, 390

King, J. C. and Turner, J. 1997, Antarctic Meteorology and Climatology (Cambridge: Cambridge University Press)

Knox, L. 1995, Phys. Rev. D, 52, 4307

—. 1999, Phys. Rev. D, 60, 103516, astro-ph/9902046

—. 2000, RADPACK, http://bubba.ucdavis.edu/~knox/radpack.html

Kolb, E. W. and Turner, M. S. 1990, The Early Universe (Reading, Mass.: Addison-Wesley)

Krauss, L. and Turner, M. S. 1995, Gen. Rel. Grav. 27, 1137, astro-ph/9504003

Kulkarni, S. R. and Heiles, C. 1988, in Galactic and Extragalactic Radio Astronomy, 2nd Edition, ed. G. L. Verschuur & K. I. Kellerman (New York: Springer-Verlag), 95

Lay, O. P. and Halverson, N. W. 2000, ApJ, 543, 787

Lee, A. T. *et al.* 2001, ApJ, submitted, astro-ph/0104459

Leitch, E. M. *et al.* 2001, ApJ, submitted, astro-ph/0104488

Linde, A. D. 1982, Phys. Lett. B, 108, 389

Lyth, D. H. 1997, Phys. Rev. Lett., 78, 1861

Mauskopf, P. D. *et al.* 2000, ApJ, 536, L59

McCullough, P. R. 2001, private communication

Meinhold, P. and Lubin, P. 1991, ApJ, 370, L11

Miller, A. D. *et al.* 1999, ApJ, 524, L1

Mohr, J. J., Mathiesen, B., and Evrard, A. E. 1999, ApJ, 517, 627

Morita, T. and Cohn, S. B. 1956, IRE Trans., AP-4, 33

Narlikar, J. V. and Padmanabhan, T. 1991, ARA&A, 29, 325

Netterfield, C. B. *et al.* 2001, ApJ, submitted, astro-ph/0104460

Olver, A. D. and Xiang, J. 1988, IEE Proc. H, 135, 34

Ostriker, J. P. and Steinhardt, P. J. 1995, Nature, 377, 600, astro-ph/9505066

Padin, S., Cartwright, J. K., and Joy, M. 2000, IEEE Trans. Antennas Propagat., 48, 836

Padin, S., Cartwright, J. K., Shepherd, M. C., Yamasaki, J. K., and Holzapfel, W. L. 2001a, IEEE Trans. Instrum. Meas., 50, 1234

Padin, S. *et al.* 2001b, ApJ, 549, L1, astro-ph/0012211

Padman, R. 1978, Electron. Lett., 14, 311

Pearson, T. J. *et al.* 2000, in IAU Symposium 201: New Cosmological Data and the Values of the Fundamental Parameters, ed. A. Lasenby & A. Wilkinson (ASP), astro-ph/0012212

Peebles, P. J. E. and Yu, J. T. 1970, ApJ, 162, 815

Penzias, A. A. and Wilson, R. W. 1965, ApJ, 142, 419

Perlmutter, S. *et al.* 1999, ApJ, 517, 565

Plambeck, R. L. 1999, private communication

Platt, S. R., Kovac, J., Dragovan, M., Peterson, J. B., and Ruhl, J. E. 1997, ApJ, 475, L1

Pospieszalski, M. W. 1993, in Proc. 23rd European Microwave Conf., Madrid, Spain (Tunbridge Wells, UK: Reed Exhibition Companies), 73

Pospieszalski, M. W., Nguyen, L. D., Lui, M., Lui, T., Thompson, M. A., and Delaney, M. J. 1994, in Proc. IEEE MTT-S Int. Microwave Symp., San Diego, CA (New York: IEEE), 1345

Pryke, C. *et al.* 2001, ApJ, submitted, astro-ph/0104490

Riess, A. G. *et al.* 1998, AJ, 116, 1009

Scott, D., Silk, J., and White, M. 1995, Science, 268, 829

Scott, D. and White, M. 1995, Gen. Rel. Grav. 27, 1023

Smoot, G. F. *et al.* 1992, ApJ, 396, L1

Starobinsky, A. A. 1982, Phys. Lett. B, 117, 175

Stuart, A., Ord, J. K., and Arnold, S. 1999, Kendall's Advanced Theory of Statistics, Vol. 2A (London: Arnold)

Takeichi, Y., Hashimoto, T., and Takeda, F. 1971, IEEE Trans. Microwave Theory Tech., MTT-19, 947

Tauber, J. A. 2000, in IAU Symposium 201: New Cosmological Data and the Values of the Fundamental Parameters, ed. A. Lasenby & A. Wilkinson (ASP)

Tegmark, M. 1997, Phys. Rev. D, 55, 5895

Tegmark, M. and Efstathiou, G. 1996, MNRAS, 281, 1297

Tegmark, M., Taylor, A. N., and Heavens, A. F. 1997, ApJ, 480, 22, astro-ph/9603021

Thomas, B. M. 1978, IEEE Trans. Antennas Propagat., AP-26, 367

Thomas, B. M., James, G. L., and Greene, K. J. 1986, IEEE Trans. Antennas Propagat., AP-34, 750

Thompson, A. R., Moran, J. M., and Swenson, G. W. 1991, Interferometry and Synthesis in Radio Astronomy (Malabar, Fla.: Krieger)

Tucker, G. S., Griffin, G. S., Nguyen, H. T., and Peterson, J. B. 1993, ApJ, 419, L45

Turner, M. S. 1999, in ASP Conf. Ser. 165: The Third Stromlo Symposium: The Galactic Halo, ed. B. Gibson, T. Axelrod, & M. Putman, 431

Vittorio, N. and Silk, J. 1984, ApJ, 285, L39

White, M. 2001, ApJ, 555, 88

White, M., Carlstrom, J. E., Dragovan, M., and Holzapfel, W. H. 1999a, ApJ, 514, 12

White, M., Carlstrom, J. E., Dragovan, M., Holzapfel, W. H., Halverson, N. W., Kovac, J., and Leitch, E. M. 1999b, Analyzing Data from DASI, astro-ph/9912422

White, M., Scott, D., and Silk, J. 1994, ARA&A, 32, 319

White, M. and Srednicki, M. 1995, ApJ, 443, 6

Wright, A. E., Griffith, M. R., Burke, B. F., and Ekers, R. D. 1994, ApJS, 91, 111

Wright, E. L. 1999, New Astronomy Review, 43, 257

Zaldarriaga, M. and Seljak, U. 2000, ApJS, 129, 431, astro-ph/9911219

Zeldovich, Y. B. 1972, MNRAS, 160, 1P

Zhang, X. 1993, IEEE Trans. Microwave Theory Tech., MT-41, 1263